

ABSTRACT

SOTORY, PETER ZSOLT. Carbon Pyrolyzed Photoresist Film and Platinum Microelectrode Chronoamperometry Using a Single and Double Potential Step Approach for Dopamine Detection and Electrode Interaction with Cottrell Equation Relations. (Under the direction of Dr. Gregory S. McCarty).

Dopamine is an important molecule as part of the synaptic language governing the neuronal communications through the trillions of axonal and dendritic interconnections between nerves found in the human brain and body. It has been linked to major functions such as movement, behavior, pain perception, learning, motivation, cognition, emotions and memory. The catecholamine is also implicated with the cardiovascular, metabolic, renal, hormonal and immune systems. As a hydrochloride salt, dopamine can additionally be administered as a pharmaceutical. With such an extensive set of roles, there is a need to have sensors capable of detecting dopamine concentrations.

The focus of this work was the chronoamperometric study of both microscale platinum and carbon pyrolyzed photoresist film sensors of similar design to electrochemically detect dopamine in solution. Previously the design had been used with Fast Scan Cyclic Voltammetry (FSCV) as a prospective method to record the extracellular volume transmission of dopamine in brains. In this current work, single and double potentiometric step approaches were utilized to characterize both sensor type oxidative response linearity and analyze the competitive shielding interaction between dual potential electrodes. The redox cycling capacity, mass transport flux, electrical current flux, and Cottrell equation relation of these sensors were additionally investigated.

Initially the sensors quickly fouled and had non-linear responses. A technique was developed to electronically clean the sensors to reliably restore their sensitivity. Following this discovery, the oxidative dopamine testing response became linear and dependable, enabling the chronoamperometric study of the devices.

The findings showed there was evidence for electrode competition or shielding and that redox cycling was more successful with the carbon PPF design than the platinum type of sensor. The mass transport and electrical current flux per unit area were dependent on the surface area of the electrodes. The measured oxidative current was not directly predictable by the Cottrell equation. For some of the platinum sensor testing cases the difference was

merely a constant multiplier. But for the remaining platinum testing scenarios, and in all of the carbon PPF cases, the multiplier was a function inversely proportional to the square root of the concentration. The same data trend could also be successfully matched to an exponential equation. Both function forms are of a type used to characterize the potential decay from an electrode surface into an ionic solution. The Debye-like modulation of the Cottrell equation suggests the observed current is an outcome of the electrode interacting with a zone or volume of solution on a length scale influenced by the size of the electric double layer from the electrode surface. Electron tunneling, moderated by the electric double layer Debye length scale, is a candidate for the method of action. There are several favorable influences for it explored in the discussion, including dopamine's chemical nature, sterically constrained water near the electrode surface, as well as other additional factors.

© Copyright 2014 Peter Zsolt Sotory

All Rights Reserved

Carbon Pyrolyzed Photoresist Film and Platinum Microelectrode Chronoamperometry using a
Single and Double Potential Step Approach for Dopamine Detection and Electrode
Interaction with Cottrell Equation Relations

by
Peter Zsolt Sotory

A thesis submitted to the joint Graduate Faculty of
North Carolina State University in Raleigh and the
University of North Carolina at Chapel Hill
in partial fulfillment of the
requirements for the Degree of
Master in Science

Biomedical Engineering

Raleigh, North Carolina

2014

APPROVED BY:

Dr. Glenn Walker

Dr. H. Troy Nagle

Dr. Gregory S. McCarty
Chair of Advisory Committee

DEDICATION

To my mother, father and family.

BIOGRAPHY

After undergraduate study, the author has worked in research and development in industry. He was later accepted as a graduate student at the joint university Biomedical Graduate Program of North Carolina State University in Raleigh and the University of North Carolina at Chapel Hill to pursue a Masters in Biomedical Engineering.

ACKNOWLEDGMENTS

I would like to thank my parents, family and friends for their encouragement and support in this endeavor.

I would also like to thank my advisor, Dr. Gregory McCarty, for his expertise, assistance, always making time for discussion and providing the opportunity to work in his lab, the Biomedical Engineering Cleanroom and the NCSU Nanotechnology Facility. Thank you also to Dr. Glenn Walker and Dr. H Troy Nagel for lab materials and lab access. Many thanks also go to Vindhya Kunduru, Adam Dengler, Lindsay Walton, Alison Amos, Bruce Sprague, Steve Callender, Miguel Acosta, Daniel Salo and Eugene Yamamura for their assistance and contributions in the lab. Also I would like to thank Vilma Berg for skillfully helping to navigate through the steps needed to complete the degree.

For this kind of academic journey it is really impossible to thank everyone who contributed to all the incremental parts and background leading to its success without making a list as long as a thesis itself. There are others who deserve thanks as well. Thank you to all.

TABLE OF CONTENTS

LIST OF TABLES	vii
LIST OF FIGURES	viii
Chapter 1 Introduction and Background.....	1
1.1 Research Objectives and Goals.....	1
1.2 Importance and Background of Dopamine	1
1.3 Sensor Technique Overview and Literature	3
1.4 Electrochemical Detection Background	11
1.5 Chronoamperometry Background.....	14
1.6 Dopamine as an Electroactive Species	19
1.7 Electrode Surface Chemistry and Physics Background.....	23
1.8 Microfabrication Background.....	27
1.9 Organization of this Thesis	34
Chapter 2 Sensor Fabrication and Testing Protocols.....	34
2.1 Platinum Microelectrode Sensor Fabrication.....	34
2.2 Carbon Pyrolyzed Photoresist Film (PPF) Microelectrode Sensor	38
2.3 Platinum and Carbon PPF Sensor Mounting for Testing.....	43
2.4 Circuit Design and Experimental Setup.....	44
2.5 Experimental Protocol	47
2.5a Reagents, Instrumentation and Software.....	47
2.5b Testing Protocol and Amperometry responses	49
2.5c Processing Data.....	55
Chapter 3 Results and Discussion for the Electrochemical Sensing of Dopamine.....	63
3.1 Platinum Sensor Electrode Oxidative and Reduction Results	63
3.2 Platinum Electrode Mass Transport.....	77
3.3 Platinum Sensor Electrode Current Flux	81
3.4 Platinum Sensor Electrode Cottrell Equation Relation.....	85
3.5 Carbon PPF Sensor Electrode Oxidative and Reduction Results	103
3.6 Carbon PPF Sensor Electrode Mass Transport.....	118
3.7 Carbon PPF Sensor Electrode Current Flux	123

3.8 Carbon PPF Sensor Electrode Cottrell Equation Relation.....	126
3.9 Comparison of Platinum versus Carbon PPF Sensors	136
3.9a Electrode Oxidative Response Comparison.....	136
3.9b Electrode Mass Transport	138
3.9c Electrode Current Flux	140
3.9d Carbon PPF and platinum sensor electrode Cottrell Equation relation	142
Chapter 4 Conclusions	144
Chapter 5 Future Work	147
REFERENCES	150

LIST OF TABLES

Table 1: Applied Waveforms and Potentials to Outer and Inner Electrodes	49
Table 2: Recorded Data Points for each Applied Waveform	60
Table 3: Platinum Scenario 1, Outer Electrode: Square Wave -0.4V to+0.7V, Inner Electrode: Square Wave -0.4V to +0.7V, 10 sec cycle	64
Table 4: Platinum Scenario 2, Outer Electrode: Square Wave -0.4V to+0.7V, 10 sec cycle, Inner Electrode: Constant +0.7V	67
Table 5: Platinum Scenario 3, Outer Electrode: Constant 0V, Inner Electrode: Square Wave -0.4V to +0.7V, 10 sec cycle.....	72
Table 6: Platinum Scenario 4, Outer Electrode: Square Wave -0.4V to +0.7V, 10 sec cycle, Inner Electrode: Constant 0V.....	74
Table 7: Cottrell Equation Multiplying Coefficient for Platinum Sensors	87
Table 8: Carbon Scenario 1, Outer Electrode: Square Wave -0.4V to+0.7V, 10 sec cycle, Inner Electrode: Constant -0.4V	104
Table 9: Carbon Scenario 2, Outer Electrode: Square Wave -0.4V to +0.7V, 10 sec cycle, Inner Electrode: Constant +0.7V	108
Table 10: Carbon PPF Scenario 3, Outer Electrode: Constant 0V, Inner Electrode: Square Wave -0.4V to +0.7V, 10 sec cycle	113
Table 11: Carbon Scenario 4, Outer Electrode: Square Wave -0.4V to +0.7V, 10 sec cycle, Inner Electrode: Constant 0V.....	115
Table 12: Comparing Platinum and Carbon PPF Sensor Oxidative Rates	137
Table 13: Comparing Platinum and Carbon PPF Sensor Mass Transport Flux Rates.....	139
Table 14: Comparing Platinum and Carbon PPF Sensor Nanoamp Flux Rates	141
Table 15: Characteristic Platinum and Carbon PPF Cottrell Equation.....	143

LIST OF FIGURES

Figure 1: An illustration of the principle components of a sensor.....	4
Figure 2: Examples of sensor components for Figure 1	5
Figure 3: Examples of a biocatalytic sensor.	6
Figure 4: An example of an affinity sensor.	7
Figure 5: Combining both nanowire and FET ideas, this is an example of a silicon wire field-effect transistor (SiNW-FET)	9
Figure 6: Volta and electrochemistry.	11
Figure 7: Examples of a three electrode electrochemical detection apparatus.	13
Figure 8: Frederick Gardner Cottrell, the namesake of the Cottrell Equation.....	14
Figure 9: Aspects of single step chronoamperometry.....	16
Figure 10: Varying step potential in chronoamperometry	17
Figure 11: Aspects of double step chronoamperometry	18
Figure 12: Dopamine's reversible electroactive nature.	20
Figure 13: The electrochemical dopamine detection operation of this paper's device design and how redox cycling in a collector-generator arrangement can aid the detection.	22
Figure 14: Electric double layer theories and illustrations.	25
Figure 15: Illustration of the PECVD process.	29
Figure 16: A cross section of etching processes showing removed substrate and a mask unaffected by the etchant	30
Figure 17: An overview of photolithography with additive and subtractive methods, resulting in carbon pyrolyzed film and metal deposition examples	33
Figure 18: The platinum sensor microfabrication process.....	36
Figure 19: Continuation of the platinum sensor microfabrication process.....	37
Figure 20: Platinum microelectrode sensor design.....	38
Figure 21: Carbon pyrolyzed photoresist film (PPF) sensor microfabrication process.....	41
Figure 22: Carbon PPF microelectrode sensor design.....	42
Figure 23: The mounted dopamine sensor, ready for testing on the probe station. Platinum and carbon PPF sensors looked nearly identical at this stage. The only difference was that for the carbon PPF sensors stainless steel wires were attached to the contact pads with conductive epoxy.	43
Figure 24: The dopamine sensor mounted on probe station for testing. Platinum and carbon PPF sensors looked nearly identical at this stage.....	44
Figure 25: The transimpedance amplifier circuit.....	45
Figure 26: More detail on the amplifier circuit.....	46
Figure 27: The completed construction of the amplifiers and their connectors.	47
Figure 28: A typical looking sensor response.....	50
Figure 29: The graph shows the loss of sensor performance with the number of trials performed due to fouling..	54
Figure 30: The process flow for data acquisition and processing programs.....	57

Figure 31: The graphs show the effect of smoothing the data and where the samples of current response values (black circles) were taken to be used for analysis.	59
Figure 32: Shifting in sensor response over time.....	62
Figure 33: Platinum sensors have a linear, oxidative concentration dependent curve for the outer electrode current in Scenario 1a where the outer electrode was at +0.7V and the inner electrode at -0.4V.	66
Figure 34: Platinum sensors have a linear, oxidative concentration dependent curve for the outer electrode current in Scenario 2a.	68
Figure 35: Platinum sensors have a linear, oxidative concentration dependent curve for the inner electrode current in Scenario 2b.	69
Figure 36: A reduction current was measured in Scenario 2c and it leveled off at approximately 20 μM	70
Figure 37: Scenario 2d for the platinum sensors produced a linear, oxidative concentration dependent curve for the inner electrode current.	71
Figure 38: Scenario 3b for the platinum sensors produced a linear, oxidative concentration dependent response curve for the inner electrode current.	73
Figure 39: Platinum sensors have a linear, oxidative concentration dependent response curve for the inner electrode current in testing Scenario 4a.	75
Figure 40: Platinum sensor oxidation rates per testing scenario in $\text{nA}/\mu\text{M}$	77
Figure 41: Mass Transport Flux for Platinum Sensors in Nanomoles per Second per Square Micrometer ($(\text{nM}/\text{t})/\mu\text{m}^2$) with linear regression lines.	79
Figure 42: Platinum sensor mass transport flux rates per scenario.....	81
Figure 43: Platinum Sensors Electrical Current Flux per Unit Area ($\text{nA}/\mu\text{m}^2$)/ μM with linear regression lines.....	83
Figure 44: Platinum Sensor Nanoamps Flux Rates per testing Scenario.....	85
Figure 45: The acid-base equilibria of dopamine leads to several forms for the molecule depending on pH.....	92
Figure 46: The Bockris-Devanathan-Muller (BDM) model.....	96
Figure 47: Platinum Scenario 3b) Coefficient Multiplier of Cottrell Equation for Inner I when $V_{\text{outer}} = 0.0\text{V}$, $V_{\text{inner}} = 0.7\text{V}$	100
Figure 48: Platinum Scenario 4a) Coefficient Multiplier of Cottrell Equation for Outer I when $V_{\text{outer}} = 0.7\text{V}$, $V_{\text{inner}} = 0.0\text{V}$	101
Figure 49: Plot of the measured platinum coefficient multipliers.	103
Figure 50: The carbon PPF sensors have a linear, oxidative concentration dependent curve for the outer electrode current in Scenario 1a where the outer electrode was at +0.7V and the inner electrode was at -0.4V.	105
Figure 51: The carbon PPF sensors have a linear, reduction concentration dependent curve for the inner electrode current in scenario 1b where the inner electrode is at -0.4V and the outer electrode is at +0.7V..	107
Figure 52: Carbon PPF sensors have a linear, oxidative concentration dependent curve for the outer electrode current in Scenario 2a.	109
Figure 53: Carbon PPF sensors have a linear, oxidative concentration dependent curve for the inner electrode current in Scenario 2b.	110

Figure 54: A reduction current was measured on the outer electrode in Scenario 2c for the carbon PPF sensors unlike the platinum sensors. 111

Figure 55: Scenario 2d for the carbon PPF sensors produce a linear, oxidative concentration dependent curve for the inner electrode current. 112

Figure 56: Scenario 3b for the carbon PPF sensors produced a linear, oxidative concentration dependent curve for the inner electrode current. 114

Figure 57: Carbon PPF sensors have a linear, oxidative concentration dependent curve for the inner electrode current in Scenario 4a. 116

Figure 58: Carbon PPF sensor oxidation rates per scenario in nA/ μM 117

Figure 59: Mass Transport Flux for carbon PPF Sensors in Nanomoles per Second per Square Micrometer ((nM/t)/ μm^2) with linear regression lines.. 120

Figure 60: Carbon PPF sensor mass transport flux rates per scenario..... 122

Figure 61: Carbon PPF electrical current per unit area (nA/ μm^2) with linear regression lines. 124

Figure 62: Carbon PPF Sensor Nanoamp Flux Rates per testing Scenario. 126

Figure 63: The carbon PPF sensor Scenario 1a coefficient multiplier of the Cottrell Equation for the outer electrode current when $V_{\text{outer}} = 0.7\text{V}$ and $V_{\text{inner}} = -0.4\text{V}$ 127

Figure 64: The carbon PPF sensor Scenario 2a coefficient multiplier of the Cottrell Equation for the outer electrode current when $V_{\text{outer}} = 0.7\text{V}$ and $V_{\text{inner}} = 0.7\text{V}$ 129

Figure 65: The carbon PPF sensor Scenario 2b coefficient multiplier of the Cottrell Equation for the inner electrode current when $V_{\text{outer}} = 0.7\text{V}$ and $V_{\text{inner}} = 0.7\text{V}$ 130

Figure 66: The carbon PPF sensor Scenario 2d coefficient multiplier of the Cottrell Equation for the inner electrode current when $V_{\text{outer}} = -0.4\text{V}$ and $V_{\text{inner}} = 0.7\text{V}$ 132

Figure 67: The carbon PPF sensor Scenario 3b coefficient multiplier of the Cottrell Equation for the inner electrode current when $V_{\text{outer}} = 0.7\text{V}$ and $V_{\text{inner}} = 0.0\text{V}$ 133

Figure 68: The carbon PPF sensor Scenario 4a coefficient multiplier of the Cottrell Equation for the outer electrode current when $V_{\text{outer}} = 0.7\text{V}$ and $V_{\text{inner}} = 0.0\text{V}$ 135

Figure 69: All measured carbon PPF sensor measured multiplier values together. 136

Figure 70: Possible future modification to the sensor could include a partial covering over the sensing region. 148

Chapter 1 Introduction and Background

1.1 Research Objectives and Goals

The focus of this work was the chronoamperometric study of both microscale platinum and carbon pyrolyzed photoresist film sensors of similar design to electrochemically detect dopamine in solution. Single and double potentiometric step approaches were utilized to characterize both sensor type oxidative response linearity and analyze the competitive shielding interaction between dual potential electrodes. The redox cycling capacity, mass transport flux, electrical current flux, and Cottrell equation relation of these sensors were also investigated.

In order to attain these objectives, it was necessary to include several additional goals in this project. This involved the successful microfabrication of the carbon pyrolyzed photoresist film and platinum sensors. Also the physical electronics hardware was constructed which was needed to set voltage potentials on the sensors, amplify and measure the nanoamp sized currents. In addition, the software for controlling the hardware, data acquisition, equilibrating the sensors, automating the testing protocols and data processing was programmed.

1.2 Importance and Background of Dopamine

Dopamine is studied because it has significant functions in both the brain and body. It is a catecholamine perhaps best known for its role as a neurotransmitter in the central nervous system, used for communication between nerve cells [91]. The brain is where most of this dopamine messaging takes place. As the most complex organ known, the brain has tens of billions of nerve cells, each with its own thousands of axonal and dendritic connections to other neurons, making for hundreds of trillions of interconnections where dopamine is part of the inter-nerve cell synaptic language [35][94]-[97][127]. With such a ubiquitous presence, it is not surprising that dopamine has been linked to many important functions and systems including movement, pain perception, behavior, learning, reward,

motivation, cognition, emotions and memory [81][82][88][90][128]. The neuronal communication network activity behind these roles can be characterized as taking place with fast moving, fleeting “phasic” components and slower, ebbing “tonic” elements [78]. These two terms refer both to the rate of nerve firing and resulting waves of dopamine concentration that wash through the extracellular fluid of brain tissue as a result of the nerve firing [78]. Together the dopamine communication and dopamine volume transmission are of interest to brain researchers [5][6][35][77][78][92].

Dopamine also has important roles in other crucial body systems such as human metabolism, cardiovascular, renal and hormonal systems [83][85]. Low levels of dopamine can cause illnesses such as schizophrenia, Huntington’s disease, and Parkinson’s disease [83]-[85]. High levels of dopamine can cause negative health issues as well, such as vomiting, nausea and cardiac arrhythmias [84].

Dopamine, as a hydrochloride salt, can also be used as an injectable drug for treating symptoms of shock including bronchial asthma, hypertension, heart failure, endotoxic septicemia and renal failure [81][84][86]. In addition, the pharmaceutical version of dopamine has found use in the parallel problems of circulatory collapse originating from myocardial infarction, trauma, kidney failure, cardiac surgery or congestive cardiac failure [87].

Dopamine also plays a role in the immune system. It is synthesized by lymphocytes and these immune cells are also influenced by dopamine as they have dopamine receptors on their cell membranes [88]-[90]. Due to those receptors, T cells, dendritic cells, B Cells, Natural Killer (NK) cells, neutrophils, eosinophils and monocytes have been shown to be regulated by dopamine [88][93]. Furthermore, the existence of these receptors indicates that dopamine has a role in the control and regulation of the immune response [93]. When this regulation system is decoupled or disrupted, cancer or autoimmune problems may develop [93].

For these reasons and others, dopamine and its roles are being actively studied in laboratories around the globe as evidenced by the many published papers related to the

catecholamine. The diverse areas of dopamine function and investigation explain why there is a compelling need to create sensors and systems capable of detecting dopamine in vitro, in vivo or for pharmaceutical implementation.

1.3 Sensor Technique Overview and Literature

The ever expanding universe of sensors has enabled the study and further understanding of chemical and biological processes for medical, research and biotechnological pursuits and applications. Individual cells, tissues, bacteria, bodily fluids, the environment as well as other kinds of samples can be examined with sensors tailored made to evaluate specific properties of interest [1]-[4].

Despite the diverse categories of samples and seemingly infinite number of properties that can be chosen to be measured, there is a fundamental underlying theme common to any kind of sensor. All sensors recognize a biological, chemical or physical change and generate a quantifiable and processable signal proportional to that change [1]-[3][15].

Sensor devices can be thought of as having three components. First is the recognition part, made of a selective receptor. This portion will identify a specific analyte or family of analytes with a design that diminishes the chance of interference from other compounds present in the sample [1][2]. The creation of a signal from the interaction with the analyte is considered the transducer characteristic of the sensor [1]-[3]. The transducer signal is converted to an electronic signal and sent to signal processor and displayed [1][2]. Figure 1 illustrates these principle components of a sensor.

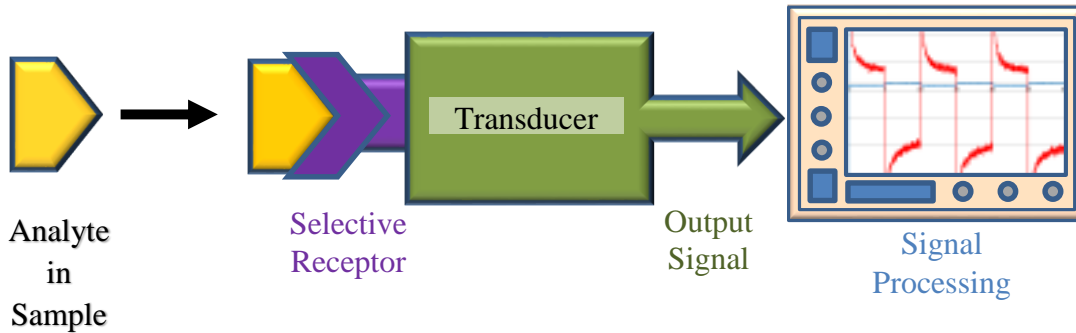


Figure 1: An illustration of the principle components of a sensor [1]-[3][36].

The general concepts in Figure 1 can be implemented in a myriad of ways for the design and construction of sensors. To show how these ideas apply, Figure 2 supplies some examples for Figure 1 components. As discussed earlier, the origin of the samples can vary, as would the analytes of interest. The selective receptor element examples in Figure 2 are shown as nucleic acids, cells, antibodies and enzymes. The electrical interface element examples are illustrated as (field effect transistors) FET devices, nanowire arrays, nanoparticles, or electrodes. Together the receptors and the electrical interfaces function as the transducer. The transducer signal is amplified by an electronic circuit, processed and collected by computer software to be presented in a meaningful representation to the experimenter [1][2].

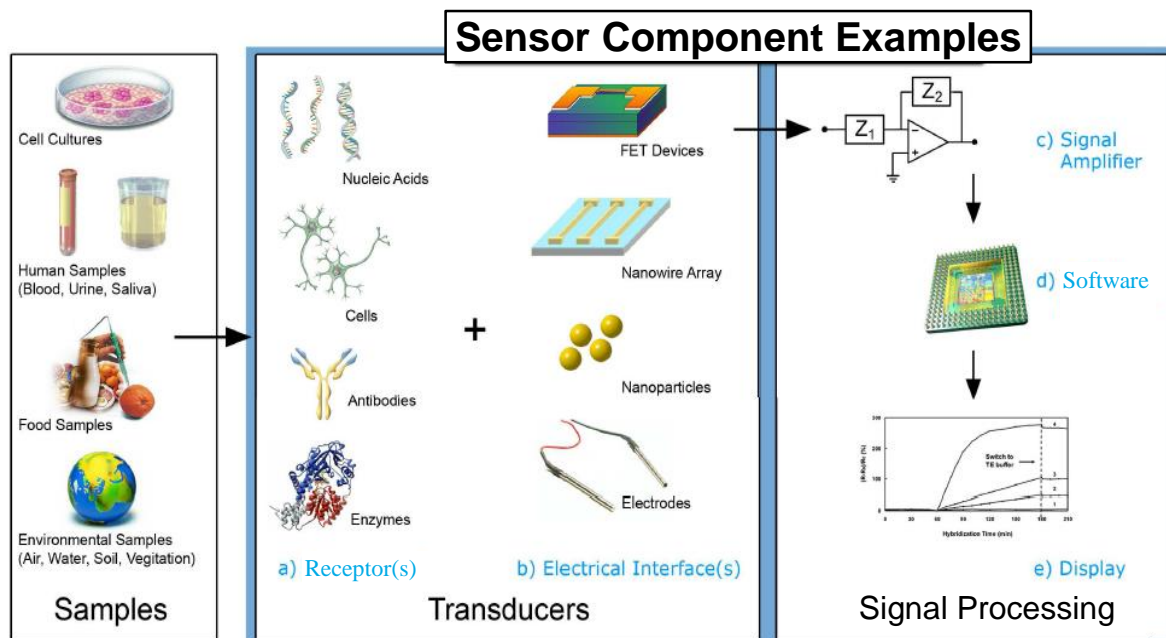


Figure 2: Examples of sensor components for Figure 1 [1][2][16][17]. Figure is derived from [2].

As indicated by Figure 2, the transducer mechanisms for detection can be used to classify the sensors into different categories. Some of the sensor categories represented include biocatalytic activity, affinity, field effect transistor nanowires and electrode electrochemical sensors categories. These will be briefly discussed to show the variety that is possible in the operating principles for these devices.

Biocatalytic sensors use tissues, entire cells, or enzymes to target a specific analyte [1]. These recognition elements can interact with the analyte to produce a detectable product, such as an electroactive species [1][7]. The most compact designs use enzymes for their selectiveness and ability to enhance reaction rates considerably [1]. The best known biocatalytic sensors are personal blood glucose measuring devices [1].

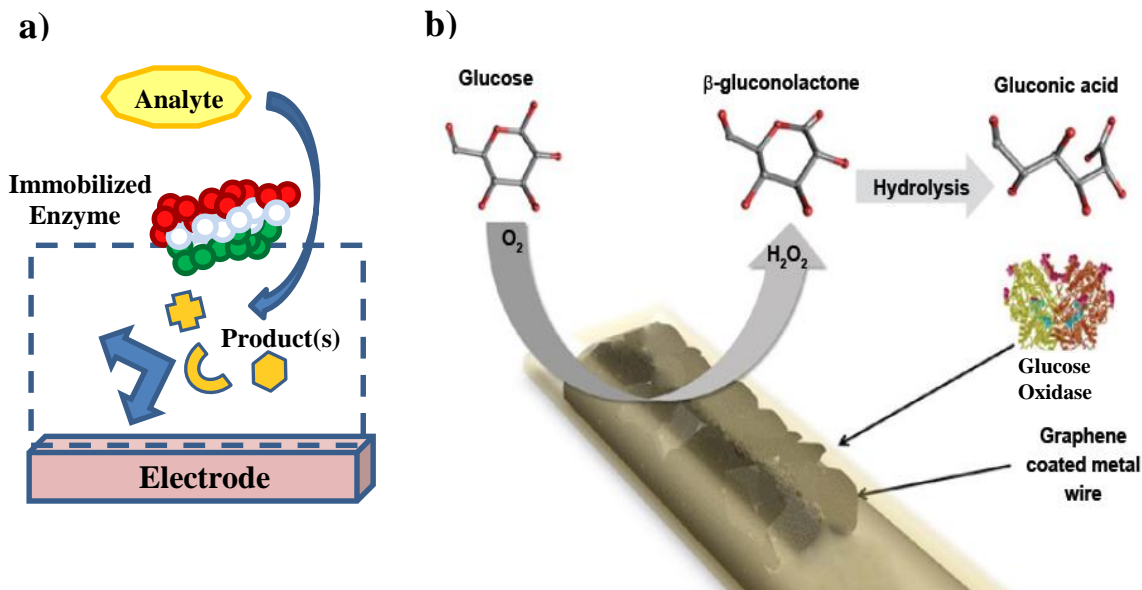


Figure 3: Examples of a biocatalytic sensor. a) A model biocatalytic sensor, where a bound, immobilized enzyme catalyzes a reaction and creates products where at least one can be detected with an electrode due to the molecule's electroactive nature [1][2][37]. Some ways of immobilizing enzymes include polymer/gel entrapment, covalent binding, electrostatic attraction and surface adsorption [1]. b) A covalently and electrostatically immobilized glucose oxidase is used on a graphene sensor to detect glucose [37]. Glucose enzymatically reacts with glucose oxidase, to make β -gluconolactone and hydrogen peroxide (H_2O_2). The β -gluconolactone undergoes immediate hydrolysis, creating gluconic acid and lowering the pH, which is detectable amperometrically. Most other glucose sensors detect the produced H_2O_2 from glucose oxidase. Figure 3b is derived from [37].

Affinity sensors use the specificity and robust binding properties between certain receptor element molecular species with their ligand analyte species [1][15]. The receptor elements include such molecules as antibodies, cell receptors, peptide aptamers, nucleic acid aptamers, and phages [1][15][16]. The resulting linkage can be detected via an electrical response [1][15][16].

Figure 4 shows an aptamer based affinity sensor. An aptamer is an artificial nucleotide sequence. The benefit of using an aptamer is that they can be designed to be

smaller than the Debye length [48]. This feature allows them to be very specific because the protein-aptamer reactions take place within the electric double layer where the charge screening influence of the bulk solution is reduced [43][48].

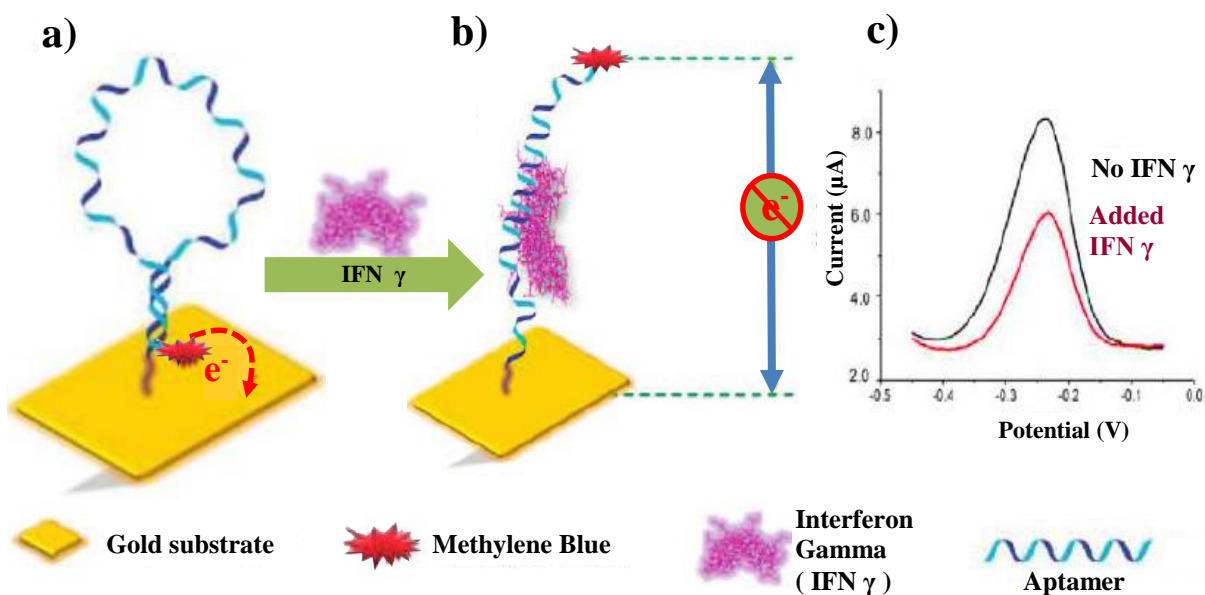


Figure 4: An example of an affinity sensor. Here the sensor can detect the cytokine Interferon Gamma (IFN γ). a) The receptor element of the sensor is a nucleic acid hairpin aptamer. The hairpin aptamer is attached in a self-assembly process, with a thiolated 5' end, to a gold substrate/electrode. In the absence of the target IFN γ , the aptamer loop holds a redox label, methylene blue, close to the gold substrate [16][17]. b) When the target IFN γ is present, the hairpin undergoes a conformational change. The distance of the redox label from the gold substrate is then increased, decreasing the electron-transfer efficiency of the gold electrode [16][17]. c) The before and after faradaic current shows a decreased current with the presence IFN γ when using square wave voltammetry [16][17]. Adapted with permission from [17]. Copyright (2010) American Chemical Society.

The nanowire reference in Figure 2 refers to a category of sensors that includes nanotubes, nanorods, nanobelts, thin films as well as others nanostructures [2][9]. The feature that unites them as a family is a large length to diameter aspect ratio of the structure [9]. The lengths are generally magnitudes larger than the diameters of the wire which are

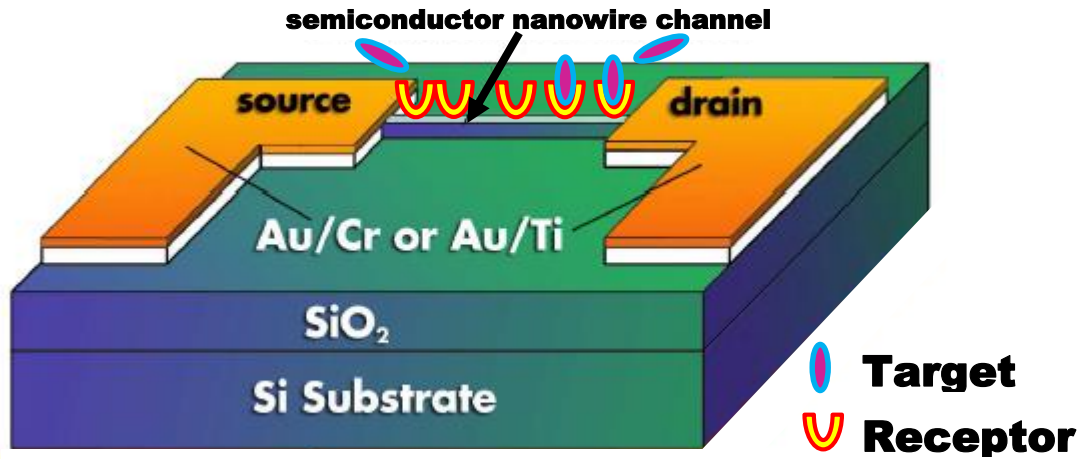
usually in the nanometer range [2][9]. Since the nanowires have a large surface area to volume ratio, their conductance is sensitive to slight variations in charges on the nanowire surface [2][18].

Nanowires can be grown in a well understood and controlled fashion with an assortment of chemical compositions [9]. This has allowed nanowires to be incorporated into field-effect transistors (FET) to detect protein, pH, cancer and viral markers, single viruses, DNA at the femto molar range, RNA, metal ions and a wide range of other biological species [2][10][11][18]. Also the union of nanowires and FETs illustrate that sensor elements, such as those in Figure 2, can sometimes be combined to create new devices. In this case, that is the silicon wire nanowire FET (SiNW-FET) as shown in Figure 5.

The SiNW-FET is made of drain, source, and semiconductor channel usually on a silicon substrate with an insulating/dielectric layer such as silicon dioxide [2][18]. The semiconductor channel is functionalized with immobilized receptors made of DNA, RNA, proteins or antibodies to target charged molecules [18]. The proximity of the charges to the narrow pathway allowed for the electron flow alter the nanowire's conductivity, modifying the electrical current between the drain and source in a detectable manner [2][13][14].

Interestingly, there are a number of reversible surface modification approaches that have been developed for SiNW-FETs [18]. These techniques enable a replacement of the target-receptor complex with a fresh layer of receptors while also maintaining the same number of receptors on the surface for the tested device [18]. This is a useful feature during the repeated cycles of testing and calibrating the devices for analysis [18]. The reusable surface is made possible by methods adopted from protein purification procedures that anchor a base molecule to a substrate which can be made to attach or release an attached compound. In this case, the attachment is of the unbounded receptor and release would be for the target-receptor complex [18]. The system relies on a glutathione (GSH)/glutathione S-transferase (GST)-tag and Ni²⁺/hexahistidine (His₆)-tag systems and a cleavable disulfide bond (S–S) [18].

a) **Functionalized Silicon Nanowire FET**



b)

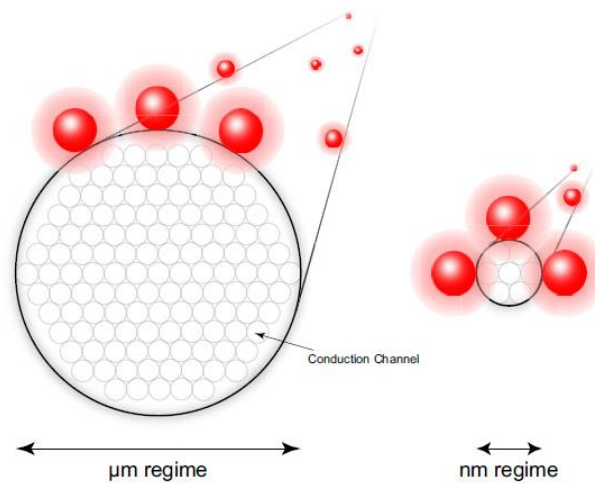


Figure 5: Combining both nanowire and FET ideas, this is an example of a silicon wire field-effect transistor (SiNW-FET) [2][12][18]. a) The nanowire channel is specifically coated (functionalized) with receptor molecules that bind to charged target molecules, securing the charged molecules close to the surface of the nanowire [2][13][14]. The proximity of the charges to the narrow pathway allowed for the electron flow alter the nanowire's conductivity, modifying the electrical current in a detectable manner [2][13][14]. b) An illustration of how charged molecules become increasingly influential on conductors of nanowire dimensions [2]. Figure is derived from [2].

One final aspect of Figure 2 to be quickly reviewed is the use of electrodes for sensing, more routinely referred to as electrochemical detection. For this technique, electric potentials and currents are applied to the electrode from a selection of patterns to detect the presence of an analyte. These methods are generally described as either voltammetry or amperometry. Microscale and nanoscale electrochemical electrodes have good measuring abilities on a short time scale, can be used for molecular flux analysis of cells and skin, and if spaced nanometers apart, can detect a single molecule [5][6]. The functional advantages of electrochemical detection with electrodes is portability and an affordable cost [1]. The work of this thesis focuses on electrochemical detection and will be discussed in greater detail in the upcoming section.

There are a great many other sensor technologies beyond what is described here. Just a short listing would include those based on carbon nanotubes, surface plasmon resonance (SPR), branched intracellular nanotube FET (BIT-FET), conductometry, electrochemical impedance spectroscopy (EIS), electrochemical quartz crystal microbalance with dissipation monitoring (EC-QCM-D), photometry, thermometry, scanning electrochemical microscopy (SECM) and graphene [1]-[3][18][19][24].

Regardless of the technology involved, effective sensor design will address the following criteria [2][3]:

- Maximize selectivity and avoid “crosstalk” from other analytes.
- Have an appropriate sensitivity range and resolution for measurements.
- Have an implementation that is unaffected by physical conditions such as pH, stirring, and temperature. If these conditions cannot be avoided, then the implementation design must compensate for the conditions.
- Have a precise, duplicatable and predictable linear response over the expected operating conditions.
- Have minimized internal system noise from the electronics or transducer.
- Have an acceptable response and recovery time.

- The dimensions of any implantable sensor should be as minimally invasive as possible without toxic effects nor provoking an immune response.
- Have a reliable construction, ensuring an acceptable working lifetime.

1.4 Electrochemical Detection Background

The concentration of work in this thesis is the electrochemical detection of dopamine. Electrochemical detection has its foundation in electrochemistry. Electrochemistry relates the connection between chemical and electrical change [21]. The study of electrochemistry spans back over two centuries. It was heavily influenced by the experiments and theories set forth by Alessandro Volta, Sir Humphrey Davy and Michael Faraday [21]. Their work established the basis for electrolysis and chemical reactions that produce electrical current, the pillars of modern electrochemical detection [21].



Figure 6: Volta and electrochemistry. Volta observed the electricity produced between dissimilar metals in moist settings, leading him to grade metal and other substances based on the intensity of their effect [23]. This classification became the “electrochemical series”, well known to students and scientists of today [23][25]. Volta also explained electrochemical chemistry to Napoleon and his court. Napoleon was so captivated by the scientific discoveries, he insisted to be an assistant for the next talk Volta gave on the subject [21]. The picture is courtesy of Library and Artifacts of the Bakken Museum [32]. The museum was established by Earl Bakken who co-founded Medtronic, the 4th largest biomedical device company in the world.

Up till the middle of the 20th century, the body of electrochemical work focused on expanding the knowledge of reactions and how current or voltage affected electrode reactions [22]. By the 1950s and 60s there was an accelerated growth to the field with the advent of the operational amplifier and other solid-state technology proliferating the types of experiments that could be done with carefully modulated potentials and currents [21][22]. With the start of the 1970s, electroactive species were beginning to be studied in animals [35]. Over time, electrodes became smaller and reduced in size for finer testing. By the 1980s, they could be useful for neuronal measurements [22]. There were still issues with fabrication at micrometer scale, but the continued work since then has overcome the obstacles [5]. Now in the 21st century, the methods to construct the electrodes for different microscopic geometries are well developed [5]. The options possible for microfabrication have become encyclopedic in volume, with the pantheon of processes including several forms of lithography (e.g. e-beam, UV), material removal techniques (e.g. patterning, lift-off, etching), and additive technologies (e.g. chemical and physical vapor deposition, thermal oxidation) ultimately allowing for the construction of microelectrodes within MEMs, BIO-MEMs and BIO-NEMs [26]-[28]. In fact, it is rare today to find published articles that do not utilize microelectrodes in electrochemical detection [22]. Their small size minimizes the disturbance to the microdomains being measured, the chemistry probing can be done in contact with tissues or cells, and they are useful in monitoring molecular fluxes across tissues, cells or skin [5]. In terms of operating parameters they are beneficial as well because their dimensions have high levels of steady-state mass transport, lessened ohmic drop distortion in contrast to large electrodes, and reduced double layer charging noise compared to macro dimensions as well [24].

A typical electrochemical system is comprised of three electrodes. These are a working electrode, a counter electrode and a reference electrode, to which all potentials are referenced [2]. Examples of a three electrode detection system can be seen in Figure 7.

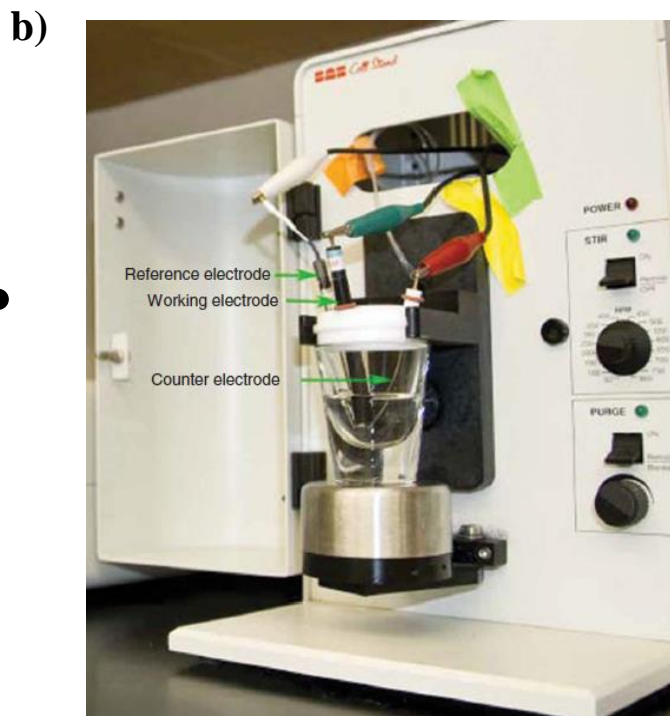
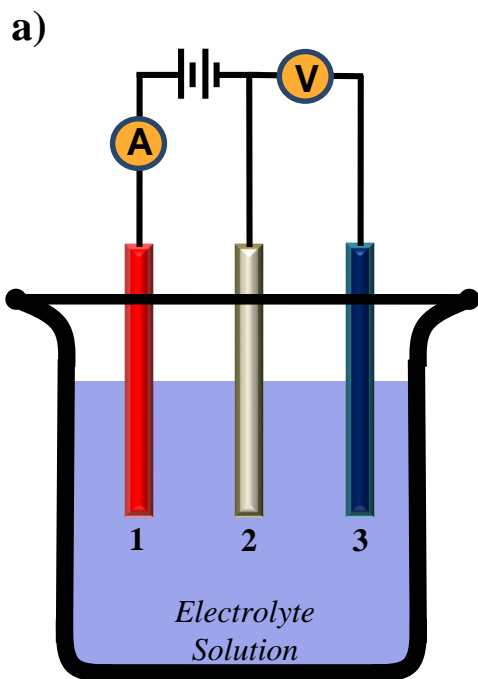


Figure 7: Examples of a three electrode electrochemical detection apparatus. a) Schematic showing the working, counter and reference electrodes, demonstrating how potential is set relative to the reference electrode and how the electrical current flow of the system can be monitored [2][29]. For the work represented in this paper, current was measured on both the working and counter electrode, and the scale of both these electrode was on the micron level. b) A commercial version of three electrode electrochemical cell used to test and characterize sensors [30]. For the work represented in this paper, the necessary electronic apparatus was locally constructed and the software was custom programmed for this experiment. Figure 7b is reprinted by permission from Macmillan Publishers Ltd: [Nature Protocols] Ref. [30], copyright (2007).

When a potential is applied to a working electrode, there is a current that results from the oxidation or reduction of the analyte in solution along the surface of the electrode [1]. When the potential is varied over a range, the technique is referred to as cyclic voltammetry.



Figure 8: Frederick Gardner Cottrell, the namesake of the Cottrell Equation. Cottrell created a number of inventions, including the electrostatic precipitator to scrub factory exhaust of pollutants. He used his patents to make a research foundation to help fund research in many scientific fields (Robert Goddard's rocketry and Ernest Lawrence's particle accelerator, the cyclotron, are just 2 instances). The institution founded in 1912 still exists today. Image courtesy of the Research Corporation for Scientific Advancement (RCSA) [38]-[40].

Since potential can be applied in different ways, there are many of forms of cyclic voltammetry. The patterns include square wave voltammetry, linear sweep, stripping voltammetry, differential staircase, differential pulse, ac voltammetry, polarography analysis as well as others [2][3]. When the potential is maintained on the working electrode and the current is monitored over time, it is referred to as amperometry or chronoamperometry [1]-[3].

The current measured in chronoamperometry is limited to the diffusion rate of the analyte, also referred to as a diffusion limited current [2][3]. In other words, the current flux is proportional to how quickly the analyte diffuses toward and away from the electrodes. The Cottrell equation, (6), brings together the variables of diffusion rate, time, Faraday's constant, the electrode area, the analyte concentration, the number of transferred electrons per analyte molecule and predicts the expected electrical current values, making it an important tool for chronoamperometry [2].

1.5 Chronoamperometry Background

The chronoamperometry approach is used to detect electroactive species like dopamine by applying a square wave potential and monitoring the current response over time. The voltage values of the square wave are selected where at least one of the potentials corresponds to analyte oxidation or reduction. The experimental arrangement keeps the set

electrode voltage by providing enough current to maintain that chosen potential [20]. From the physical standpoint, it is the diffusion of the analyte to the electrodes that determines the current via the electrochemical reaction at the electrode surface [20][24]. For oxidation, electrons are being transferred from the analyte to the electrode, while for reduction, electrons are being transferred from the electrode to the analyte. In either case, the flow of electrons can be measured analytically as electrical current. In these situations, the current can be referred to as diffusion limited or more generally as mass transfer limited current [20][24].

The effects of diffusion become apparent when the concentration of analyte and product are directly examined. For example, when the potential is stepped to the oxidation or reduction voltage of an electroactive species, all of the analyte near the electrode will be converted to the oxidized or reduced species respectively [20][24]. This happens instantaneously, drawing a high current at the same moment and making a concentration of product close to the electrode [20]. In the case of an electrode at oxidation potential, the supply of proximal analyte will be quickly oxidized. Only newly incoming analyte, arriving via diffusion and subsequently oxidizing at the electrode, will drive the flow of electrons to be measured as electrical current at the electrodes [20][24]. The oxidation current starts off large, but then will then decay rapidly. Given adequate time, the system settles into an equilibrium, with a steady-state current proportional to the electroactive species concentration in solution [3][20][24].

During these events, the concentration profile of product created adjacent to the electrode begins to expand [3][20][24]. At first the oxidized product is only found near the electrode. As time proceeds, more product is produced and diffused away into the medium, expanding the concentration profile of the oxidized product.

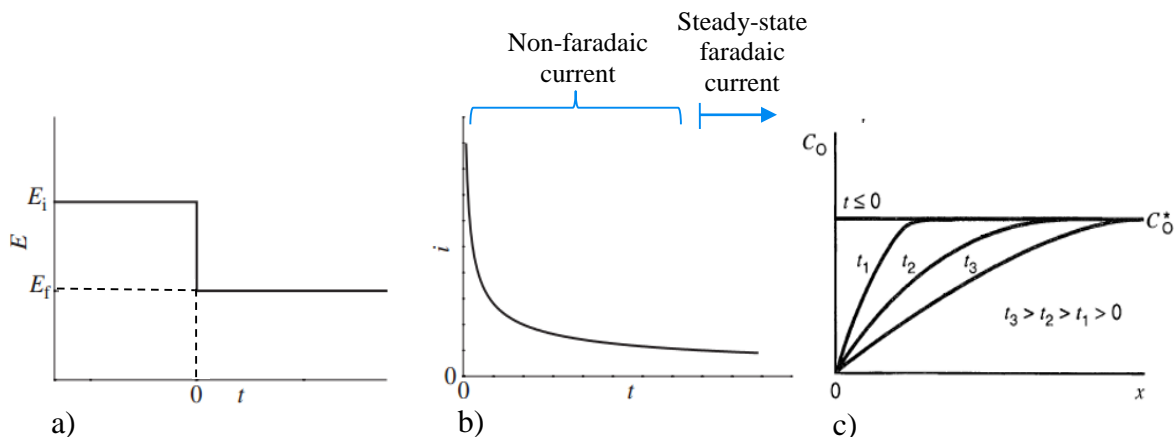


Figure 9: Aspects of single step chronoamperometry [20][24]. a) A step function input signal for an electroactive species that is unresponsive at the potential E_i , but at E_f becomes electrochemically reduced at a diffusion-limited rate [24]. b) A characteristic chronoamperometric response for the input step function [20][24]. The current will be high at first, but will begin to drop immediately. The transient current response is referred to as a non-faradaic current. When the response reaches steady state, it is a faradaic current. Both non-faradaic and steady-state faradaic current labels have been added to the figure. c) The concentration profile of the electrochemically reduced species product adjacent the electrode [20]. This example shows an electrochemically reduction. If it had been an oxidation event, a) and b) would have been very similar, and c) unchanged. For the same experimental configuration with an oxidation event, a) would have had the step function stepping positive, and the current response of would be a mirror image of the above b) below the horizontal axis. Conceptually the oxidative current response should have the opposite polarity of the reduction current response. The same relation should be true for the step function. Figure 9a and Figure 9b are derived from [24], reprinted from “Handbook of Electrochemistry”, by C. Zoski, pg 432, Copyright © 2007, with permission from Elsevier. Figure 9c derived from [20] in Bard & Faulkner, “Electrochemical Methods. Fundamentals and applications”, 2nd Edition. Copyright © 2000 by John Wiley & Sons, Inc. Reprinted by permission of John Wiley & Sons, Inc.

As mentioned in Figure 9(a), there are applied potentials where an electroactive species is inactive. These conditions will not generate any electroactive related currents from the analyte [20].

There are also a range of potentials where an electroactive species is responsive, but may not produce a smaller current than what is possible. By increasing the potential to an optimal level, a higher current can be produced that oxidizes or reduces the analyte at the rate equal to the rate that diffusion brings it to the surface of the electrode [20]. The difference between using an inactive potential, a non-ideal potential and an optimal potential can be seen in Figure 10.

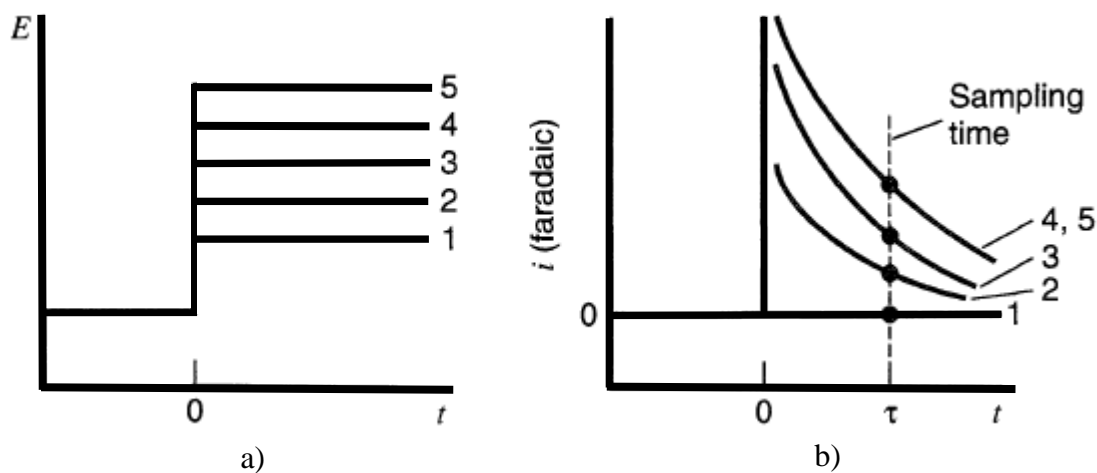


Figure 10: Varying step potential in chronoamperometry [20]. a) Examples of step waveforms that can be applied. b) Current measurements for each step potential, compared at the same time, τ . Step 1 is considered an inactive potential for the electroactive species and does not generate a current response in b). Step 2 and 3 are potentials where the electroactive species is being affected, and is either being oxidized or reduced, but not fully and are still not optimal potentials. Step 4 and 5 are potentials where the electroactive species is being oxidized or reduced. Increasing the potential beyond the value for Step 4 to Step 5 does not increase the current because the current is limited by the rate of speed the analyte can reach the electrode via diffusion. At the Step 4 potential, the optimal electrochemical conversion of analyte had been reached. In this case the concentration of analyte along the electrode is zero due to immediate electrochemical conversion into product. In Steps 2 and 3 the concentration of the analyte adjacent to the electrode was non-zero [20]. Figure derived from [20], from Bard & Faulkner, “Electrochemical Methods. Fundamentals and applications”, 2nd Edition. Copyright © 2000 by John Wiley & Sons, Inc. Reprinted by permission of John Wiley & Sons, Inc.

Up till now only single step chronoamperometry has been mentioned. However, in chronoamperometry, a square wave can be designed to have one potential of the waveform at the oxidizing potential of the electroactive species and the other at the reducing potential. When the potentials cycle are made to cycle this way, it is called double step chronoamperometry [20][24]. The resulting current response is similar in shape to the single step chronoamperometric response, but has both a positive and negative polarity waveform components as shown in Figure 11.

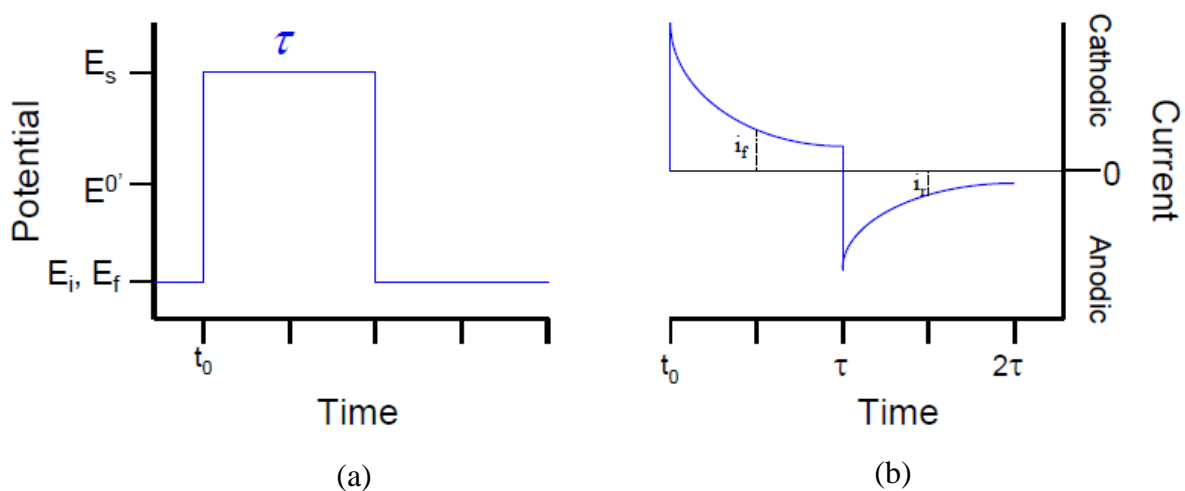


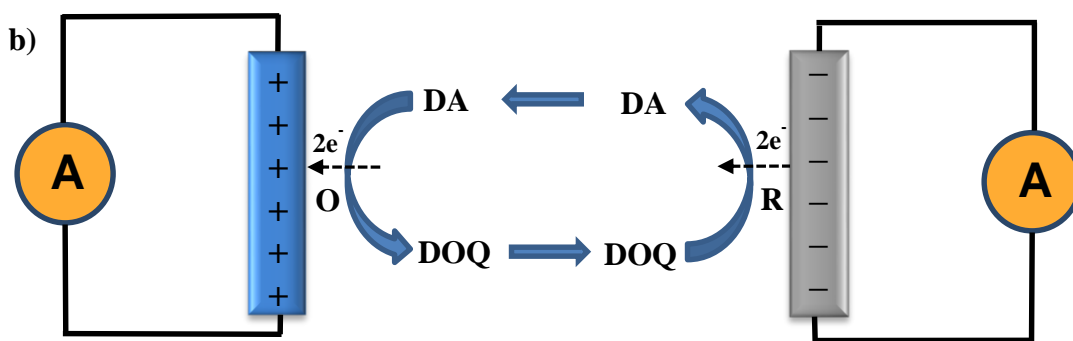
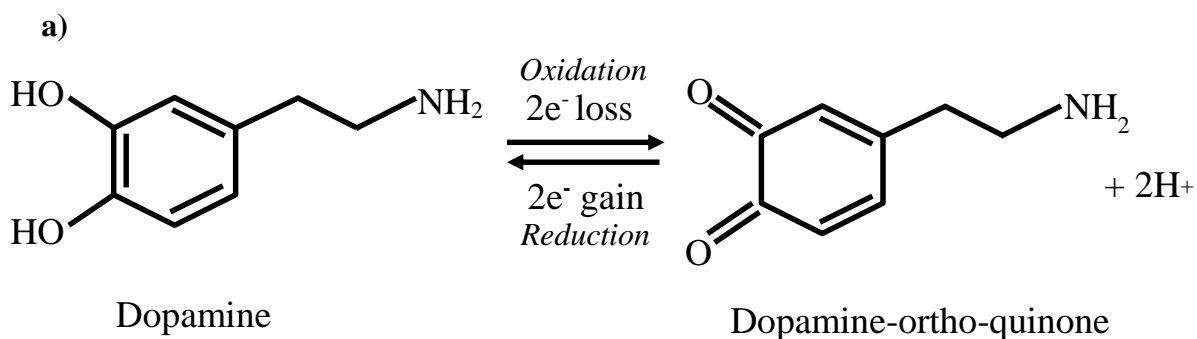
Figure 11: Aspects of double step chronoamperometry [33]. a) Step function with potentials levels set at oxidizing and reduction potentials for the electroactive species. b) Current response for the oxidative and reductive step functions. Figure derived from [33].

Lastly, the chronoamperometric technique for this study was applicable because the carbon pyrolyzed photoresist and platinum microelectrodes both operate in the so-called “small A/V conditions” [20]. They have small electrode area, A, compared to a large volume of solution, V, creating the situation where the device’s operation produces inconsequential

amounts of oxidized or reduced product species and does not alter the bulk concentration of the solution [20].

1.6 Dopamine as an Electroactive Species

Dopamine is an electroactive species that can be oxidized with an electrode at a +0.7V potential, converting it to dopamine-ortho-quinone (dopamine-o-quinone). An electrode at a -0.4V potential can reduce the dopamine-o-quinone back to dopamine. Either surface reaction on an electrode can be registered as a measureable electrical current. Figure 12 shows the reversible nature of these events.



DA = Dopamine
DOQ = Dopamine-ortho-quinone
O = Oxidation Reaction (converts DA to DOQ)
R = Reduction Reaction (converts DOQ to DA)

Figure 12: Dopamine's reversible electroactive nature. a) The chemical structure of dopamine is shown in equation illustrating how it changes in oxidation to dopamine-ortho-quinone. The dopamine-ortho-quinone can be made to undergo a reduction and return to dopamine. b) An illustration showing how electrodes at positive and negative potential can manipulate the reaction seen in a). When the electrode is held at a positive potential, dopamine is oxidized to dopamine-ortho-quinone [34]. When a molecule of dopamine is oxidized, it loses 2 electrons to the electrode which is measurable as a current. The reaction is reversed when the potential is changed to a negative potential. The dopamine-ortho-quinone is then reduced and converted back to dopamine. Here the electrode gives two electrons to the dopamine-ortho-quinone molecule to make dopamine. This reducing reaction is also measurable as a current, but will be in the opposite direction as the current detected in the oxidizing reaction. The experiment of this paper used +0.7V for the oxidizing potential and -0.4V for the reducing potential.

By spatially arranging electrodes close together in a parallel manner, it is possible to have the product species of one electrode diffuse to the second electrode, be electrochemically converted back to the original analyte species, return to the first electrode via diffusion, and have the process repeat. In this way the events are electrically detected on both electrodes. Since one electrode is generating the product and the other is collecting it, the arrangement has been referred to as a sensor operating in “generator-collector mode” [20]. The situation is also known as redox cycling, because the molecules are actively cycling through reduction and oxidation [1][41][42][47]. With either nomenclature, the concept is based on increasing signal strength and sensor sensitivity with the positive feedback arising from the flux of electrode produced species adding to the incoming flux from the bulk solution [20][41][42]. The more flux, the greater the measurable current. Additional gains can come from decreasing the gap between electrodes allowing for more redox cycles to occur, and again, with that creating more flux. [41][42].

Signal strength improvement also occurs when the number of electrodes are increased and closely interlaced into a design pattern that is called an interdigitated array [20][41][42]. The work of this paper is a small interdigitated sensor with three bands. A schematic of it and its conceptual redox cycling ability and overall functioning is shown below in Figure 13.

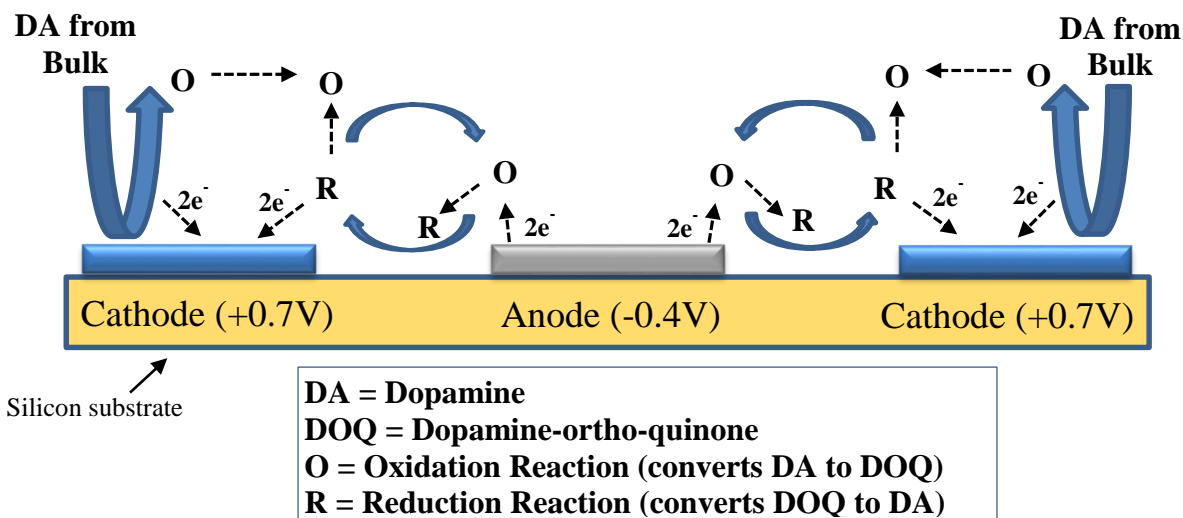


Figure 13: The electrochemical dopamine detection operation of this paper's device design and how redox cycling in a collector-generator arrangement can aid the detection. One of the several modes of operation for the device is shown here. See Section 2 & 3 for the other modes of operation. The other modes change the polarity of the electrodes. In the illustrated situation above, dopamine from the bulk solution is oxidized on the positive potential outer electrodes into dopamine-ortho-quinone, with the oxidation causing a measurable electrical current. The dopamine-ortho-quinone diffuses into the bulk solution, with some of it reaching the negative potential inner electrode. Here it is electrochemically reduced, becoming dopamine again, with the reduction reaction being detected as an electrical current. The newly produced dopamine also diffuses into the bulk solution and some of it moves to the outer electrode, where it reacts with the electrode and adding to the baseline measured current produced from the electrode interacting with the dopamine concentration of the bulk solution.

Redox cycling also offers the advantage that it improves sensor selection abilities when signal interfering molecules are present. An example of an interfering molecule with dopamine is ascorbic acid, more commonly known as Vitamin C. Ascorbic acid exhibits a similar oxidation potential as dopamine and as a result interferes with dopamine detection [78][80]. The problem becomes even more significant in tissue measurements, where concentration levels of ascorbic acid can exceed the concentration of dopamine by a factor of a thousand [78][83][87]. A developed method shown to prevent this interference is to use an anionic (negatively) charged polymer film such as Nafion that repels the negatively charged

ascorbic acid molecules, but allows dopamine passage through the film [80]. However, this introduces its own difficulties because within the polymer layer the diffusion rate of dopamine molecules are slowed [80]. With the dopamine molecular diffusion progress slowed across the film, the sensor's rate of detection in turn is also slowed [80].

Fortunately by using a redox cycling arrangement, the slowed response time and the interfering effects of ascorbic acid can both be avoided [80]. Dopamine can experience reversible oxidation like other catechols, but ascorbic acid does not share in this range of electroactive capability [80]. Instead when ascorbic acid is electroactively oxidized, the subsequent chemical product undergoes a quick, irreversible hydration reaction [80]. The resulting molecule cannot be reduced and it no longer interferes with the system [80].

This makes the redox cycling approach a useful alternative to electrode surface modification such polymer coatings, self-assembled monolayers, or enzymatic pretreatment [80].

1.7 Electrode Surface Chemistry and Physics Background

In ionic solutions, the charge of the ions screen the electrode potential with their own electric fields, negating the electrode's field at a distance known as the Debye length. The masking effect of the Debye length for electrolytes is measured on the order of nanometers and is inversely proportional to the ionic strength (concentration) of the solution. For instance, in a PBS (phosphate buffered saline) solution with 10nM of the negatively charged protein streptavidin, the Debye length is approximately 0.7 nanometers [43]. Decreasing the ionic strength of the solution by reducing its PBS concentration by ten times solution increases the Debye length to ~2.3 nm [43]. With another tenfold reduction of PBS concentration, the Debye length grows again and is approximately 7.3 nm [43]. The growth of the Debye length continues as the ion concentration for shielding becomes sparser.

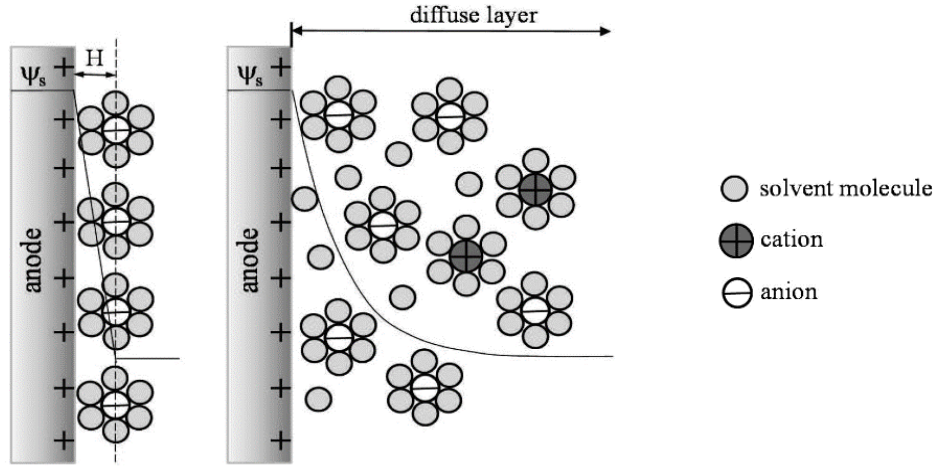
The interaction between the electrode charge and the electrolyte's ionic components is also responsible for the order that develops at the electrode's surface in the form of an electric double layer. This first to conceive of this concept was Helmholtz [49][50]. He

suggested that when a potential is applied to an electrode in an electrolyte, the counter, or opposing, charged ions in solution will be attracted to the electrode surface [49]. This assembly of the positive and negative counterbalanced charges from the electrode and electrolyte at the electrode surface became known as the electric double layer [49]. The counter ions were considered to be adsorbed to the surface of the electrode in the Helmholtz model [49].

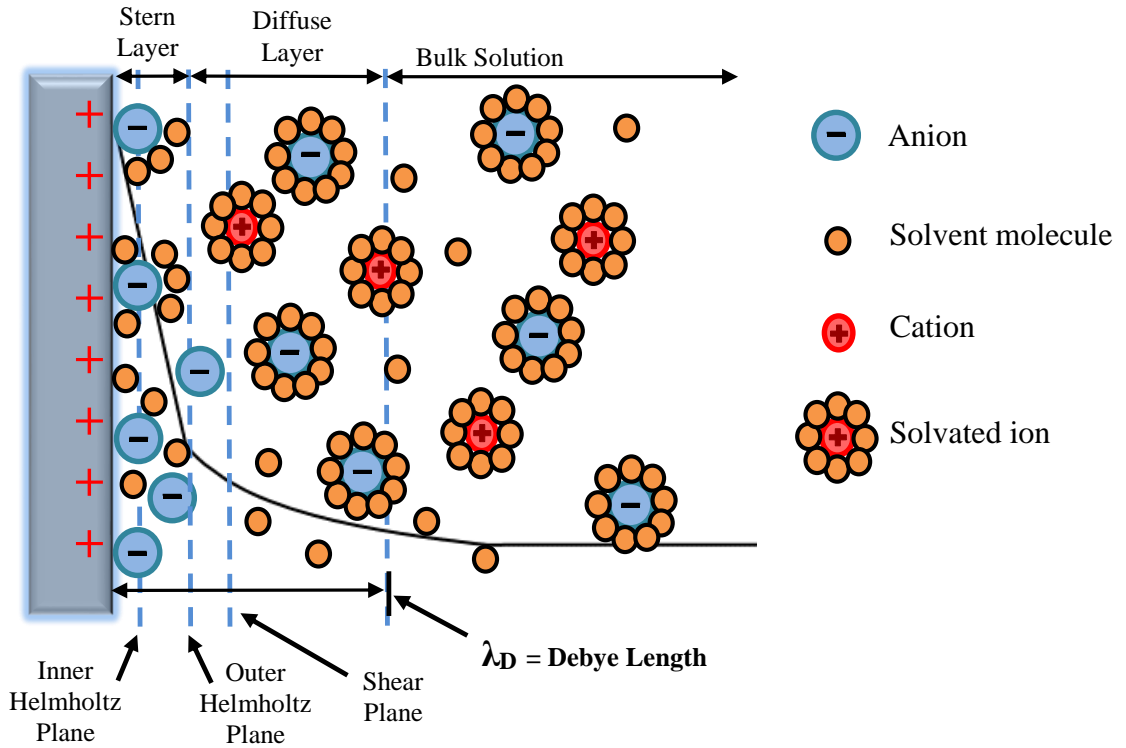
Later, Gouy and Chapman created another version of the electric double layer, emphasizing that ions can move in solution from the influences of diffusion, thermal motion and electrostatic fields [49][51]. In contrast to Helmholtz's model with compacted layers of adsorbed immobilized ions on the electrode surface, the Gouy-Chapman theory refers to "diffuse layer" as where the ions are roaming [49]-[51].

Stern joined the ideas of Helmholtz with the Gouy-Chapman concepts, into what has become called the Gouy-Chapman-Stern model [49]. It described a compacted, immobilized layer of ions with the opposite charge as the electrode at the surface of the electrode as the Inner Helmholtz Plane [49][51][52]. The ions here are defined as being specifically adsorbed [51]. Some model versions express that regardless of the charge on the electrode, anions (negative charge) with their weakly bound solvation shells can be found here chemically bonded with the electrode surface [51][53]. Others accounts indicate that it is the counter ions that strongly make up this adsorbed ion population along the electrode [49][50]. Slightly further from the surface is the Outer Helmholtz Plane where the ions are solvated [24]. When entirely solvated, these ions are referred to as nonspecifically adsorbed [24]. The closest approach these nonspecifically adsorbed ions can make to the electrode surface is limited by the width of their solvation shell plus the monolayer of adsorbed atoms on the electrode [24][53]. Together, the Inner Helmholtz Plane and Outer Helmholtz Plane are termed the Stern layer [51][52]. Beyond the Stern layer is the region where the ions are mobile, as previously defined by the Gouy-Chapman model as the diffuse layer [49]. The diffuse layer can also be described as having a shear plane close to the Outer Helmholtz Plane, as the molecules can move along this delineation [50][54].

Figure 14: Electric double layer theories and illustrations. The potential is indicated by the black line. a) The Helmholtz model with the potential linear through the electrode surface monolayer of atoms and ions. b) The Gouy-Chapman model with mobile ions and curved potential drop (Poisson-Boltzmann equation). c) The combination of a) and b) yielding the Gouy-Chapman-Stern model where there is a compacted layer of atoms and ions along the electrode surface and a diffuse region. Subdividing the regions there is the Inner Helmholtz Plane, Outer Helmholtz Plane and Shear Plane [49]-[53]. The diffuse layer width is characterized by the Debye length [54]. Figure 14a-b reprinted with permission from [49]. Copyright 2011 American Chemical Society.



(a) Helmholtz model (b) Gouy-Chapman model



c) Gouy-Chapman-Stern Model

1.8 Microfabrication Background

Microfabrication techniques include additive, subtractive and photolithography patterning methods to build miniaturized structures. Many techniques for building biomedical sensors have been borrowed or adapted from the semiconductor industry to construct MEMs, BIO-MEMs and BIO-NEMs [26]-[28][53][55][79].

Additive methods are also known as deposition techniques and they use physical or chemical reactions to introduce a layer onto a substrate with good adherence to that substrate [55]. The most straightforward example is spin-on deposition procedures where a liquid is administered to the substrate's surface [55][56]. The substrate, such as a silicon wafer, is then rotated quickly, spreading out the solution on the surface. The rate of speed will determine the thickness of the film. Heating the wafer will drive off the volatile components of the film, leaving behind a solidified film layer. Spin-on deposition methods are used to apply photoresists, polymer layers and some types of glass layers [55][56]. The photoresist can then be made into a pattern and/or pyrolyzed to become an electrode [58].

Physical vapor deposition (PVD) is another kind of additive technique [55][56]. Both the material to be layered and substrate are put into a high vacuum environment ($\sim 10^{-6}$ mTorr) [55]. The deposition material is heated until it evaporates. When the vapor strikes the substrate, which is at a cooler temperature, the vapor condenses on the substrate, forming a thin layer [55]. The heat needed to vaporize the substance can come from contact heating, electron beam heating, positively charged ion bombardment heating (sputtering), or a laser beam [55]. Electron beam (e-beam) is the most efficient at heating the material for deposition and creating vaporized atoms with higher energy levels, to make better quality layers [56].

Chemical vapor deposition (CVD) is another way to deposit material onto a substrate by putting into an atmosphere, or flow, of one or more volatile precursor gas species, under controlled pressure and temperature [55][56]. The reagents at the surface chemically react to deposit a film onto the substrate. The unwanted byproducts or unused gas species are removed, usually with the gas flow [55][56]. There are variations on the CVD technique

theme. When low pressure and high temperature are utilized, then the process is referred to as low pressure chemical vapor deposition, otherwise known as LPCVD [55]. This method can create good quality silicon dioxide and silicon nitride layers under a range of pressures and temperatures upwards of 500 °C [55][60][63][64]. Another variation of CVD is the use of plasma to encourage the production of reactive chemical compounds, referred to as plasma enhanced CVD (PECVD) [55]. By using plasma, the temperature of the reaction chamber can be lower than in LPCVD [55][59][60]. Generally this means below 500 °C, but in practice 300 to 350 °C can produce a high quality silicon dioxide film [59][60]. Unlike in LPCVD where the entire chamber is heated, the RF generator provides the energy for the reaction by exciting (heating and ionization) the gas directly in the PECVD method [55][58]. PECVD is also recognized as a good process to create silicon dioxide (SiO_2), silicon nitride films (Si_3N_4), silicon oxynitride (SiO_xN_y), poly silicon (poly-Si), amorphous silicon (A-Si), amorphous hydrogenated silicon nitride (A-SiN_xH_y) and diamond-like carbon (DLC) [55][59][60][61][62].

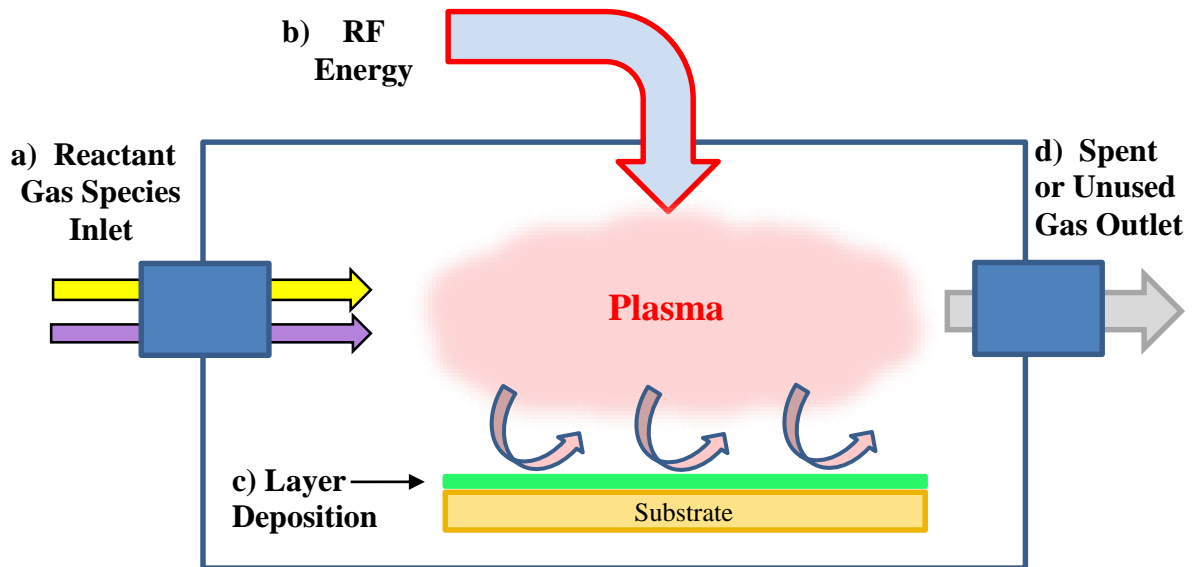


Figure 15: Illustration of the PECVD process [55]-[62][74]. a) Reactant gas species are delivered to the chamber where they are excited by b) RF energy. The excited plasma gas species diffuse to the substrate, react with each other and the surface, and create a deposition of a desired layer on top of the substrate. d) Spent or unused gas is vented out. PECVD can come in a variety of configurations and modalities. These including low to high radio frequency systems, as a parallel plate plasma reactor, downstream (remote) RF inductively couple plasma reactor, linear applicator excitation, plasma impulse CVD (PICVD) excitation, dual-mode Microwave/RF excitation, atmospheric pressure plasma, atomic layer deposition, cascade operation, hybrid PECVD/PVD combining parallel plate RF electrode and magnetron sputtering and other configurations as well [74].

There can also be additive depositions that are not permanent, but temporary, to serve as sacrificial layers. These layers can be transitory protective structures during multi-stage construction steps, be used to create overhangs or gaps, or provide a way to pattern a wafer with lift-off steps [55][56][69]. In a way, they are similar to subtractive techniques since material is removed.

A true subtractive technique, also referred to as a micromachining process, is the use of an etchant to remove substrate material either on the surface or in bulk [55][69][70]. The area to be selectively etched is defined by the use of a mask, which limits the removal of

material to regions in direct contact with the etchant. The zones covered by the mask will not be eroded because the mask physically restricts those areas from contact with the etchant [55][69]. The mask is chosen as having a composition little affected or completely unaffected by the etchant's chemistry with a photoresist being favored [55][69]. The etch rate is an important factor as well, defining how quickly material is removed per unit time (e.g. $\mu\text{m}/\text{min}$, $\mu\text{m}/\text{sec}$, nm/min , etc.) [55][69]. Also critical in etching is the directionality of the etch process. When the etchant consumes material in all directions equally, it is considered an isotropic etchant [69]. The substrate removal can also occur unequally in different directions. This anisotropic etching usually occurs along the crystalline planes of the substrate [69][70].

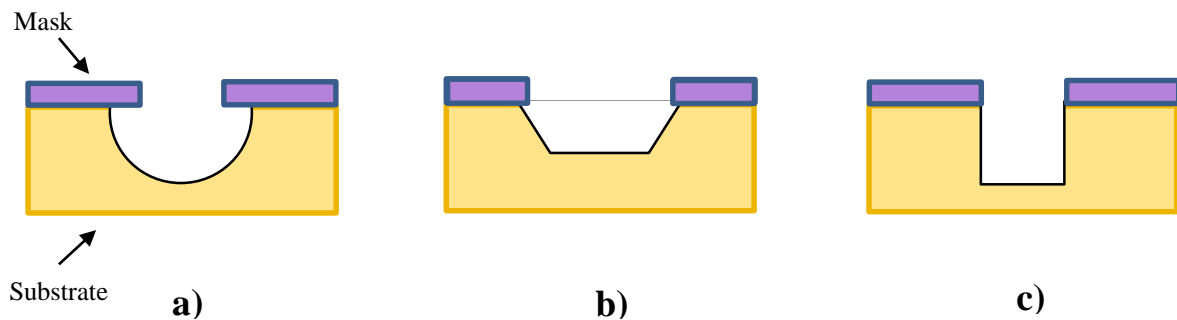


Figure 16: A cross section of etching processes showing removed substrate and a mask unaffected by the etchant [26][55][56][69][70][72][73]. a) In isotropic etching the etchant removes substrate material in all directions equally from the mask window. b) With anisotropic etching, substrate consumption is a function of direction and could be governed by crystalline planes as happens in silicon wet etching. In both a) and b) some underetching of the mask is also illustrated. c) Another example of anisotropic etching as would be expected from reactive gas or plasma (reactive ion etching (RIE)) in dry etching.

When such a fluid based etchant is used, it is referred wet chemical etching [69]. Mixtures based on acids or bases have been developed that predictably and selectively erode substrates isotropically and anisotropically [55][69]. Most etchants have historically been liquids [69].

Dry etching methods are also possible as a subtractive technique. Instead of using a liquid, a reactive gas species or plasma is delivered to the substrate's surface [55][69]. Dry etching is known for its ability to provide a directionality to the material removal, providing a way to make features with near vertical sidewalls [69][72]. The resulting structures can also be large in height compared to their horizontal length scale, or in other words, have a high aspect ratio [56][69][73]. An example of a reactive gas for dry etching is xenon difluoride (XeF_2) which selectively etches silicon or polysilicon, while leaving metals and silicon dioxide untouched [56][69][71]. Plasma for dry etching is produced by exciting a gas with radio frequency (RF) energy [55][69]. The ions then bombard the surface and erode it in one of two ways. If the ion is an inert gas ion, such as Ar^+ , it is the momentum of the ion that knocks away the substrate's atoms in a process called ion milling or the sputter effect [56]. The second way the ion can remove some of the surface is when the ion is not inert, as with oxygen ions, O^{2+} [56]. In these cases the ion interacts with the surface and produces a volatile product that evaporates away in the vacuum [55][56]. This process is called reactive ion etching (RIE) [55][56] [69]. Related to it, is the successive etching process of deep reactive ion etching (DRIE) [55][56] [72][73].

The procedure in microfabrication that brings together the aforementioned additive and subtractive processes is photolithography. Photolithography incorporates these techniques as individual steps which are implemented in a sequentially and controlled by the use of patterned masks. These masks define what areas of the substrate will be affected by the additive or subtractive methods at any particular step in a series of steps referred to as patterning.

The patterns are made with light sensitive polymers called photoresists. They are applied to the substrate after the substrate has been mounted on a specially designed vertical spindle (spinner) with a horizontal platform (chuck) [56]. The chuck provides a vacuum to secure the substrate as it is spun. With the rotation the photoresist spreads across the substrate's surface. The thickness of the photoresist polymer is determined by how quickly the substrate is rotated [56]. The substrate is then put on a hot surface to drive off any

remaining solvent from the photoresist [56]. The substrate, with its newly acquired layer of photoresist, is then exposed to ultraviolet (UV) light through a mask that can be made of chrome on glass. The chrome covered regions of the mask prevent the light from passing through, while the clear parts of the mask's glass allow the transmission of the UV. Whatever pattern that is on the mask, then becomes transferred to the photoresist.

For this procedure to properly work, the mask has to be paired with the appropriate kind of photoresist for its chrome pattern. If a positive photoresist is used with the mask, the photoresist polymer regions exposed to light will be soluble at the development stage, letting those light exposed regions be washed away [69][75][76]. The regions that were not exposed to light will remain behind [69][75][76].

Negative photoresist behaves just the opposite. If a negative photoresist is used with the mask, the photoresist polymer regions exposed to light will be insoluble at the development stage [69] [75][76]. The light exposed features will remain on the substrate, while unexposed regions will be washed away [69][75][76].

An overview of photolithography with additive and subtractive methods can be seen in Figure 17.

The future direction of microfabrication will include shorter light wavelengths, as in extreme ultraviolet lithography, to improve photolithography resolution [75]. Other techniques will also try to use technologies that avoid using light. These methods include proximity x-ray, electron-beam direct write, electron projection, ion-projection lithography, nanoimprint lithography and directed self-assembly [75].

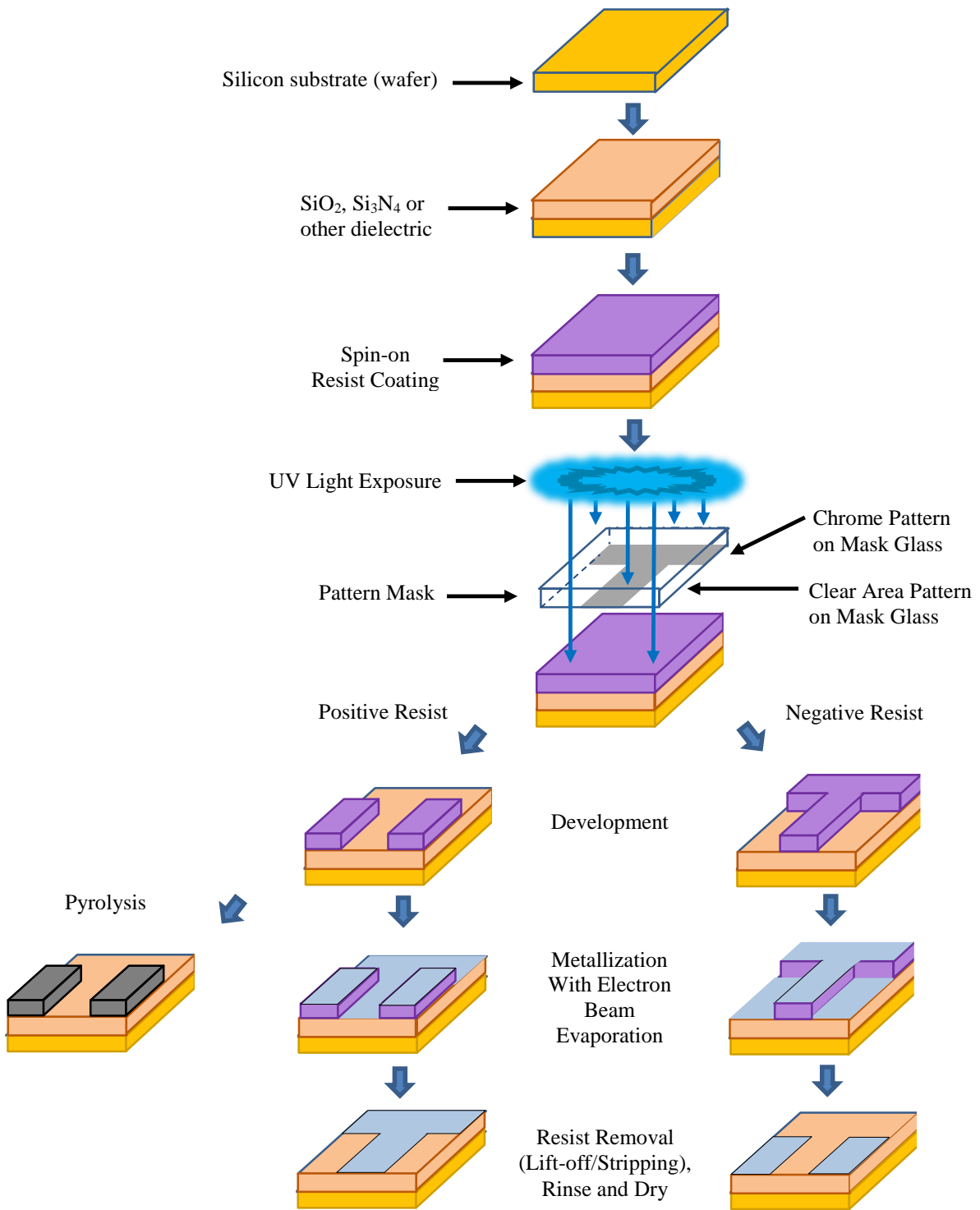


Figure 17: An overview of photolithography with additive and subtractive methods, resulting in carbon pyrolyzed film and metal deposition examples [26][55][56][58][69][75]-[78].

1.9 Organization of this Thesis

- Chapter 1 presents a brief description of the project and the necessary background information for the thesis. This background information includes sensor technique overview and current literature, electrochemical detection, chronoamperometry, dopamine as an electroactive species, electrode surface chemistry and physics, microfabrication and the importance of dopamine.
- Chapter 2 explains the sensor fabrication and experimental design of the project.
- Chapter 3 shows the results of the experiments with discussion.
- Chapter 4 summarizes the conclusions.
- Chapter 5 presents possibilities for future work.

Chapter 2 Sensor Fabrication and Testing Protocols

2.1 Platinum Microelectrode Sensor Fabrication

The platinum sensors were microfabricated using a multiple step approach outlined in Figure 18 and Figure 19. The sensors were made on a 200 μm silicon wafer and insulated with a 3250 \AA thick layer of LPCVD silicon nitride (Si_3N_4). The wafer was then cleaned with JT Baker solution and coated with 2 μm layer of JSR NFR photoresist. The photoresist was patterned and then developed with MF-319. The pattern was then RIE etched to a depth of 65 nm. The patterned channels were first filled with a 5 nm titanium adhesion layer followed by a 60 nm deposition of platinum. A liftoff was then done in a bath of acetone with sonication. Measurements have shown the newly deposited metal is flush with the LPCVD nitride layer's surface and a profilometer is unable to distinguish where the nitride ends and the platinum begins.

Next, another layer of insulating silicon nitride was deposited with plasma enhanced chemical vapor deposition (PECVD). With S1813 photoresist a pattern was made. Reactive ion etching (RIE) with CHF_3 was then used to selectively to etch the PECVD nitride to open

a small window in the nitride. This allowed the platinum electrodes to interact with the dopamine solution in those etched areas. The wafer was then coated with AZ4620 photoresist to help strengthen the wafer from during the dicing step and prevent fracturing. The devices were then individually diced out of the silicon wafer using a dicing saw. Lastly, the sensors were cleaned with acetone and deionized water prior to use. The fully fabricated platinum sensor can be seen in Figure 20.

Once completed, the sensor was adhered to a glass slide. A sheet metal mold was placed on top of the sensor, and hot wax was poured into it. When the wax cooled, the metal was removed and the wax formed a solution reservoir as seen in Figure 23. At this stage, the sensor was ready to be tested and could be mounted in the probe testing station as shown in Figure 24.

Platinum Sensor Microfabrication Process

a) Silicon Wafer Substrate



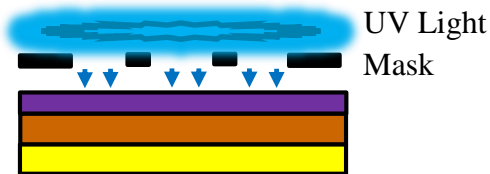
b) 3250 Å LPCVD Silicon Nitride deposited



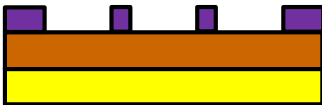
c) 2 μm layer of JSR NFR photoresist added



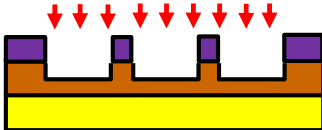
d) UV Pattern the Photoresist



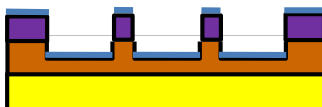
e) Develop pattern with MF 319



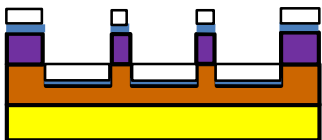
f) RIE with CHF₃ etch 65 nm



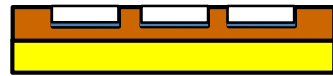
g) Deposit 5nm Titanium Adhesion Layer



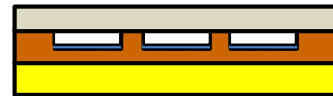
h) Deposit 60nm Platinum



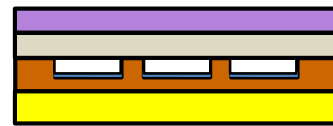
i) Lift-off in sonicated acetone bath



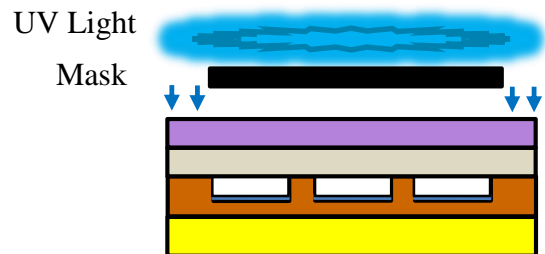
j) PECVD Silicon Nitride deposited



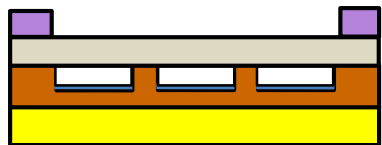
k) S1813 photoresist deposited



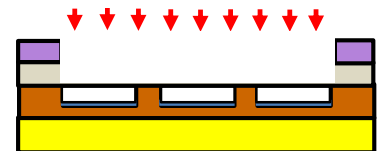
l) UV Pattern the Photoresist



m) Develop pattern with MF 319



n) RIE with CHF₃ etch through PECVD silicon nitride to make window where electrodes can contact the solution

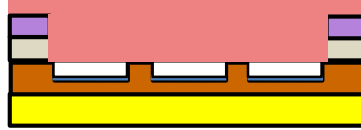


*) Continued in Figure 19

Figure 18: The platinum sensor microfabrication process.

*) Continued from Figure 18

o) Coat wafer with AZ4620 photoresist to strengthen the wafer prior to dicing from wafer



p) Clean diced sensor with acetone and deionized water

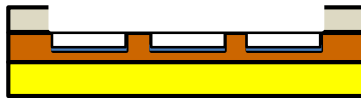


Figure 19: Continuation of the platinum sensor microfabrication process.

Platinum Microelectrode Sensor

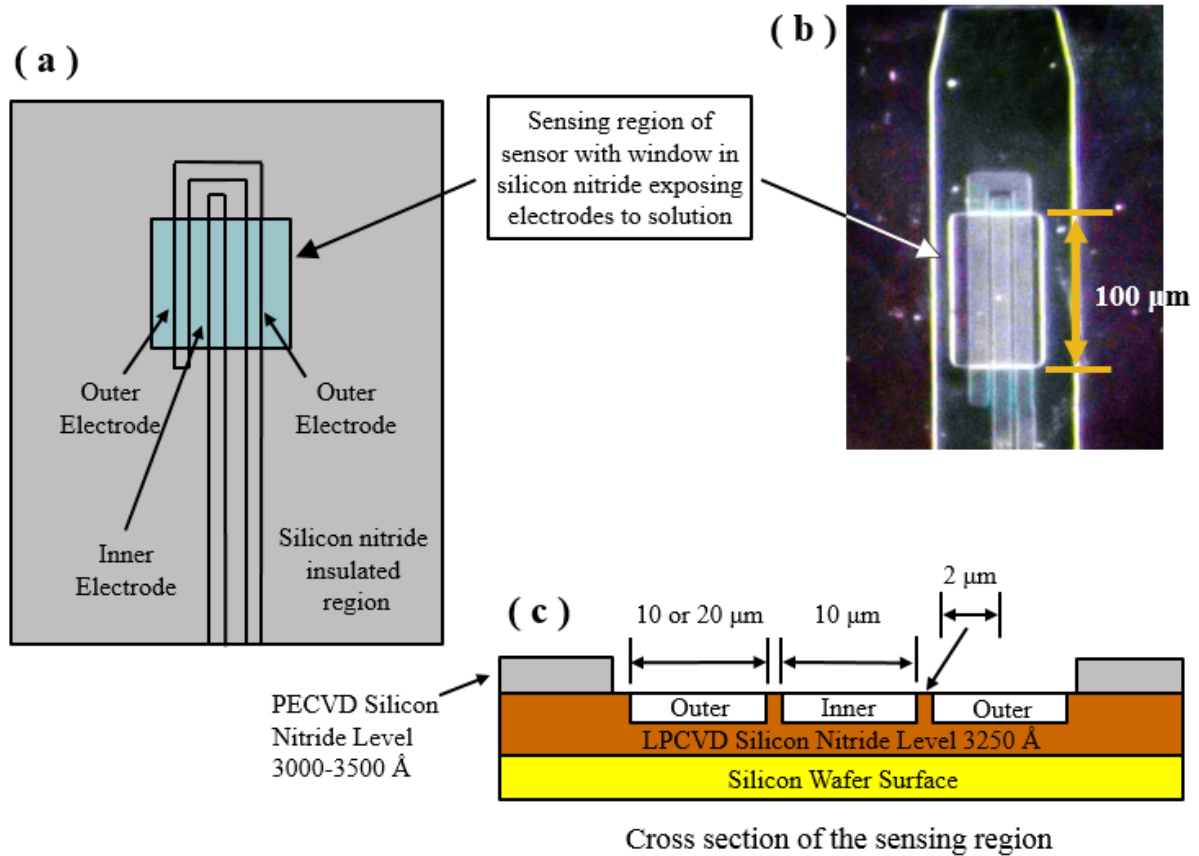


Figure 20: Platinum microelectrode sensor design. (a) A schematic showing the layout of the sensor. (b) A picture of a used platinum microelectrode sensor. Crystallized, white salt crystals from dried PBS solution are visible. (c) A cross-sectional schematic of the platinum sensor. The inner electrode was always 10 μm wide and 100 μm long with the gap between the inner and outer electrodes being 2 μm . The outer electrode of the tested population of sensors was either 10 μm or 20 μm wide and 100 μm long.

2.2 Carbon Pyrolyzed Photoresist Film (PPF) Microelectrode Sensor

The carbon PPF (Pyrolyzed Photoresist Film) sensors were microfabricated on a 200 μm silicon wafer substrate. First the wafers were JT Baker cleaned. Then an insulating layer

of silicon nitride (Si_3N_4) was deposited with LPCVD to a 3000 Å thickness on the wafers. A dehydration bake was then performed followed by an HMDS application to remove any remaining water. Photoresist AZ1518 was then applied at 2750 rpm resulting in a 2 µm thick coating. This photoresist was then soft baked and patterned, and subsequently developed with CD-26. After a rinse with deionized water rinse and drying via N₂ gun, the wafer is hard baked for 5 minutes at 115 °C. The wafer was then air plasma (descum) treated for 20 minutes. Next, the photoresist was pyrolyzed by having the wafer placed in a quartz tube furnace. The temperature was gradually ramped to 1000 °C and held for an hour in an inert atmosphere of 95% N₂ and 5% H₂, and then temperature was then ramped down over a period of hours.

An additional layer of nitride is then deposited with PECVD to a thickness of 5000 Å. The wafer is then treated with MCC Primer at 3000 rpm for 30 seconds. This treatment was followed by an S1813 photoresist patterning and soft bake at 115 °C for 1 minute. The S1813 photoresist was developed with MF319 for approximately 1 minute. A hard bake was next done at 115 °C for 5 minutes. The PECVD nitride was then RIE etched with CHF₃ to make windows in the insulating layer that allow the electrodes to interact with the dopamine solution. A Nanostrip treatment was then performed with Nanostrip 1 for 20 minutes and Nanostrip 2X for 10 minutes to remove resist and other organic materials. The wafers were then rinsed off with deionized water.

Another photoresist coating with AZ4620 was applied in preparation of dicing. The photoresist was spun on at 1800 rpm for 1 minute. The AZ4620 gave some structural support to prevent the wafer from fracturing during the dicing process. UV release tape was also put on the wafer to give additional strength to the wafer. The carbon PPF devices were then individually diced out of the wafer with a dicing saw. A UV light oven released the tape from the devices. The AZ4620 is then rinsed off with two baths of acetone and a deionized water bath. The carbon PPF sensor fabrication process is diagrammed in Figure 21.

Stainless steel wires were silver epoxied to the carbon pads of the devices and then secured with clear epoxy. The completed fabrication of a carbon PPF sensor can be seen in Figure 22.

Once fabricated, the sensor was adhered to a glass slide. A sheet metal mold was placed on top of the sensor, and hot, liquid wax was poured into it. When the wax cooled and solidified, the metal mold was removed and the wax formed a dopamine solution reservoir as seen in Figure 23. At this stage, the sensor was ready to be tested and could be mounted in the probe testing station as shown in Figure 24.

Carbon Pyrolyzed Photoresist Film (PPF) Sensor Fabrication Process

a) Silicon Wafer



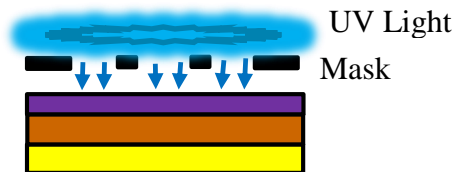
b) 3000 Å LPCVD Silicon Nitride Deposited



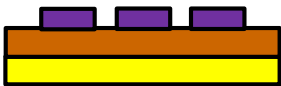
c) 2 μm layer of AZ1518 photoresist added



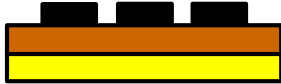
d) UV Pattern the Photoresist



e) Develop with CD26



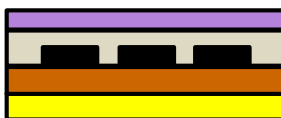
f) Pyrolyze the photoresist



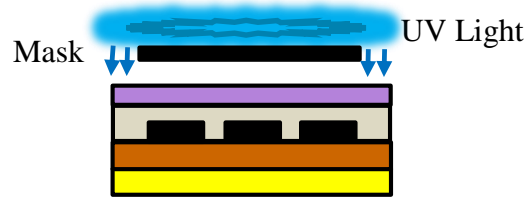
g) 5000 Å Silicon Nitride deposited



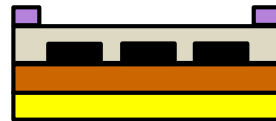
h) S1813 photoresist deposited



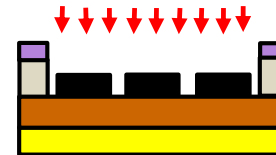
i) UV Pattern the Photoresist



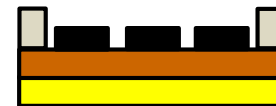
j) Develop with MF 319



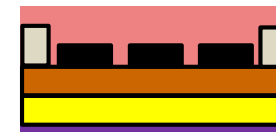
k) RIE Etch with CHF₃ to make window in PECVD silicon nitride layer to allow electrodes to contact the solution



l) Use Nanostrip product to remove resist and clean surface



m) Coat wafer with AZ4620 photoresist (top) and apply UV sensitive tape (bottom), both to strengthen the wafer prior to dicing



n) Treat diced sensor with UV to release tape and remove the AZ4620 resist with acetones baths and deionized water

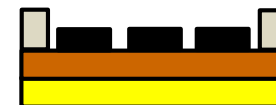


Figure 21: Carbon pyrolyzed photoresist film (PPF) sensor microfabrication process.

Carbon PPF Microelectrode Sensor

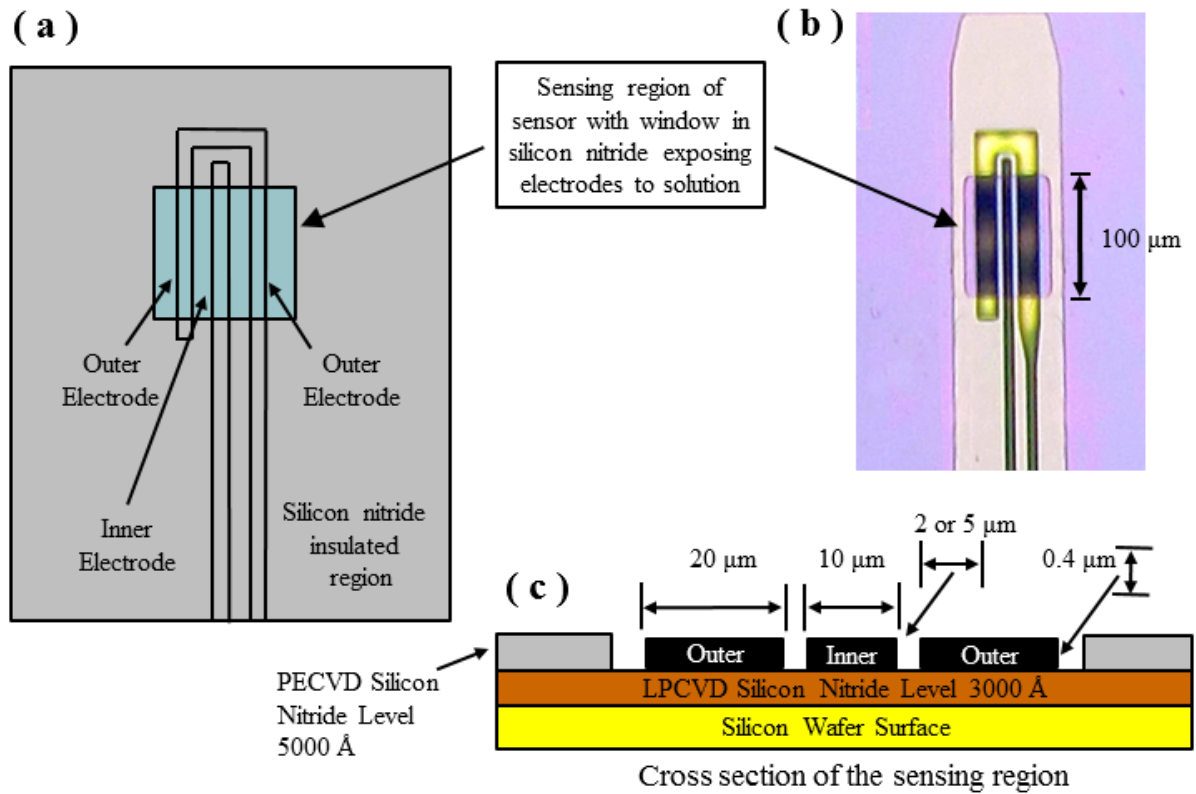


Figure 22: Carbon PPF microelectrode sensor design. (a) A schematic showing the layout of the sensor. A noticeable difference between the carbon PPF sensors and the platinum sensors is that the PPF electrodes sit atop of the LPCVD nitride rather than being embedded in it as for the platinum sensor. (b) A picture of a used carbon PPF microelectrode sensor. The lighter area in the vertical center of the electrode bands is due to a light reflection from the PPF surface. (c) A cross-sectional schematic of the platinum sensor. The inner electrode was always 10 μm wide and 100 μm long with the gap between the inner and outer electrodes being 2 or 5 μm in this population of sensors.

2.3 Platinum and Carbon PPF Sensor Mounting for Testing

The mounting of the platinum and carbon PPF sensor to a glass slide and dopamine reservoir can be seen in Figure 23.

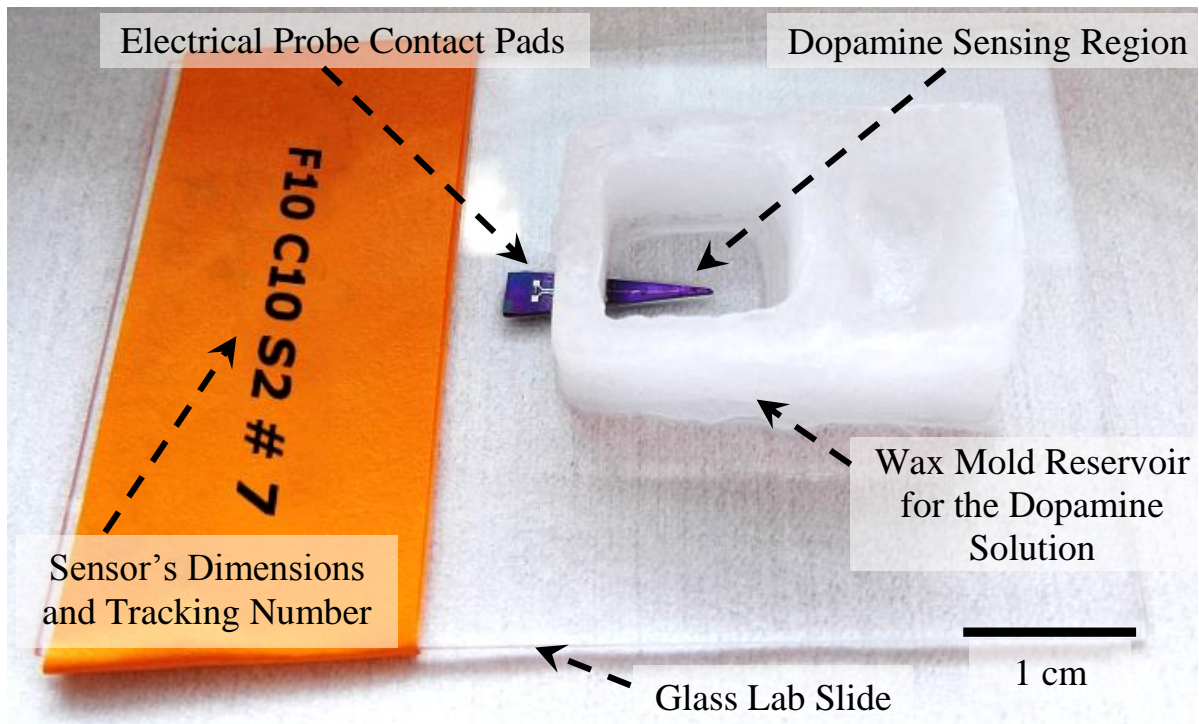


Figure 23: The mounted dopamine sensor, ready for testing on the probe station. Platinum and carbon PPF sensors looked nearly identical at this stage. The only difference was that for the carbon PPF sensors stainless steel wires were attached to the contact pads with conductive epoxy.

The platinum and carbon PPF sensor mounted and on the probe station can be seen in Figure 24.

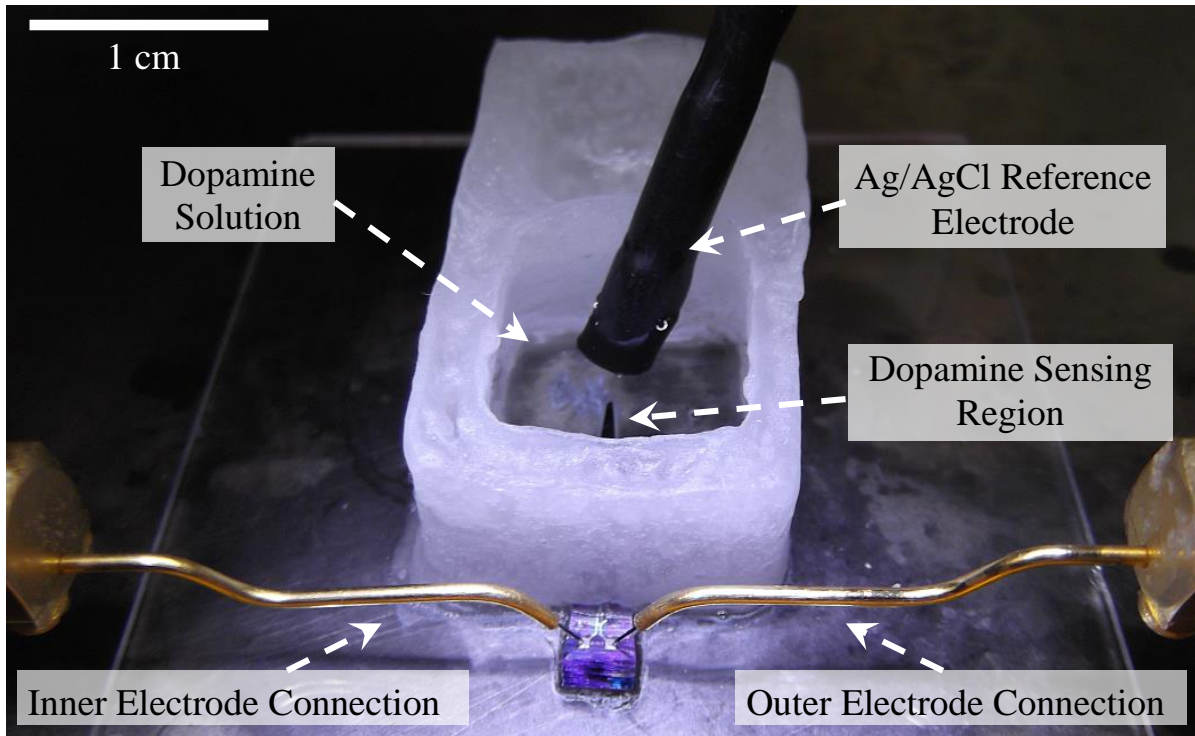


Figure 24: The dopamine sensor mounted on probe station for testing. Platinum and carbon PPF sensors looked nearly identical at this stage. The only difference was that for the carbon PPF sensors stainless steel wires were attached to the contact pads with conductive epoxy. The inner and outer electrode connectors were placed in contact with those wires.

2.4 Circuit Design and Experimental Setup

Two trans-impedance amplifiers, also called current to voltage amplifiers, were used in the chronoamperometry experiments. Both amplifiers were constructed with low noise Op-Amps. One trans-impedance amplifier was connected to the inner electrode and the other trans-impedance amplifier connected to the outer electrode of the sensor. A data acquisition (DAQ) board controlled the voltage applied to the non-inverting terminals of the

two Op-Amps of the trans-impedance amplifiers. This application of voltage then controlled the voltage at the inverting terminal which controlled the voltage on the sensor's electrodes. The resulting current could be detected on the output of the amplifier and recorded via the DAQ. This circuit can be seen in Figure 25.

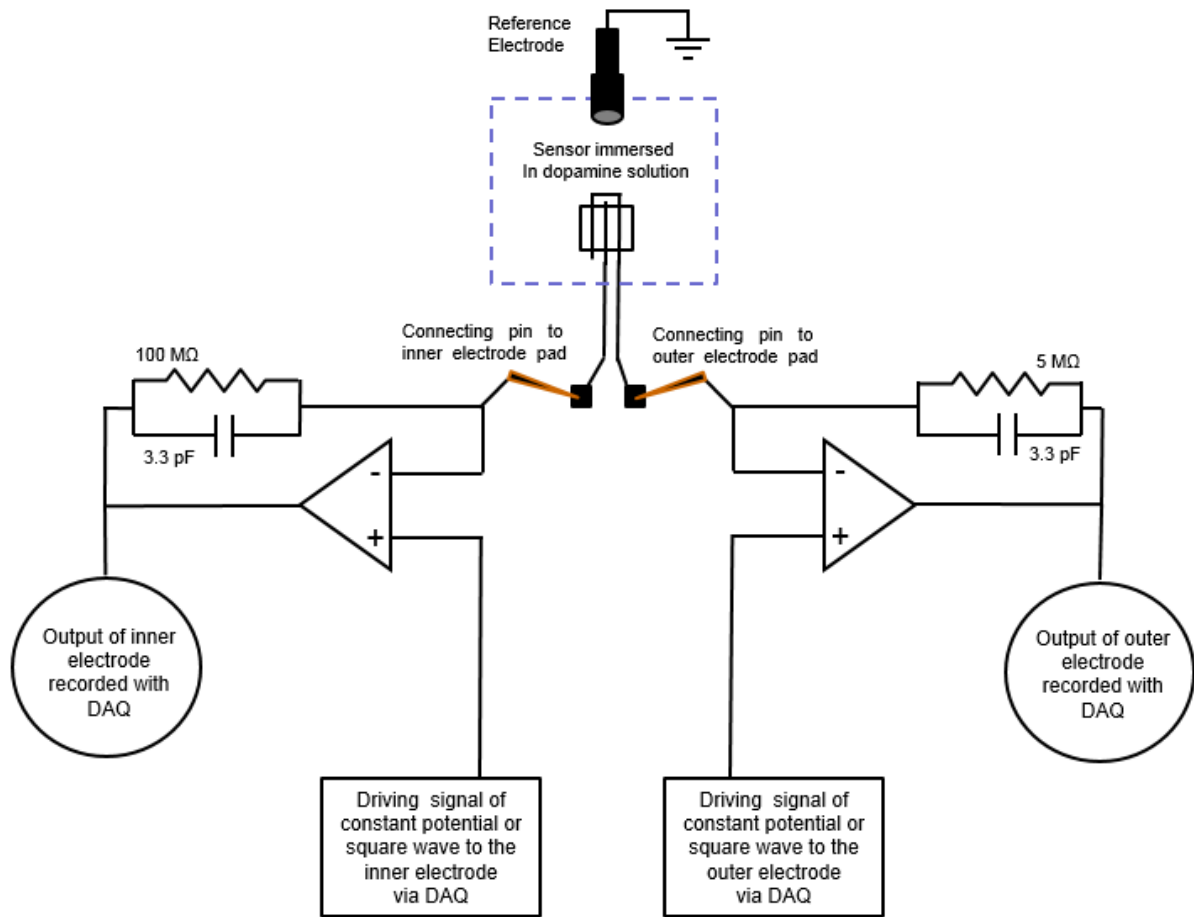


Figure 25: The transimpedance amplifier circuit. The feedback resistor governed the gain of the amplifiers. A higher gain was used on the inner electrode of the sensor. The capacitor helped stabilize the response and did not reduce the signal in the used frequency range.

Some more circuit detail is offered in Figure 26. A low ripple, 15 V power supply was used. In practice it was found that the signal to noise ratio was better when the grounds between the 1 μ F capacitors were wired to each other before connecting to ground.

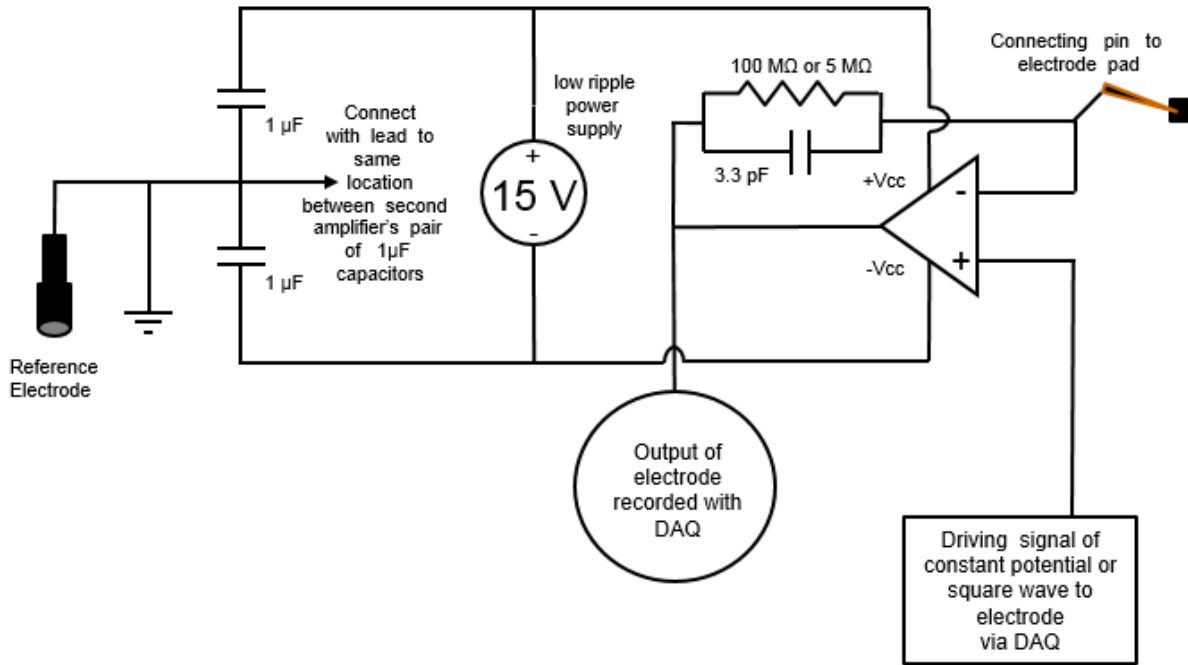


Figure 26: More detail on the amplifier circuit. The schematic represents half the circuit from Figure 25. A 15V low ripple power supply was used and connecting the pair of 1 μ F capacitors between amplifier circuits improved the signal to noise ratio.

The amplifiers and their surface mount capacitors were cocooned in 2 part epoxy resin. The epoxy protected the surface mount components and prevented any accidental shorts. The quantity of epoxy used was not much more than what was required to minimally cover the components. Experience proved that using too much epoxy could generate enough heat during the exothermic curing process to destroy the amplifiers.

To give further protection, the epoxy was tightly covered in heat shrink wrap tubing. Placement of the amplifier close to the sensor lessened environmental electrical noise. The

amplifiers were connected via a shielded flexible cable to the multi-pin adaptor that supplied power and connection to the DAQ. Completed amplifiers can be seen in Figure 27.



Figure 27: The completed construction of the amplifiers and their connectors. The amplifiers are entombed in epoxy resin and surrounded by the black shrink wrap tubing as seen on the left side in the picture. Of the pair of wires protruding from each amplifier, one was for sending the voltage signal to the inner or outer electrodes and the other wire was for ground. The right side of the picture shows the interface to power and DAQ connections.

2.5 Experimental Protocol

2.5a Reagents, Instrumentation and Software

Dopamine was purchased from Sigma-Aldrich (St. Louis, MO). Phosphate Buffered Solution (PBS) 10X was obtained from Fisher Scientific (Hampton, New Hampshire). It was diluted to 1X (1.37 mM Sodium Chloride, 2.7mM Potassium Chloride, and 11.9mM Phosphates) with distilled water and to have a final pH of 7.4. The paraffin wax used to mold the dopamine solution reservoir around a sensor was from Gulf Wax (Roswell, GA).

The S1813 photoresist came from Shipley (Marlborough, MA), the JTB-100 Baker cleaning solution came from Avantor Performance Materials (Center Valley, PA), the AZ4620 and AZ1518 photoresists came from AZ Electronic Materials (Branchburg, NJ), the

MF319 and CD26 developers were from Rohm & Hass (Philadelphia, PA), the JSR NFR photoresist was from JSR Microelectronics (Sunnyvale, California), the MCC Primer was made by Microchem (Newton, MA), and the Nanostrip and Nanostrip 2X were from Cyantek (Fremont, CA).

Cleanroom fabrication was performed at the University of North Carolina at Chapel Hill Analytical and Nanofabrication Laboratory (CHANL), North Carolina State University Biomedical Department Cleanroom and the North Carolina State University Nanofabrication Facility (NNF). Adam Dengler, a PhD candidate for Dr. McCarty, was responsible for the carbon PPF sensor fabrication. Lindsay Walton, a PhD candidate for Dr. Wightman and Dr. McCarty, was responsible for the platinum sensor fabrication.

The trans-impedance amplifiers, also called current to voltage amplifiers, were constructed from low noise, precision AD795 operational amplifiers (Analog Devices) purchased from DigiKey (Thief River Falls, MN). The surface mount capacitors and resistors, BNC connectors, as well as cables and interface ports were also acquisitioned from DigiKey. The coaxial cable leading from the amplifier to the probe station coaxial wire was bought from Cooner Wire (Chatsworth, CA).

The analytical probe station was made by Cascade Microtech (Beaverton, OR) and used both Cascade Microtech probe holders and Cascade Microtech 5 μm probes.

Measurements were recorded with a National Instruments NI PXI-6229 data acquisition board interfaced through a Windows based PC. A custom made program created in LabVIEW was used as the software controlling the data acquisition. Data processing was then done with Excel and several programs created in Excel. Automation of testing and processing was also accomplished.

For both types of sensors, an Agilent technologies DSO6032A oscilloscope was used concurrently with the testing to display the sensor responses in real time. Also an Ag/AgCL electrode was used as the reference electrode. All measurements were carried out at room temperature and the dopamine solution was exposed to the ambient atmosphere.

2.5b Testing Protocol and Amperometry responses

Each platinum and carbon sensor was tested for at least 5 concentrations of dopamine solution. Both types of sensors underwent the same testing protocol. The testing protocol consisted of a series of waveforms and constant voltage application to the outer and inner electrodes. These tests were based on the electrochemical properties of dopamine. These included dopamine oxidizing at 0.7 V into dopamine-ortho-quinone (dopamine-o-quinone) and dopamine-o-quinone being chemically reduced to dopamine at -0.4V. Below is a table showing the performed tests.

Table 1: Applied Waveforms and Potentials to Outer and Inner Electrodes

Scenario	Outer Electrode	Inner Electrode
1	Square Wave -0.4V to +0.7V, 10 sec cycle	Constant -0.4V
2	Square Wave -0.4V to +0.7V, 10 sec cycle	Constant +0.7V
3	Constant 0V	Square Wave -0.4V to +0.7V, 10 sec cycle
4	Square Wave -0.4V to +0.7V, 10 sec cycle	Constant 0V

A typical sensor response curve for the Scenario 1 test can be seen in Figure 28. The other testing scenarios would have similar current attenuation responses, though at different starting points depending on the polarity of the waveform input.

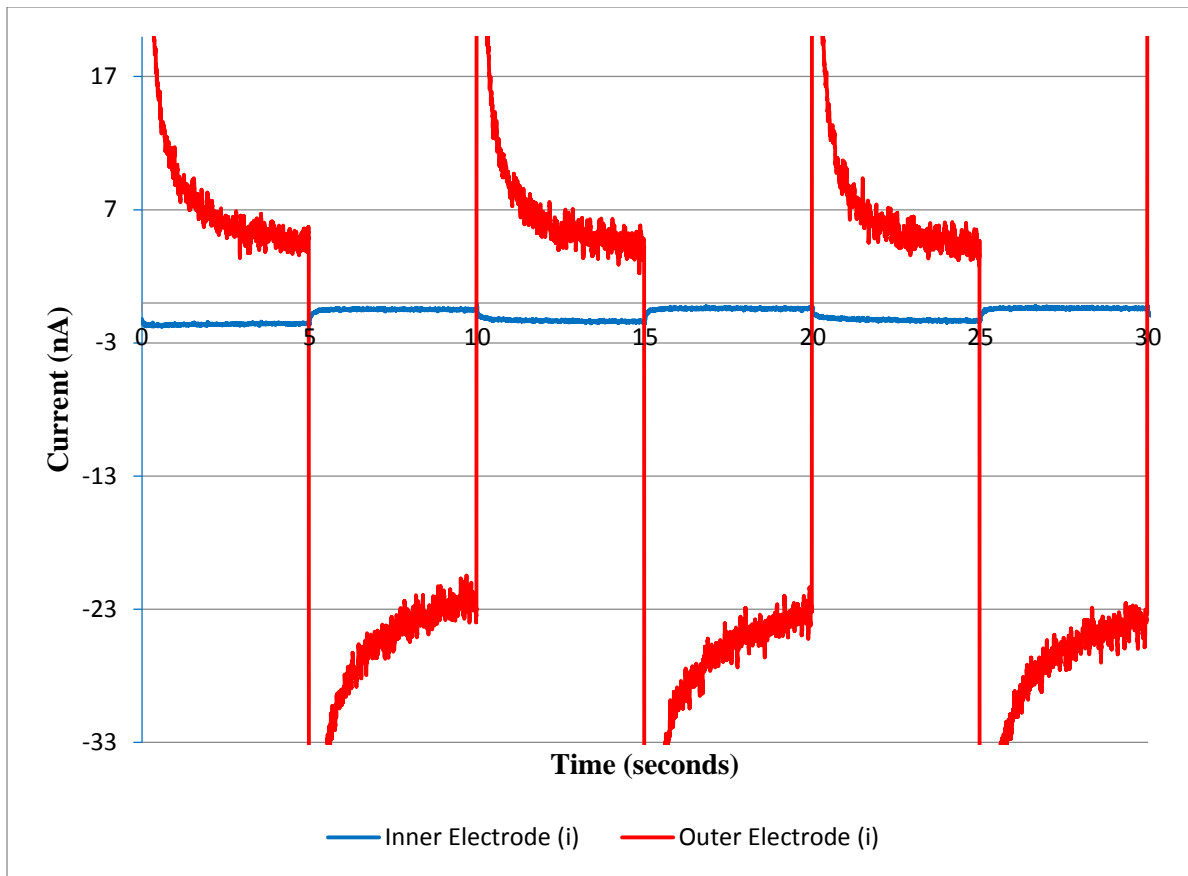


Figure 28: A typical looking sensor response. This was for a Scenario 1 test with the outer electrode going from -0.4V to $+0.7\text{V}$ in a double potential step. The other testing scenarios would have similar current attenuations, but with different starting points depending on the polarity of the input. The variation in current in the current comes from electronic noise in the system and possibly from the extension/contraction of the electrode diffusion layer [2].

For each dopamine concentration, testing scenarios 1 through 4 (Table 1) were automatically tested in sequence for every sensor, with each test lasting approximately 60 seconds. When a square wave was applied, its period was 10 seconds. By having a test last a few times longer than the period, several full repetitions of sensor responses could be collected. This allowed to verify response repeatability and to examine if any trends that occurred while testing. For all tests, the data sampling rate was 400 Hz.

With the full square wave being 10 seconds, half the period is spent at either the oxidizing or reducing potential. This is also the time that the oxidizing or reduced product is diffusing toward the opposite electrode. Reaching the opposing electrode is done very quickly. The actual time to shuttle from one electrode to the other can be estimated from (1), the general solution of the one-dimensional diffusion equation [102].

$$\Delta x^2 = 2D \Delta t \quad (1)$$

In the equation, the distance between electrodes is represented by x , the diffusion constant is D , and t , is time, measured in seconds. By adjusting the terms, an expression for the average shuttling time between electrodes is achieved in (2).

$$\Delta t = \frac{x^2}{2D} \quad (2)$$

With a D for dopamine of $5.4 \times 10^{-6} \text{ cm}^2/\text{sec}$ [101], there is a range of the shuttling time from one electrode to the other, dependent on the gap between electrodes. The predicted shuttling time for the $2 \text{ }\mu\text{m}$ gap electrodes is 0.0037 seconds, while the anticipated time for the $5 \text{ }\mu\text{m}$ gap is naturally longer at 0.0231 seconds.

Another time interval that was part of the experimental setup had nothing to do with testing but should be mentioned for completeness. Between tests 1, 2, 3 and 4, there was approximately 15 seconds wait time where the sensor was not oxidizing dopamine or reducing dopamine-o-quinone. This was the amount of time the automation program took to reset the system for the next test. Data for each test was recorded via the DAQ at 400 Hz in a text file to be processed later.

The data collected was the output of the transimpedance amplifiers which converted the electrolytic surface interaction current to voltage. The electrolytic current recorded indicates interaction between the sensor surface and the dopamine molecules in the solution as indicated in Figure 12 and Figure 13. As a quick review, the dopamine molecules on a positive 0.7V potential electrode surface can donate electrons and oxidize into dopamine-o-

quinone. The newly formed dopamine-o-quinone can absorb electrons at a -0.4V potential electrode. In either case, the interaction will register as a current.

This type of surface chemistry means that recordings of electrical current in electrochemistry has to be thought of differently in contrast to the more traditionally defined circuit-confined motion of electrons (or holes) of electrical engineering. In the context of this experiment, this means there is direct correlation between the electrolytic current recorded from the electrodes and the number of molecules interacting with the electrodes.

Scenario 1 of Table 1 had the outer electrode cycling between dopamine's oxidation and dopamine-o-quinone's reducing potential. This test's purpose was to evaluate the outer electrode's current increase with dopamine concentration. Also with the inner electrode at -0.4V, the test could show if dopamine-o-quinone produced at the outer electrode could be reduced back to dopamine by the inner electrode. If increasing dopamine concentration would show increasing current on the inner electrode, then there would be evidence for redox cycling. These sensors could then be characterized as a collector-generator system and the efficiency could also be examined. Scenario 1 was a double potential step chronoamperometric test for the outer electrode and a holding potential chronoamperometric test for the inner electrode.

Scenario 2 of Table 1 also had the outer electrode cycling between dopamine's oxidation potential and dopamine-o-quinone's reducing potential. In this case, however, the inner electrode's potential was changed and held at +0.7V. This scenario was meant to examine if the outer electrode could screen or reduce the amount of dopamine that could be oxidized by the inner electrode when both the inner and outer electrodes were at +0.7V. In other words, this test probed how much one electrode influences in the other. Scenario 2 was a double potential step chronoamperometric test for the inner electrode and a holding potential chronoamperometric test for the inner electrode.

Scenario 3 of Table 1 examined a different area of interest by keeping the outer electrode at 0 volts while the square wave from -0.4V to +0.7V was applied to the inner electrode. This could show if the inner electrode influenced the outer electrode while held at

a potential. If so, this would mean that the value would be a candidate for baseline subtraction. Scenario 3 was a single potential step chronoamperometric test for the inner electrode (with a -0.4V holding potential between oxidation potentials) and a zero voltage holding potential test for the inner electrode.

Scenario 4 of Table 1 also probed the interaction between the electrodes. In this case this was accomplished by holding the inner electrode at 0 Volts while applying a square wave to the outer electrode. As with Test 3, if there was an influence on the electrode being held at 0V, this could be a candidate for later baseline subtraction. Scenario 4 was a single potential step chronoamperometric test for the outer electrode (with a -0.4V holding potential between oxidation potentials) and a zero voltage holding potential test for the inner electrode.

Initially it was noticed that the sensors were not giving linear response in very straightforward situations, such as when one electrode was stepped up to +0.7V and the other held at 0V. Various solvents and combinations of them were used on the sensors between test runs to try to clean any debris or chemical fouling which could be occurring. These attempts included utilizing acetone, methanol, isopropyl alcohol, distilled water and xylene. Even the use of sulfuric acid was attempted as a cleaning agent. Utilizing the solvents or the acid as a cleaner did not result in permanently improved sensor performance. Initially the sensors would regain their responsiveness to the solution, but after about 3 test runs of 4 Scenarios (3 repetitions of Table 1), the sensors would inevitably lose their responsiveness. The eventual loss of sensor performance can be seen in Figure 29 for both platinum and carbon PPF sensors. As can be seen, platinum also fouls before the carbon PPF sensor.

Dopamine is known to foul electrodes by polymerizing on the surface when the solution concentration is large. Experimentally it was noticed in this work that all concentrations of dopamine eventually darkened and left a film on beakers. It was hypothesized that such a deposition on sensors might be occurring and would need to be cleaned off to restore sensor performance.

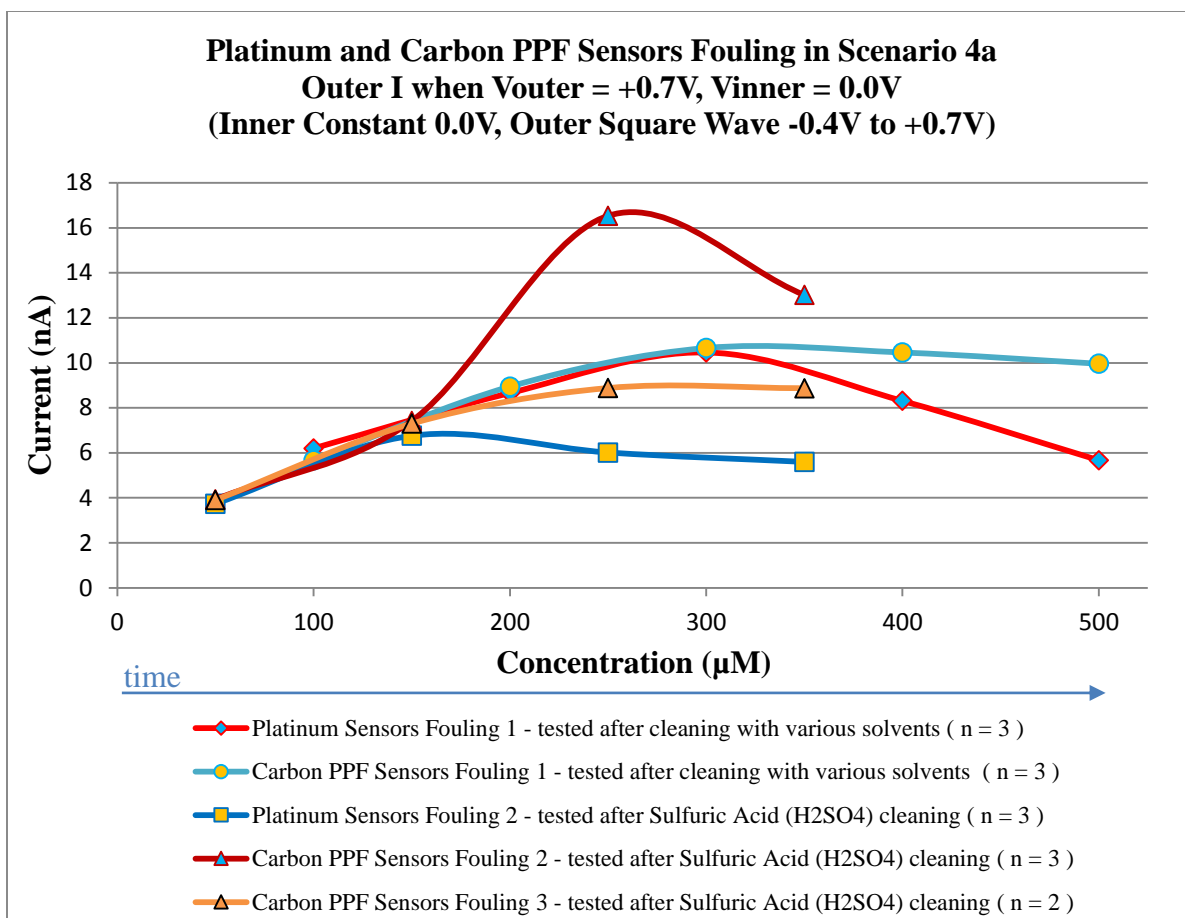


Figure 29: The graph shows the loss of sensor performance with the number of trials performed due to fouling. In this case, the trial also correlates to an increase in dopamine concentration after the sensors had been cleaned. It is not the concentration increase here that is solely responsible for the reduced response of the sensors. The repeat usage of the sensors played a significant role in encouraging fouling. The 2 different starting points (50 µm and 100 µm) and other observations helped elucidate this deduction. The fouling of platinum and carbon PPF sensors following solvent and acid cleaning was a repeatable issue. The cleaning solvents attempted were acetone, methanol, isopropyl alcohol, distilled water and xylene. The acid tried was sulfuric acid. Generally the sensors would initially have a good response following cleaning. However, they would begin to exhibit a weakened response from fouling after a few repetitions of testing (about 3 repetitions of the Table 1 tests). The line showing ‘Carbon PPF Sensors Fouling 3’ is the same population of sensors, as in ‘Carbon PPF Sensors Fouling 2’ except with 1 sensor’s data removed from the dataset. That sensor would foul too, but it would take an additional round of testing for its response to decline. The difference with that sensor is that it had a 2 µm gap instead of the 5 µm of the other two. This could indicate a smaller electrode gap may delay fouling.

A way to prevent sensor fouling was eventually discovered through experimentation. By applying a -1.5V, 0 to +1.5V potential signal at 10Hz for approximately 7 seconds simultaneously to both inner and outer electrodes, the electrodes were electronically cleaned. Following this treatment the sensors response became a linear output which was used for the rest of this work. Prior to every dopamine concentration measurement, an automated auto-cleaning program would be initiated that applied this electronic cleaning methodology. The cleaning's placement in the sequence of events can be seen in the flowchart of Figure 30.

The mechanism of cleaning is hypothesized to be a brief moment of electrolysis that produces oxygen to break down any adhered films and possibly some electrophoresis effects as well to cause movement of the fouling layer away from the electrode surfaces.

2.5c Processing Data

The data was processed in several steps via different programs run in succession. Complete automation was employed where possible. To begin with, the known applied voltage of the square wave or constant potential was subtracted out from every measured voltage at every data point. The resulting voltage difference could then be used to determine the current by dividing the voltage difference with the value of the feedback resistor in the Op Amp. A nine point moving average was then applied to initially smooth the current data. A secondary smoothing was then done with a plus and minus 60 point moving average.

Another program would then retrieve the smoothed value of the currents. The values retrieved were from the second cycle on the outer electrode when the square wave was at the high and low potential. The same sampling would be done for the inner electrode. The values of the first period was skipped because it was observed that sensors would often need at least one cycle to equilibrate their response following a cleaning. The process flow of events and automation programs can be seen in Figure 30.

Being able to create programs for the sensor testing and data collection was crucial in producing enough measurements to evaluate if batches of sensors were correctly working, fouling (Figure 29), or if there was success in electronically cleaning the sensors. To manually collect the data initially was a slow process. It would take several hours to collect

about 8 or 9 tests and this might represent 1 or 2 sensors being tested. As a result of the length of time, the dopamine solution would need to be changed and remade due to its oxidation tendency when exposed to air. Each new batch of solution would be slightly different than the previous one due to measurement variations, introducing undesired deviations in the sensor response too. With programming automation, approximately 80 tests could be done in about the same time amounting to about a 10 fold improvement. A day's work with automation then represented what would take almost a week to do previously. And a few days' work utilizing the automation represented what had taken close to a month to do beforehand. The process flow of events and automation programs can be seen in Figure 30.

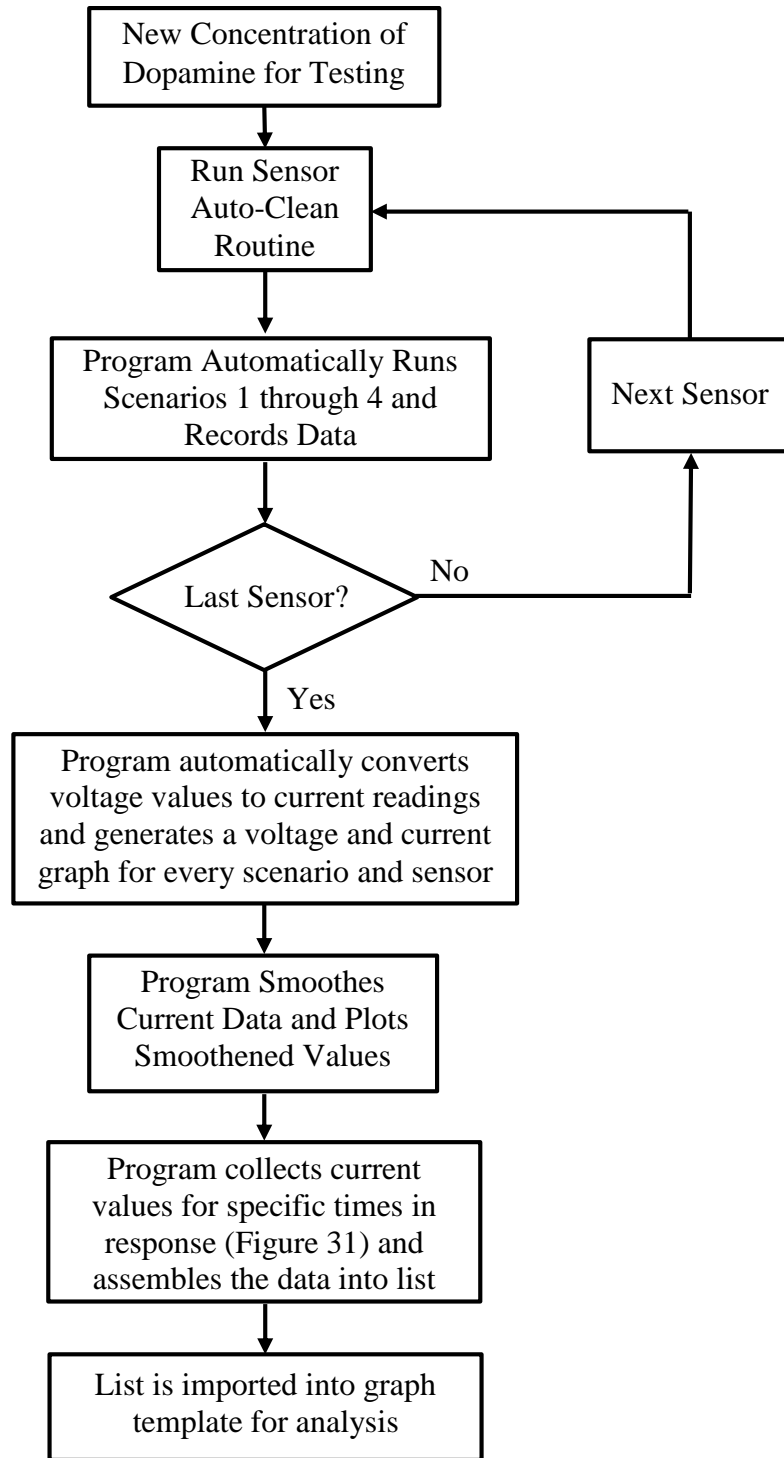


Figure 30: The process flow for data acquisition and processing programs. Automation greatly improved the testing and analysis of sensors.

The result of smoothing the current data can be seen in Figure 31 . The black circles represent where the current data values were sampled. As can be seen, each cycle had 4 places where the data was measured. These were where the response attenuated and leveled off in different portions of the cycle. Table 2 details the polarity of the applied waveforms on the outer and inner electrodes.

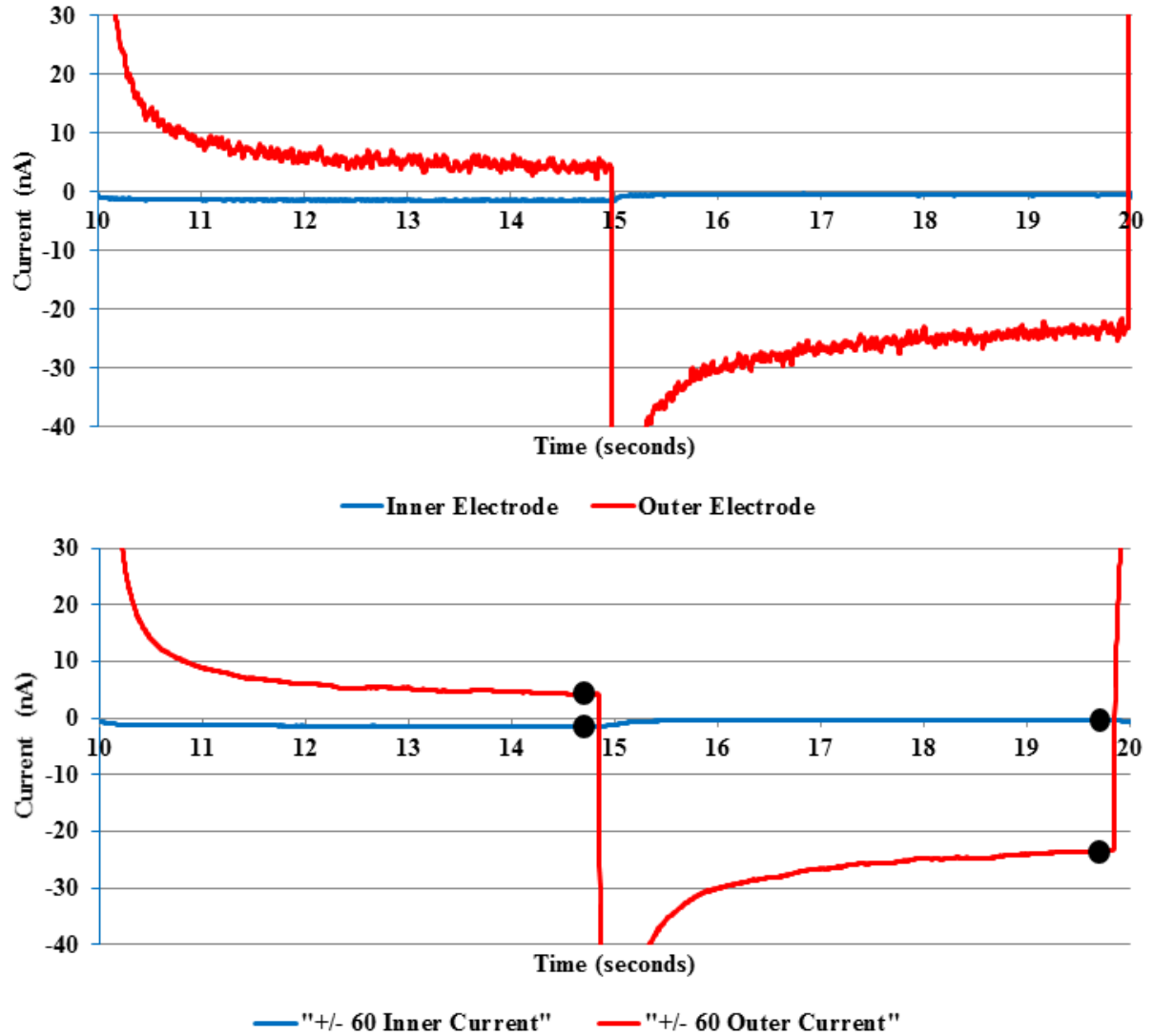


Figure 31: The graphs show the effect of smoothing the data and where the samples of current response values (black circles) were taken to be used for analysis. The top graph shows the inner and outer electrode current response pre-smoothing and with some noise. At a larger magnification, the noise on the smaller electrode is visible as well. The bottom graph shows the same data with a plus and minus 60 point moving average for both inner and outer electrode currents. The current values for sensor response and analysis come from the approximate location of the black circles and represent the four values used for each testing scenario (Table 1).

The following table, Table 2, documents what the electrode potentials are when the four current values are collected for each testing scenario.

Table 2: Recorded Data Points for each Applied Waveform

Scenario 1: Outer Electrode: Square Wave -0.4V to +0.7V, 10 second cycle Inner Electrode: Constant -0.4V			
Description	Measuring	Outer Electrode Potential	Inner Electrode Potential
Scenario 1a	Outer Electrode Current	+0.7V	-0.4V
Scenario 1b	Inner Electrode Current	+0.7V	-0.4V
Scenario 1c	Outer Electrode Current	-0.4V	-0.4V
Scenario 1d	Inner Electrode Current	-0.4V	-0.4V
Scenario 2: Outer Electrode: Square Wave -0.4V to +0.7V, 10 second cycle Inner Electrode: Constant +0.7V			
Description	Measuring	Outer Electrode Potential	Inner Electrode Potential
Scenario 2a	Outer Electrode Current	+0.7V	+0.7V
Scenario 2b	Inner Electrode Current	+0.7V	+0.7V
Scenario 2c	Outer Electrode Current	-0.4V	+0.7V
Scenario 2d	Inner Electrode Current	-0.4V	+0.7V
Scenario 3: Outer Electrode: Constant 0V Inner Electrode: Square Wave -0.4V to +0.7V, 10 second cycle			
Description	Measuring	Outer Electrode Potential	Inner Electrode Potential
Scenario 3a	Outer Electrode Current	0V	+0.7V
Scenario 3b	Inner Electrode Current	0V	+0.7V
Scenario 3c	Outer Electrode Current	0V	-0.4V
Scenario 3d	Inner Electrode Current	0V	-0.4V
Scenario 4: Outer Electrode: Square Wave -0.4V to +0.7V, 10 second cycle Inner Electrode: Constant 0V			
Description	Measuring	Outer Electrode Potential	Inner Electrode Potential
Scenario 4a	Outer Electrode Current	+0.7V	0V
Scenario 4b	Inner Electrode Current	+0.7V	0V
Scenario 4c	Outer Electrode Current	-0.4V	0V
Scenario 4d	Inner Electrode Current	-0.4V	0V

As mentioned earlier, the data points for the testing scenarios were all taken in the second cycle after the applied waveforms were started. This was primarily done because it took at least one cycle for the sensor to equilibrate. There was, however, a second reason to be consistent in when the measurement took place. This was because there was a gradual shift in the response of the sensors over time as seen in Figure 32.

The shifting can possibly come from three mechanisms. It can be the pH of the local electrode environment changing from the hydrogen release of the dopamine oxidation as indicated by Figure 12 [98][99]. The second mechanism could be gradual adsorption of species on the sensor [100]. Third could be fouling of with time. A fourth option for the shifting is that it could be a combination of these effects. Based upon the experimental data from this work and comparisons to other work, the putative causes of shifting are shown by dashed lines in Figure 32.

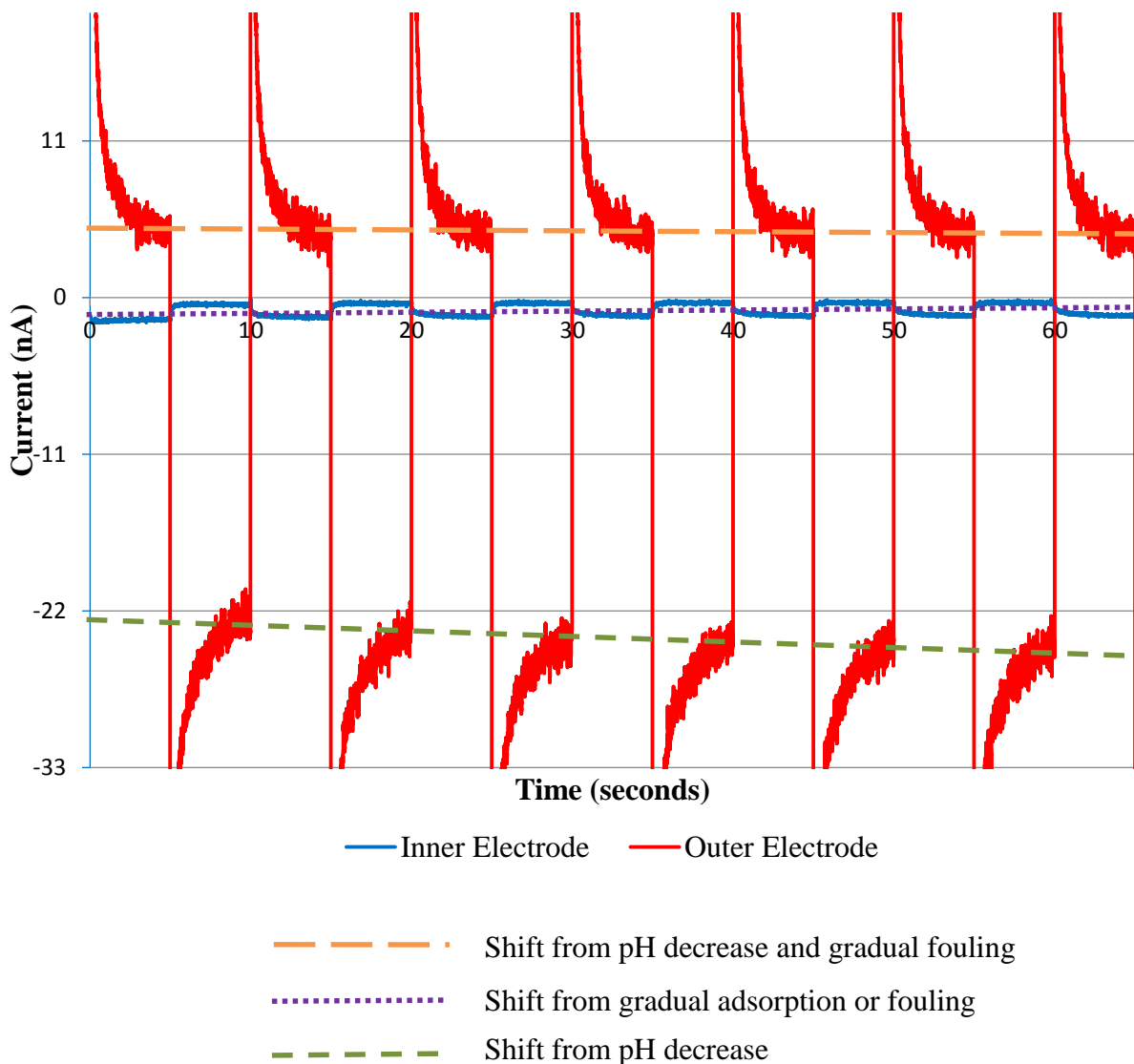


Figure 32: Shifting in sensor response over time. Both electrode responses can be seen and their trending shifts can be seen by the dashed lines. Here the outer electrode was a square wave from -0.4 V to 0.7 V with the inner electrode an inner constant of -0.4V in a 20 μ M dopamine solution. Similar shifting was seen with other testing scenarios. The shifting can possibly come from different effects. It could be the pH of the local environment changing from the hydrogen release or absorption at the electrode surface (Figure 12). The second mechanism could be adsorption. Third could be gradual fouling of the sensor with time. The shifting could also be a combination of these effects. Adsorption of to the surface maybe also be spurred by the intrinsic cationic and zwitterionic forms dopamine has in solution as shown in Figure 45.

These collected nanoamp values would then be automatically assembled into a data table spreadsheet with references to the originating data file. Within this data was also the background current that is present from the motion of ions within PBS. Identical tests (1, 2, 3, and 4), were done on the sensors with PBS alone and the current values from these tests were recorded and subtracted from the values obtained of PBS and dopamine together. With the background current removed, the offset was removed in all cases for the platinum sensors. For the carbon PPF sensors the background current subtraction was not always possible and a partial offset remained due to unidentified reasons.

In post-experiment analysis, it was observed that it was only the lower concentrations where the background subtraction did not work and that as the series of four scenarios were tested, there was an increasing likelihood background subtraction would be applicable to the carbon PPF sensors as the number of sequential tests increased. Perhaps the smaller sample size of carbon PPF sensors vs platinum sensors, the electrode gap differences in the carbon PPF sensors, the topographical height difference between sensor types, metal vs carbon interaction differences with dopamine and the different rate of fouling of platinum sensors compared to carbon PPF sensors, may all play a role in why the background subtraction worked differently for carbon PPF sensors than in platinum sensors. These could all be investigations of future work.

Chapter 3 Results and Discussion for the Electrochemical Sensing of Dopamine

3.1 Platinum Sensor Electrode Oxidative and Reduction Results

The platinum sensors were tested at several concentrations of dopamine with the four testing scenarios described in Table 1. The measured current for both the outer and inner electrodes was gathered during the application of the square wave. The background PBS currents were subtracted and the resulting graphs were created as detailed in the previous section.

Testing Scenario 1 was the application of a square wave from -0.4 V to +0.7 V with 10 second cycle time, applied to the outer electrode and a constant -0.4 V applied to the inner electrode. To improve clarity of the information collected during this test, it was sub divided into four states, Scenarios 1a-d. The potential of the electrodes for these states are summarized in Table 3.

Table 3: Platinum Scenario 1, Outer Electrode: Square Wave -0.4V to+0.7V, 10 sec cycle, Inner Electrode: Constant -0.4V				
Description	Measuring	Outer Electrode Potential	Inner Electrode Potential	Response Results
Scenario 1a	Outer Electrode Current	+0.7V	-0.4V	Linear, oxidative, concentration dependent curve (See Figure 33)
Scenario 1b	Inner Electrode Current	+0.7V	-0.4V	Non-informative (not shown)
Scenario 1c	Outer Electrode Current	-0.4V	-0.4V	Non-informative (not shown)
Scenario 1d	Inner Electrode Current	-0.4V	-0.4V	Non-informative (not shown)

Scenarios 1b, 1c and 1d had response results that were either entirely constant or mostly constant. Collectively they did not indicate a clear dependency on the dopamine concentration. This result was expected for Scenarios 1c and 1d because both electrodes were at -0.4V, the potential required to reduce dopamine-o-quinone to dopamine. However, for 1c and 1d there was not an electrode at +0.7V driving the production of dopamine-o-quinone for the negative potential electrodes to reduce and detect as a current.

Scenarios 1a and 1b were performed in the same dopamine reservoir as 1c and 1d. Any residual quantity of dopamine-o-quinone present from 1a's and 1b's previous +0.7V electrode activity would have been extremely miniscule and was not measured in this test.

Not seeing a clear response for Scenario 1b was unexpected because in this situation the outer electrode with the positive potential was oxidizing dopamine into dopamine-o-quinone and the inner electrode at the negative potential should have been reducing the just produced dopamine-o-quinone back to dopamine. An adsorption current response was only seen with the outer electrode indicating it was interacting with the solution. Apparently the dopamine-o-quinone did not make it to the inner electrode in any appreciable quantity. This can be explained by considering that the electrodes are planar with the substrate surface. In this configuration, diffusion away from the plane of the outer electrode is also diffusion away from the plane of the inner electrode. To reach the inner electrode, the dopamine-o-quinone molecules would have to random walk in the same plane as the sensor and then, at the right moment, travel with an orthogonal component to have a trajectory that brings it back to the inner electrode. Stochastically speaking this route probably does occur, but it is not in any appreciable volume as seen by the lack of a distinctive reduction current at the electrode.

The most compelling result from this first round of testing in Table 1 was where the outer electrode showed a linear, oxidative response curve as seen in Figure 33.

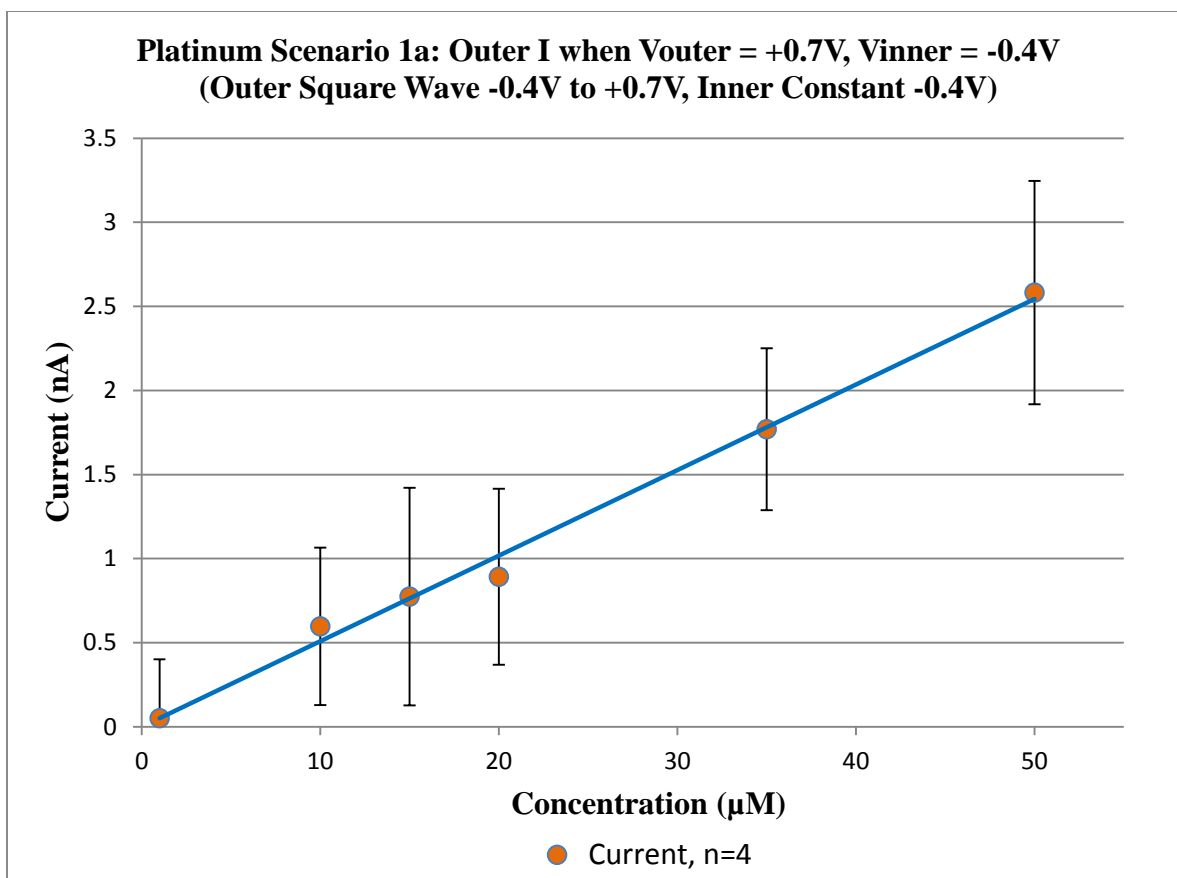


Figure 33: Platinum sensors have a linear, oxidative concentration dependent curve for the outer electrode current in Scenario 1a where the outer electrode was at $+0.7V$ and the inner electrode at $-0.4V$. Error bars are one standard deviation.

Ostensibly the linear response of Figure 33 indicates that the outer electrode was interacting with the bulk solution and oxidizing dopamine into dopamine-o-quinone. The larger the concentration of dopamine, the greater the collected current.

In the next test, Scenario 2, the outer electrode had a square wave cycling between an oxidation potential ($+0.7V$) for dopamine and reducing potential ($-0.4V$) for dopamine-o-quinone's while the inner electrode was at a dopamine oxidation potential of $+0.7V$. With both electrodes at a voltage that would cause dopamine's oxidation, and the outer electrode being approximately twice the surface area of the inner electrode, this scenario was meant to

examine if the outer electrode could screen or reduce the amount of dopamine that could be oxidized by the inner electrode. This would characterize the influence of the outer electrode on the inner electrode for dopamine oxidation. As with Scenario 1, the results were divided into four sub-scenarios depending on the applied potentials.

Table 4 summarizes the findings for Scenario 2.

Table 4: Platinum Scenario 2, Outer Electrode: Square Wave -0.4V to+0.7V, 10 sec cycle, Inner Electrode: Constant +0.7V				
Description	Measuring	Outer Electrode Potential	Inner Electrode Potential	Response Results
Scenario 2a	Outer Electrode Current	+0.7V	+0.7V	Linear, oxidative, concentration dependent curve (See Figure 34)
Scenario 2b	Inner Electrode Current	+0.7V	+0.7V	Linear, oxidative, concentration dependent curve, screening of inner electrode seen (See Figure 35)
Scenario 2c	Outer Electrode Current	-0.4V	+0.7V	Non-linear reduction curve, cycling partially present (See Figure 36)
Scenario 2d	Inner Electrode Current	-0.4V	+0.7V	Linear, oxidative, concentration dependent curve, little effect from outer electrode (See Figure 37)

Three out of four response results in Scenario 2, 2a, 2b and 2d, produced linear, oxidative, concentration dependent curve responses.

Figure 34 shows the response of the platinum sensors for Scenario 2a.

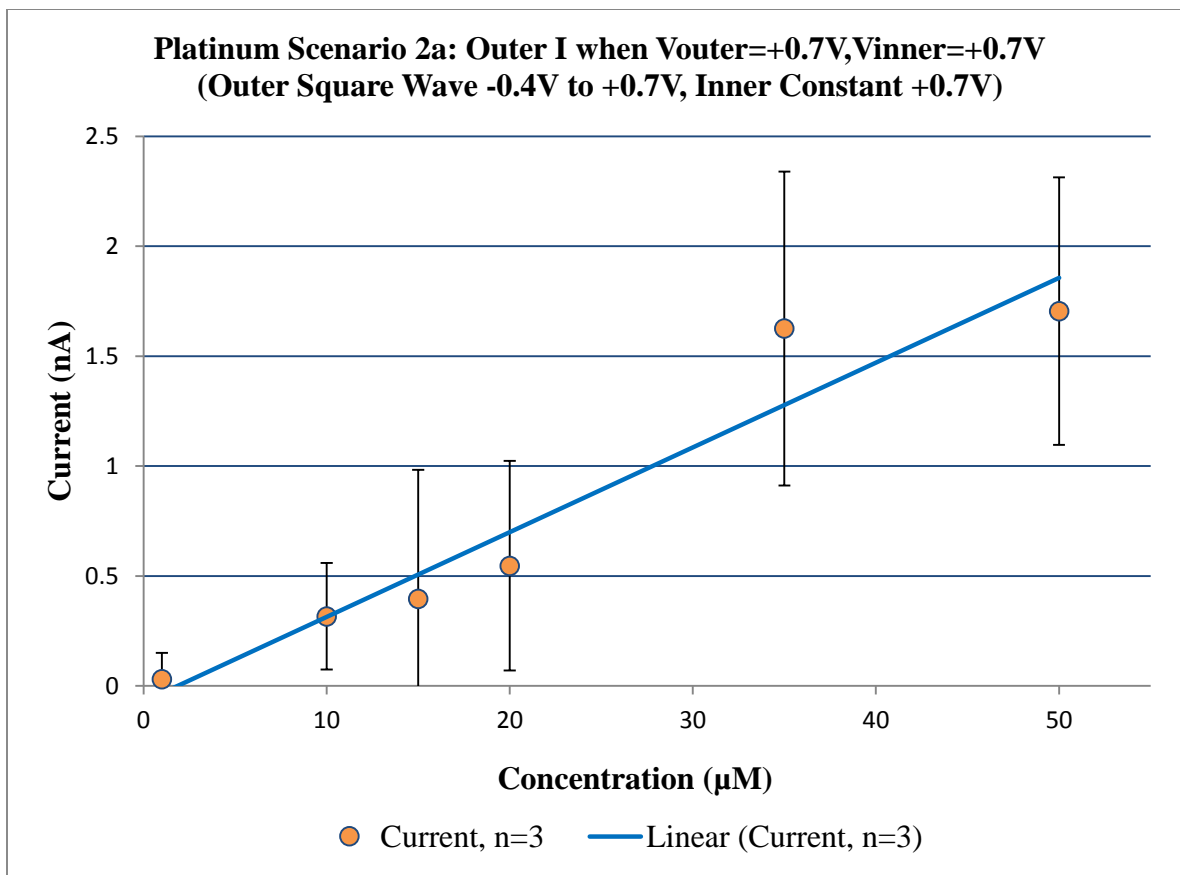


Figure 34: Platinum sensors have a linear, oxidative concentration dependent curve for the outer electrode current in Scenario 2a. Error bars are one standard deviation.

Scenario 2b examined a screening effect of the inner electrode and the linearity of the nanoamp current response for the test can be seen in Figure 35. The influence of the outer electrode can be seen in Figure 40 when by comparing Scenario 2b to Scenario 3b which had the inner electrode at $+0.7V$ and the outer at $0V$.

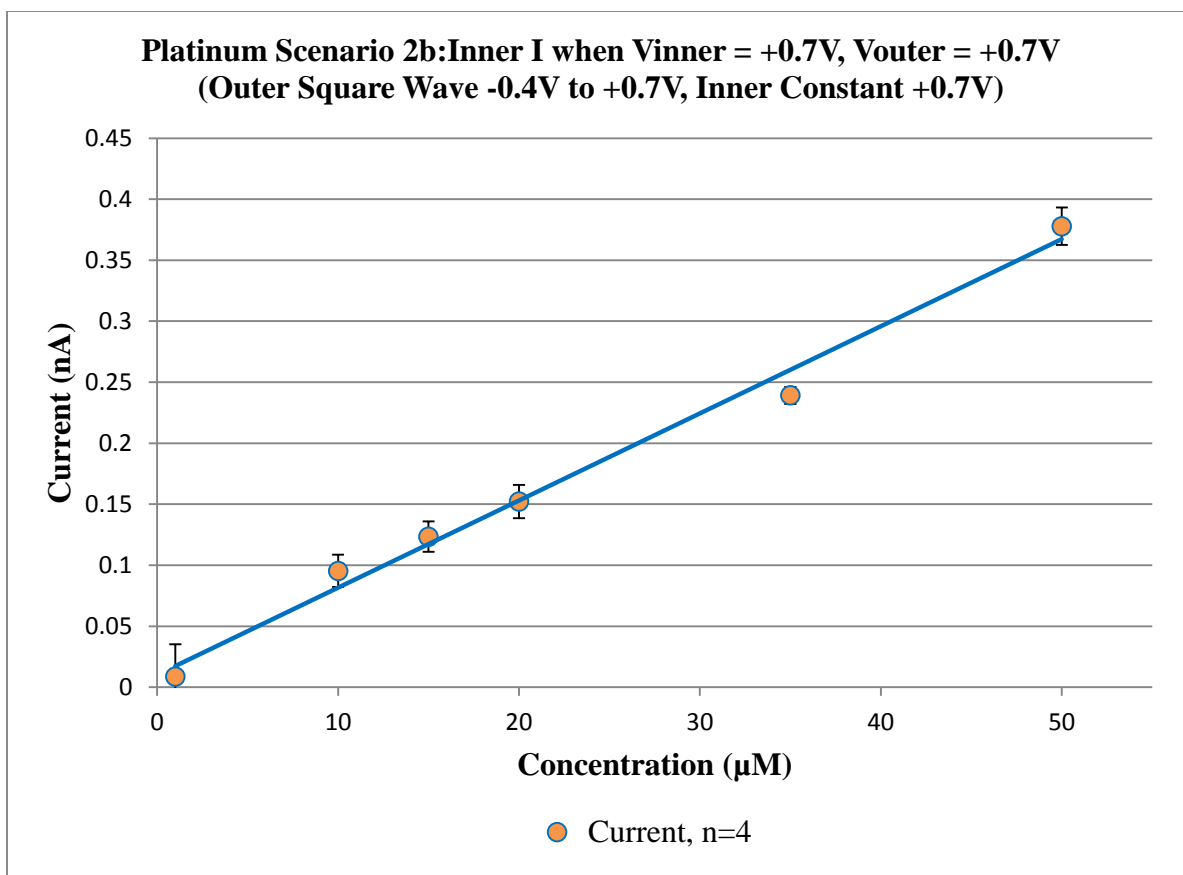


Figure 35: Platinum sensors have a linear, oxidative concentration dependent curve for the inner electrode current in Scenario 2b. Error bars are one standard deviation.

Scenario 2c was reduction current test and was similar to Scenario 1b, but with opposite polarities on the electrodes. However unlike in Scenario 1b, in 2c a reduction current was observed. The response nearly plateaus at 20 μM as seen in Figure 36. Here the current relies on the dopamine-o-quinone being produced at the inner electrode, and then it diffusing to the outer electrode. The diffusion of the dopamine-o-quinone toward the outer electrode causes the outer electrode current to noticeably increase till approximately 20 μM . Afterwards the response is close to constant or slightly increasing. There does not seem to indicate that there is a limit on the maximum amount the inner electrode can produce because in the case where the inner electrode is oxidizing dopamine the response is linear as seen in

Figure 38. Instead this appears to indicate the dopamine-o-quinone produced maybe diffusing more into the bulk solution than toward the outer electrode.

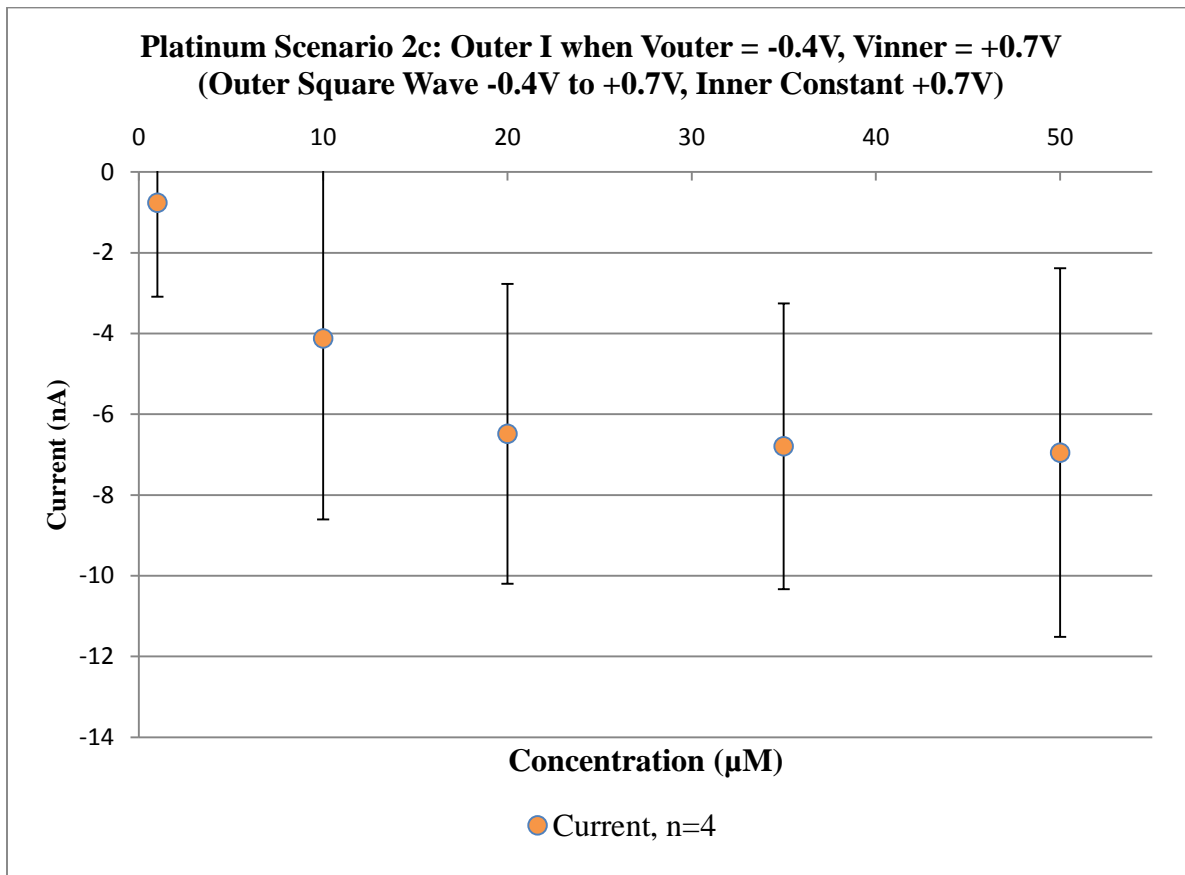


Figure 36: A reduction current was measured in Scenario 2c and it leveled off at approximately 20 μM . This indicates that the inner electrode reached a maximum in the amount of dopamine-o-quinone it could produce. Error bars are one standard deviation.

Scenario 2d examined the oxidation of dopamine at the inner electrode when its potential was set at $+0.7V$ and the outer potential was $-0.4V$. A linear response was seen as seen in Figure 37. There was a slight effect of the outer electrode which is shown in Figure 40 when compared to testing Scenario 3b.

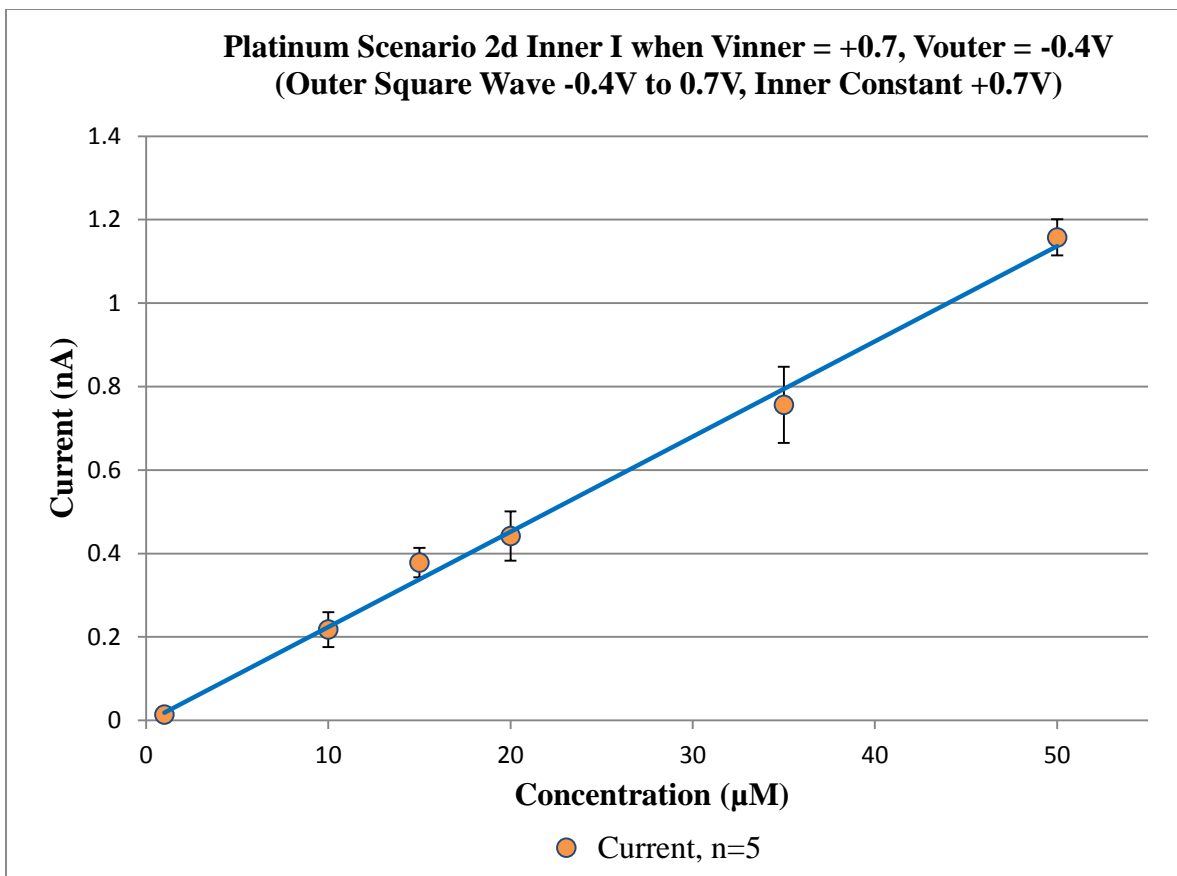


Figure 37: Scenario 2d for the platinum sensors produced a linear, oxidative concentration dependent curve for the inner electrode current. Error bars are one standard deviation.

Scenario 3 changed the conditions by putting the square wave on the inner electrode and holding the outer electrode at a constant 0V potential, to evaluate the interaction between electrodes. Table 5 summarizes the response results of Scenario 3.

Table 5: Platinum Scenario 3, Outer Electrode: Constant 0V Inner Electrode: Square Wave -0.4V to +0.7V, 10 sec cycle				
Description	Measuring	Outer Electrode Potential	Inner Electrode Potential	Response Results
Scenario 3a	Outer Electrode Current	0V	+0.7V	Non-informative (not shown)
Scenario 3b	Inner Electrode Current	0V	+0.7V	Linear, oxidative, concentration dependent curve (See Figure 38)
Scenario 3c	Outer Electrode Current	0V	-0.4V	Non-informative (not shown)
Scenario 3d	Inner Electrode Current	0V	-0.4V	Non-informative (not shown)

Scenario 3b produced a linear, oxidative, concentration dependent curve for the inner electrode as seen in Figure 38. Testing Scenarios 3b, 3c and 3d were initially thought to possibly offer some information on the background current for subtraction from the dopamine and dopamine-o-quinone signal. Research showed that it was better to subtract PBS background currents to produce data isolating the dopamine dependent response.

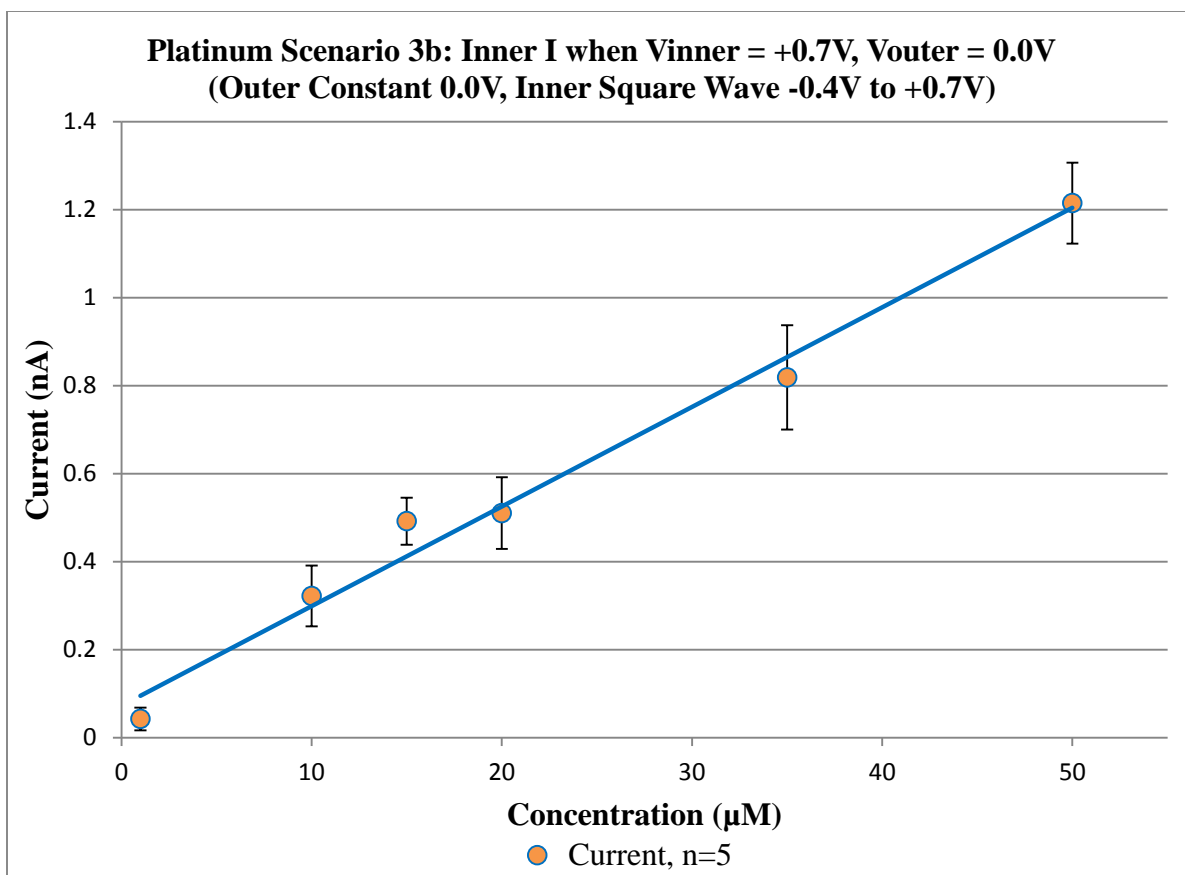


Figure 38: Scenario 3b for the platinum sensors produced a linear, oxidative concentration dependent response curve for the inner electrode current. Error bars are one standard deviation.

Scenario 4's results are shown in Table 6. In this situation the square wave of oxidation and reduction potentials was placed on the outer electrode, while the inner electrode was held at 0V.

Table 6: Platinum Scenario 4, Outer Electrode: Square Wave -0.4V to +0.7V, 10 sec cycle, Inner Electrode: Constant 0V				
Description	Measuring	Outer Electrode Potential	Inner Electrode Potential	Response Results
Scenario 4a	Outer Electrode Current	+0.7V	0V	Linear, oxidative, concentration dependent curve (See Figure 39)
Scenario 4b	Inner Electrode Current	+0.7V	0V	Non-informative (not shown)
Scenario 4c	Outer Electrode Current	-0.4V	0V	Non-informative (not shown)
Scenario 4d	Inner Electrode Current	-0.4V	0V	Non-informative (not shown)

Testing Scenarios 4b, 4c and 4d were initially thought to possibly offer some information on the background current for subtraction from the dopamine and dopamine-o-quinone signal. As with the findings from 3a, 3c and 3d, it was better to subtract PBS background currents to produce a graph isolating the dopamine related response.

Scenario 4a produced a linear, oxidative, concentration dependent curve for the outer electrode as seen in Figure 39.

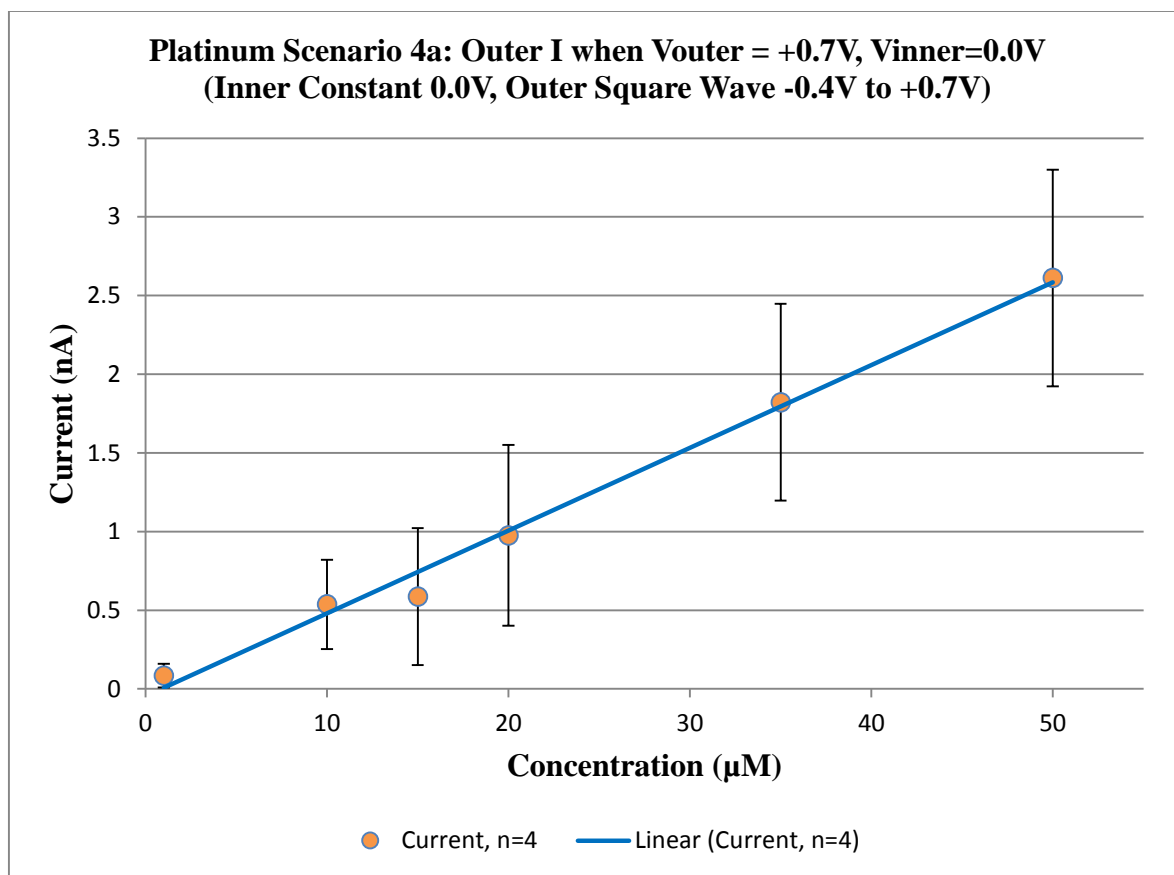


Figure 39: Platinum sensors have a linear, oxidative concentration dependent response curve for the inner electrode current in testing Scenario 4a. Error bars are one standard deviation.

The individual graphs of the electrode currents can be compared to each other to evaluate the electrode amperometric responsivity in their respective scenarios. There are some similarities and differences in the responses.

To make the electrode response comparison more apparent, the oxidative graph slopes ($nA/\mu M$) were measured and plotted together on the same graph in Figure 40. This responsivity graph shows how the oxidative rate on the outer electrode is not affected by the potential of the inner electrode if the inner electrode is at $-0.4V$ (Scenario 1a) or at $0V$ (Scenario 4a). However, if the outer electrode is oxidizing dopamine, it is affected by the inner electrode, if the inner potential is also at an oxidizing potential (Scenario 2a). The

competition between outer and inner electrode to oxidize dopamine reduces the rate of oxidation on the outer electrode from 5.2×10^{-2} nA/ μ M to 3.4×10^{-2} nA/ μ M, a 35% decline.

A similar trend can be seen on the inner electrode oxidative graph slopes. When the inner electrode is oxidizing dopamine with a +0.7V potential, there is slight difference for the inner electrode oxidation rate if the outer electrode is -0.4V or 0V (Scenarios 2d and 3b). However when the inner electrode is at the oxidizing potential and the outer electrode is made to compete with it (Scenario 2b), then there is electrode shielding and competition for dopamine, reducing the oxidation rate at the inner electrode from 2.3×10^{-2} nA/ μ M to 7.5×10^{-3} nA/ μ M, a 67% diminishment. Since the competing electrode in this case is the outer electrode, it is a reasonable result since the oxidation rate is proportional to the area, and the outer electrode has approximately twice the area of the inner electrode.

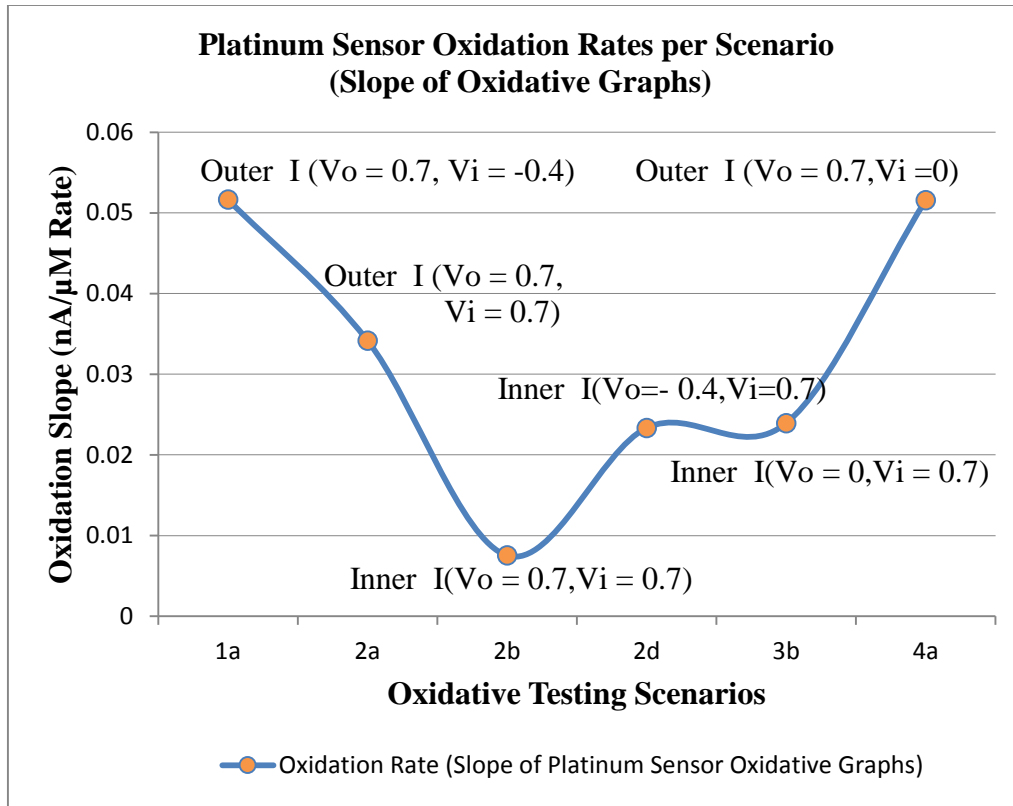


Figure 40: Platinum sensor oxidation rates per testing scenario in nA/μM. The electrode oxidation rate is highest for the outer electrodes when the inner electrode is not set to oxidize dopamine.

3.2 Platinum Electrode Mass Transport

The mass transport flux of the platinum sensors was also examined by using Faraday's Law of Electrolysis. This relation is written as:

$$Q = I t \tag{3}$$

Where Q is the charge in coulombs, I is current (coulombs/second) and t is time (seconds). This expression can be expanded to be:

$$Q = It = nNF \quad (4)$$

Where n is the number of electrons per reaction, N is the amount of moles, and F is Faraday's constant, the electric charge per mole of electrons (96,485 Coulombs/mole).

Rearranging terms in (4), the following relation can be attained:

$$\frac{N}{t} = \frac{I}{nF} \quad (5)$$

The units of (5) are moles/second. Dividing (5) by the area of an electrode will give the moles/second per unit area, or in other words, the mass transport per unit area, which is the mass transport flux. In this case the units used were nanomole per second per square micrometer, $(\text{nM}/\text{t})/\mu\text{m}^2$. The results for the different Scenario tests can be seen in Figure 41.

Figure 41 shows the inner electrode had maximum flux values across all concentrations in Scenarios 3b and 2d when there wasn't competition with the outer electrode for dopamine oxidation. In 3b and 2d the inner electrode had very similar rates of mass transport across the different concentrations.

The outer electrode had the following highest mass transport flux when the outer electrode was not competing with the inner electrode for dopamine in Scenarios 1a and 4a. In these two cases, the outer electrode had almost identical values for mass transport flux.

The higher flux per unit area for the the inner electrode (Scenarios 3b, 2d) is probably due to the smaller surface area of the inner electrode compared to the outer electrode.

The lowest mass transport flux area was in Scenarios 2a and 2b where the outer and inner electrodes competed for dopamine, effectively shielding one another from the dopamine reservoir. The competition resulted in less oxidation occurring at both electrodes.

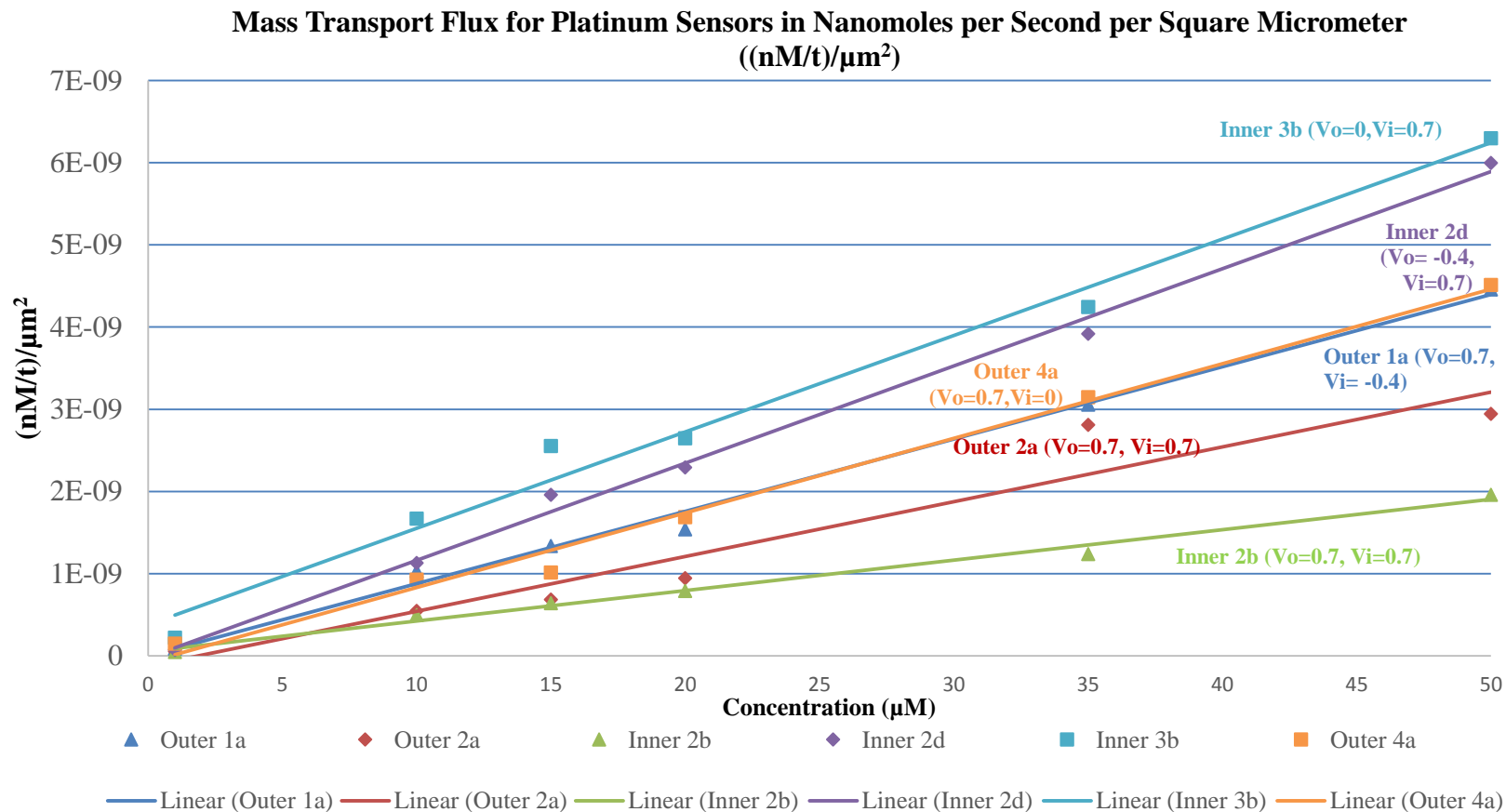


Figure 41: Mass Transport Flux for Platinum Sensors in Nanomoles per Second per Square Micrometer ((nM/t)/ μm^2) with linear regression lines. “Outer” and “inner” refer to the outer and inner electrodes respectively.

Another way to examine the mass transport flux is to look at the rates, or slopes, of flux from Figure 41 above. These flux rates were plotted in Figure 42. Not surprisingly, the relative positions of the rates per graph out in the same relative position as one would expect from seeing Figure 41. This rate graph information provides a way to compare platinum sensor results with the carbon PPF results. Unlike the platinum sensor readings, the carbon PPF sensors have an offset that could not be removed. The offset would give the carbon PPF sensors higher readings in a direct comparison with platinum. By examining the rates of change, the offset can be ignored and the sensors can be quantitatively compared in terms of responsiveness. The comparison between platinum and carbon PPF sensor mass transport flux rate is made in Table 13.

As for comparing the mass transport flux results for the platinum sensor different modes of operation, Scenarios 2d and 3b were nearly identical. This was when the inner electrode was not competing for dopamine with the outer electrode. As soon as there was competition, as in Scenario 2b, the mass transport rate fell from approximately 1.2×10^{-10} $((\text{nM}/\text{t})/\mu\text{m}^2)/\mu\text{M}$ to 3.7×10^{-11} $((\text{nM}/\text{t})/\mu\text{m}^2)/\mu\text{M}$, a 69% decline.

For the outer electrodes, the mass transport rates were also similar when only the outer electrode was actively oxidizing dopamine as in Scenario 1a and 4a. When the inner electrode also was oxidizing dopamine, the mass transport fell from approximately 8.9×10^{-11} $((\text{nM}/\text{t})/\mu\text{m}^2)/\mu\text{M}$ to 6.6×10^{-11} $((\text{nM}/\text{t})/\mu\text{m}^2)/\mu\text{M}$, a -26% change as seen with Scenario 2a.

Shielding, or competition, between electrodes is apparently greater when the inner electrode is being affected by the outer electrode. This is most likely because the outer electrode is bigger with approximately double the surface area of the smaller, inner electrode and flanks the smaller electrode on 2 sides.

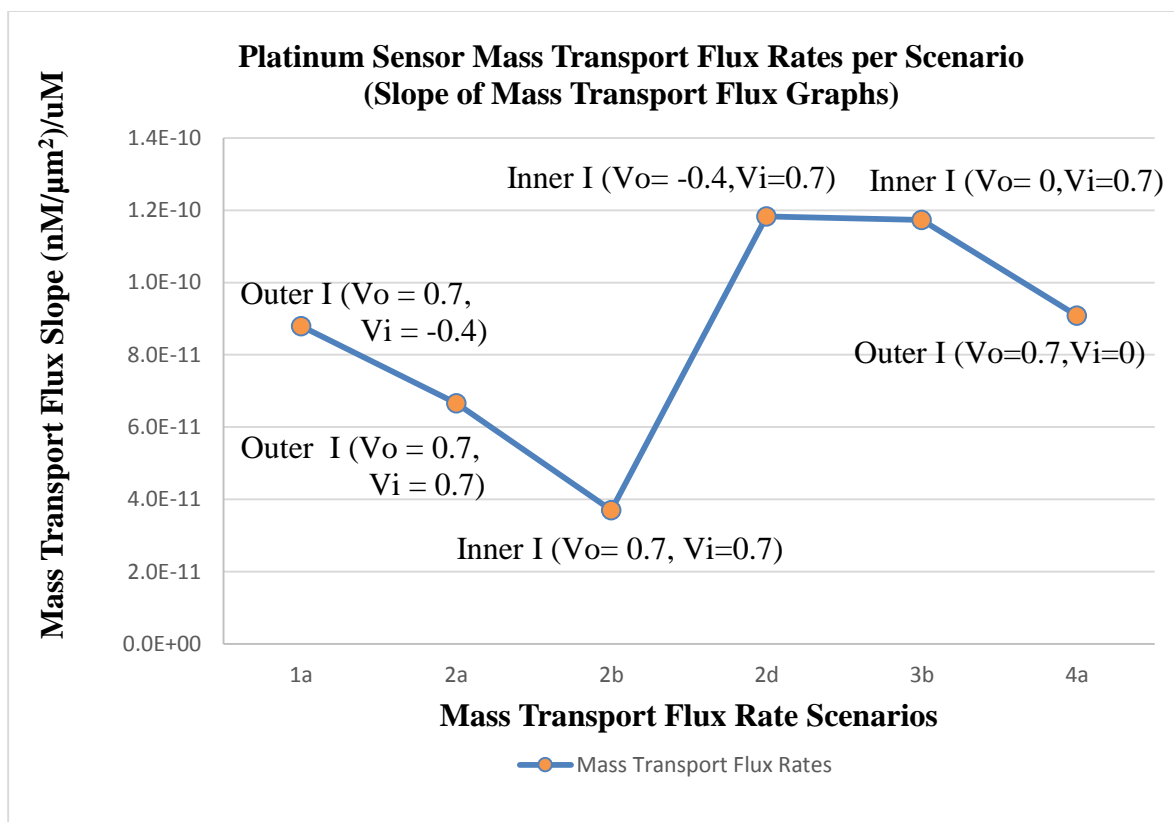


Figure 42: Platinum sensor mass transport flux rates per scenario. The mass transport flux rate was greatest for the inner electrode in Scenarios 2d and 3b where there wasn't competition between electrodes for dopamine oxidation.

3.3 Platinum Sensor Electrode Current Flux

The current flux per unit area of the platinum sensors was also examined by taking the measured value of current and dividing per electrode area. The results for this can be seen in Figure 43.

The inner electrode has the highest electrical current flux in Scenario 3b and 2d in Figure 43. This maximum occurred when the inner electrode didn't have competition with the outer electrode for dopamine oxidation.

Two scenarios, 4a and 1a, for the outer electrode had the next largest electric current flux. These were maximum values for the outer electrode and occurred when the outer electrode was not competing with the inner electrode for dopamine, with the inner electrode either at 0V or -0.4V.

The lowest flux per unit area was for an outer and inner electrode in Scenarios 2a and 2b, respectively. In both cases the electrode was competing with the second electrode for dopamine, resulting in a smaller electrical flux at both electrodes.

The higher current flux per unit area for the inner electrode in Figure 43, is most likely due to the difference in surface areas of the electrodes.

Current Flux in Nanoamps for Platinum Sensors per square Micrometer ($\text{nA}/\mu\text{m}^2$)

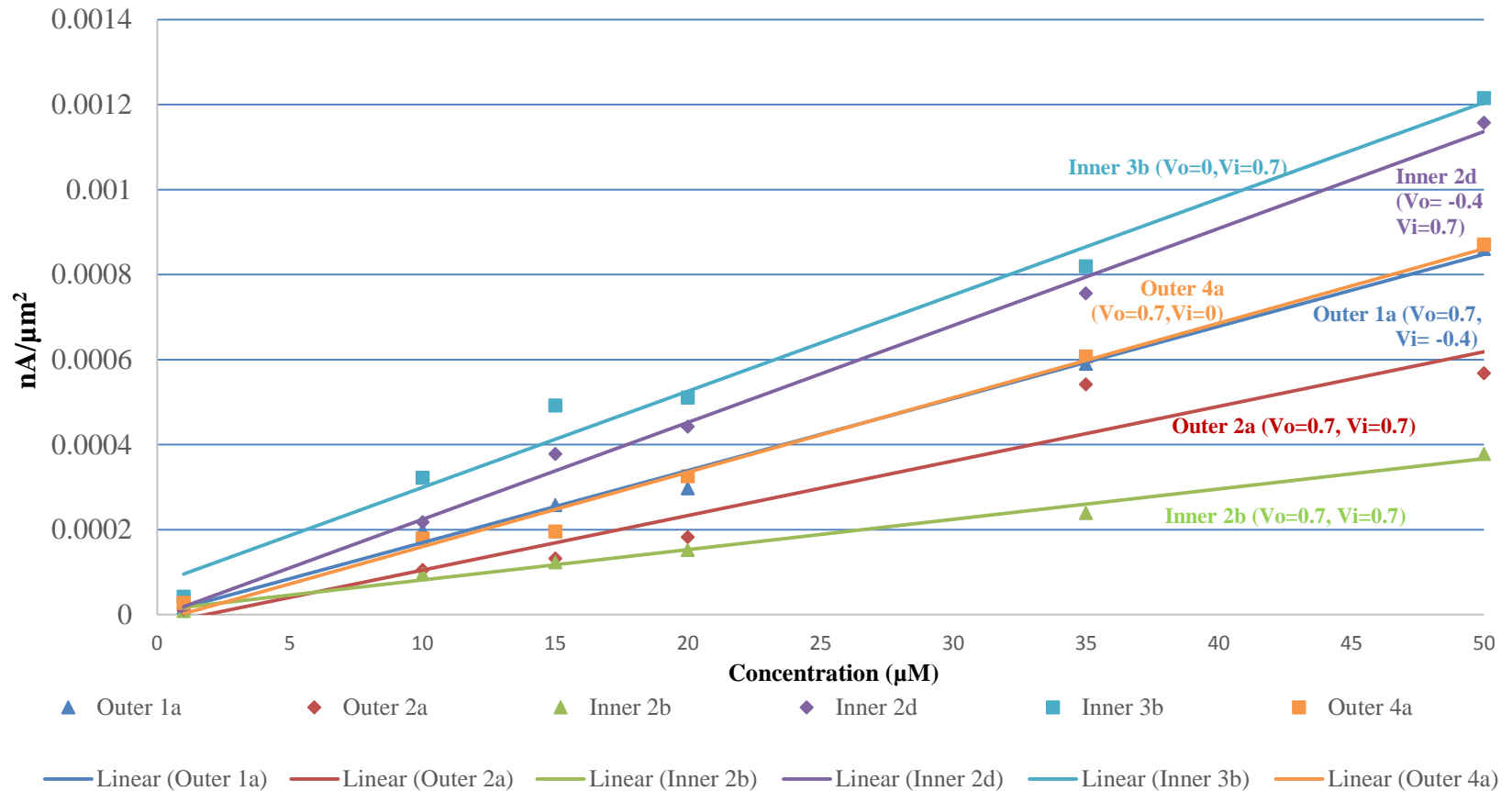


Figure 43: Platinum Sensors Electrical Current Flux per Unit Area ($\text{nA}/\mu\text{m}^2$)/ μM with linear regression lines. “Outer” and “inner” refer to the outer and inner electrodes respectively.

The current flux rates of Figure 43 were plotted in Figure 44. Scenarios 2d and 3b were a pair of data points with similar values. Scenarios 4a and 1a were also similar to each other. These four data points were when the second electrodes were not shielding the recording electrode from dopamine.

When there was competition, as in Scenario 2b, the electric current flux rate of the inner electrode fell from approximately 2.3×10^{-5} nA/ μm^2 (in 2d and 3b) to 7.1×10^{-6} nA/ μm^2 . This represented a 69% attenuation.

For the outer electrode, non-competition was for Scenarios 1a and 4a, while competition occurred in Scenario 2a. For these cases, the electric current flux rate of the outer electrode went from approximately 1.7×10^{-5} nA/ μm^2 to the lower value of 1.3×10^{-5} nA/ μm^2 , respectively. This signified a 26% reduction in the electrical current flux rate.

A comparison of electrical flux rate between platinum and carbon PPF sensors can be seen in Table 14.

As for comparing the mass transport flux results for the platinum sensor, Scenarios 2d and 3b were nearly identical. These scenarios were when the inner electrode was not competing for dopamine with the outer electrode. As soon as there was competition, as in Scenario 2b, the mass transport rate fell from approximately 1.2×10^{-10} (nA/ μm^2)/ μM to 3.7×10^{-11} (nA/ μm^2)/ μM , a 68.5% decline.

It appears that the relative size difference of the electrodes can be responsible for the electric current flux rate differences as well as the shielding that occurs. The smaller size of the inner electrode means it has a higher flux per unit area.

Shielding, or competition, between electrodes is apparently greater when the inner electrode is being affected by the outer electrode, because the outer is bigger, has double the surface area and flanks the smaller electrode on 2 sides.

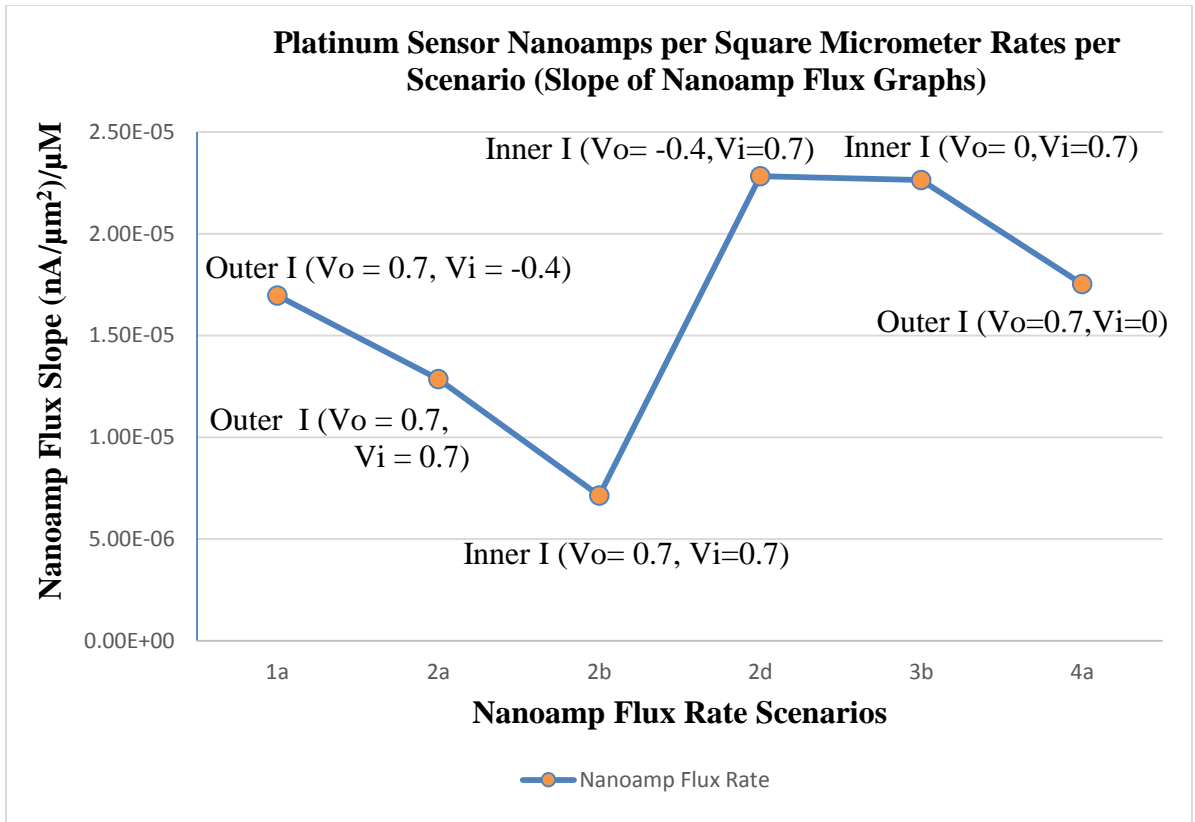


Figure 44: Platinum Sensor Nanoamps Flux Rates per testing Scenario.

3.4 Platinum Sensor Electrode Cottrell Equation Relation

The correlation to the Cottrell equation for the platinum type sensors was examined. The Cottrell Equation is typically applied to measuring current over time for chronoamperometry studies. The Cottrell equation is given in (6).

$$i = \frac{nFAD^{1/2}C_o}{(\pi t)^{1/2}} \quad (6)$$

Here n is the number of electrons transferred per molecule. For dopamine n is 2 electrons. Surface area is represented by A , measured in cm^2 . F is Faraday's constant, the

electric charge per mole of electrons, given as 96,485 Coulombs/mole. The variable D is the diffusion coefficient, which for dopamine is 5.4×10^{-6} cm²/sec [101]. C_o is the concentration of the analyte measured in units of moles/cm³. Time is represented by t in seconds.

In this research, the platinum sensors do not produce a current that can be predicted from the Cottrell equation as given in (6). Attempts were made to try to match the data to variations of the Cottrell equation modified to correct for the diffusion geometry of electrodes [20][24][103]-[105], but none of the options appeared as strong, pertinent candidates. It was decided to use the Cottrell equation as shown in (6), which is most often applied for potential step methods [3][20][24] as a basis of comparison and analysis.

The collected currents from the platinum sensor can be approximated by applying a correction coefficient to the Cottrell equation. For Scenarios 1a, 2a, 2b and 2d, the multiplying coefficient can be seen in Table 7. The dimensionless coefficient, S , arises from dividing the measured current value by the predicted Cottrell value as seen in (7) for each dopamine concentration tested.

$$S = \frac{I \text{ (measured)}}{I \text{ (predicted Cottrel current)}} \quad (7)$$

The multiplication factors for Scenarios 1a, 2a, 2b and 2d were close enough across dopamine concentrations to be averaged into a constant multiplying coefficient. Those averaged multiplying factors can be seen in Table 7. Since the relationship was not perfectly linear, and there was some averaging done, the standard deviation of the coefficients was also included in Table 7. When the standard deviation of the coefficient multiplier is expressed as a percentage of the multiplying coefficient, it is a small range of 6.3% to 10.9%. In other words, the predicted value from the coefficient multiplication will give a current value that should be within 6.27% to 10.85% of the actual value.

Table 7: Cottrell Equation Multiplying Coefficient for Platinum Sensors in Scenarios 1a, 2a, 2b, 2d-2d					
Scenario	Description	Current Being Measured & Electrode Potentials	Cottrell Equation Multiplying Coefficient	Coefficient Standard Deviation (across 5 to 6 dopamine concentrations)	Standard deviation / Coefficient multiplier
1a	Outer oxidizing potential, inner reducing potential	Outer I ($V_o = 0.7V$, $V_i = -0.4V$)	14.71	1.27	8.63%
2a	Outer electrode competing with inner electrode	Outer I ($V_o = 0.7V$, $V_i = 0.7V$)	9.66	0.911	9.43%
2b	Inner electrode competing with outer electrode	Inner I ($V_o = 0.7V$, $V_i = 0.7V$)	6.92	0.752	10.85%
2d	Inner oxidizing potential, outer reducing potential	Inner I ($V_o = -0.4V$, $V_i = 0.7V$)	18.2	1.143	6.27%

The measured current was compared to the predicted current as seen in (7) for testing Scenarios 3b and 4a as well, however, the current characterization was different in these situations. The measured current in these cases are not described by multiplying the Cottrell equation with a constant coefficient across all the tested concentrations like in Table 7 above. For 3b and 4a the current measured was larger than the predicted Cottrell equation, but was not larger due to a constant coefficient. Instead the coefficient was greater at lower concentrations and became smaller at higher concentrations in a smooth transition. They can be seen in Figure 47 and Figure 48. Possible mechanisms at work will be discussed below.

The resulting shape of the curve for the varying multiplying coefficient, S , resembled an inverse of a square root function. For this reason the data was fit to a function

proportional to the inverse square root of the concentration, C , multiplied by a constant, a , and added to a constant displacement value, b , as shown in (8).

$$S = \frac{a}{\sqrt{C}} + b \quad (8)$$

Since there appeared a relationship to the inverse square root of the concentration, it would be appropriate to look for a characteristic or principle of microelectrode sensors that can modulate a response based on the inverse square root of the concentration. Fortunately such a feature exists and more importantly, is relevant to changing concentrations at electrode surfaces. It is the Debye length, λ_D , and is given in (9) from [54].

$$\lambda_D = \frac{\sqrt{\epsilon_0 \epsilon_b k_B T}}{\sqrt{2e^2 I}} \quad (9)$$

In (9), ϵ_0 is the permittivity free space, ϵ_b is the dielectric constant of the medium, e is the elementary charge (charge of a single electron), k_b is Boltzmann's constant, T is temperature in Kelvin, and I is related to the concentration since it is ionic strength of the fluid. I is defined in (10).

$$I = \frac{1}{2} \sum_i z_i^2 c_i \quad (10)$$

For (10), the variables in the summation are the valence of the ion, z_i , and the concentration of ion i , c_i .

A simplified expression of (10) is given for water at 25 °C in (11) where the Debye length in water can be estimated [54].

$$\lambda_D = \frac{0.30}{z\sqrt{C(M)}} \text{ nm} \quad (11)$$

In this approximation, z is the charge of a symmetrical electrolyte, with equal positive and negative charges for its constituent disassociated species. The concentration, C , is in units of moles.

Whether using the formal definition of (9) or the approximation of (11), the significant concept is that the Debye distance is proportional to the inverse of the square root of the concentration. With the steady-state nanoamp current being modulated by this Debye

or Debye-like influence, it seems to indicate that the electrode is interacting not just with dopamine in contact with it, but the electrode is also interacting with additional dopamine within a distance of the electrode. In other words, it is not a two-dimensional interaction along the electrode surface, but a three dimensional interaction with a volume of fluid in proximity to the electrode surface where the dopamine is being oxidized. The volume expands and contracts with the modulation of the Debye or Debye-like length. What the actual volume dimensions of this influence and subsequent volume will have to be evaluated in future work.

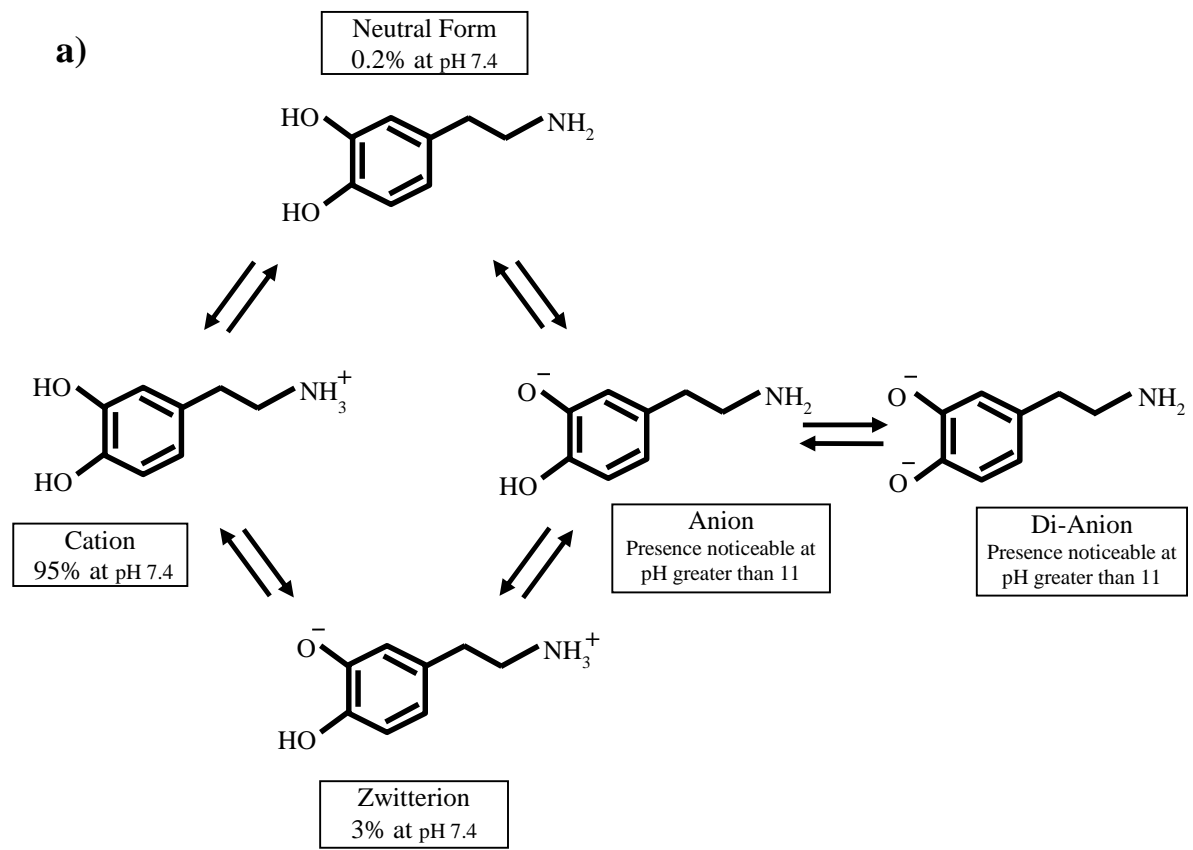
A further interpretation of the data is that when the dopamine concentration is less, the Debye length is greater because there is less screening of the electrode's influence into the solution. With a greater length, there is a correspondingly greater volume of dopamine being interacted with, which produces a higher current and a larger multiplier for the Cottrell equation. The opposite effect is seen when the dopamine concentration increases. As this the concentration increase occurs, the electrical current multiplier of the predicted Cottrell equation becomes smaller. This would be due to the smaller Debye length arising from more charged analyte in solution, increasingly screening the electrode's influence.

As the equations (9) and (11) indicate, the charges in the solution impact the Debye length. Experimentally such Debye length changes based upon concentration have been observed [43]. In the context of the work in this paper, the PBS solution used had dissolved ions, but for all tests the PBS was consistent. Therefore its influence was a constant and any variation seen in the current or Cottrell equation coefficient couldn't be attributed to it. The only part that was changed from a round of testing to the next was the concentration of dopamine. This links the noticed changes to the variation in dopamine concentration.

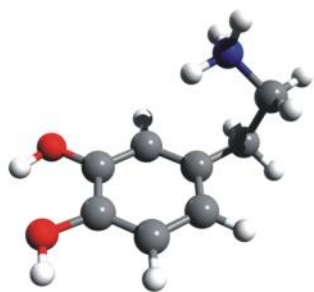
If dopamine were a neutral molecule in solution, the proportionality to the inverse square root of the concentration results would have been confounding. However, at physiological pH 7.4 of this work, dopamine mostly exists as a positively charged cation due to the protonation of its amine group [100][106][107][119] [121]. This protonation is significant because increasing the concentration of dopamine in the PBS increased the charge

of the bulk solution. According to (9) and (11), the Debye length should be reduced as more charge is added. From the decrease in the multiplier of the Cottrell equation as more dopamine is added, this is what appears to be occurring in accordance to the equations. The positive charge on dopamine's amine group at pH 7.4 can be seen in Figure 45 along with the other forms of dopamine.

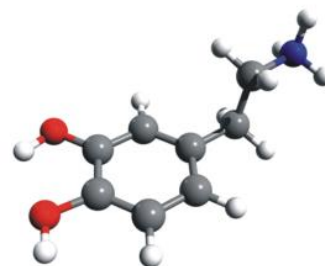
Figure 45: a) The acid-base equilibria of dopamine leads to several forms for the molecule depending on pH [106][107]. The work represented in this paper was done at pH 7.4 where the forms are present in different quantities. Having a zwitterionic and cationic form at the same time is intriguing because the dual charges may contribute to the change in signal response in Figure 32 due to fouling, especially on the negatively biased electrode. There are 5 conformational states that the dopamine cation can possess [107]. Experiments and calculations show the molecular population has almost equally numbers of trans and folded gauche conformations as defined in References [119] & [121] for a neutral aqueous pH of 7. Calculations for isolated protonated dopamine and isolated neutral dopamine at pH 7 have a gauche conformation tendency [119]. b) The most stable trans and gauche structure variants [119]. Figure 45b adapted from Ref [119]- Reproduced by permission of the PCCP (Physical Chemistry Chemical Physics) Owner Societies.



b)



dopamineH⁺ gauche



dopamineH⁺ trans

As the current is being modulated by a Debye or Debye-like influence, and the molecules in that volume are thought to be exchanging electrons with the electrode, the electrons must have a way of reaching them. A mechanism which is known to operate at the Debye length-scales of nanometers and be involved with current, is electron tunneling. Electron tunneling from electrode to electrode through a nanometer scaled gap has been experimentally studied [111][112]. Electron tunneling works by applying a potential between the nanometer-scale-gap-separated electrodes, causing electrons to flow from the more negatively biased electrode, across the gap barrier, toward the more positively biased electrode [111]. The detected current is referred to as the ‘tunneling current’ and it changes exponentially as a function of the gap width [111]. These electrode-solution-electrode kinds of arrangements physically differ from this paper’s work, but conceptually the same elements are present. In both systems there is a flow of electrons over small distances. Both systems also have a potential drop across tiny lengths.

In the electrode to solution situations that potential drop has been be gauged up to approximately 10^8 to 10^9 V/m [113]. However, this probably depends on the experimental parameters. Just as a comparison, the dielectric breakdown of dry air at sea level between parallel electrodes, to produce a spark, is 3×10^6 V/m, while airborne measurements have shown thunderstorm electric fields measuring between 5×10^4 to 8×10^5 V/m [114]. Clearly the electrical field gradient at an electrode’s surface is impressive when juxtaposed with these better known, more familiar situations.

Electron transfer via tunneling has been described as being exponentially distance dependent following an equation of the type given in (12), where β is a tunneling decay constant for aqueous fluids with units of $1/\text{\AA}$ [115][116].

$$e^{-\beta x} \tag{12}$$

The electron transfer may then occur into a zone some length away from the outer Helmholtz plane via tunneling [113][116]. This would be consistent with the proposed method of action mentioned in this paper.

The conditions for this work may have been favorable to see these results because of

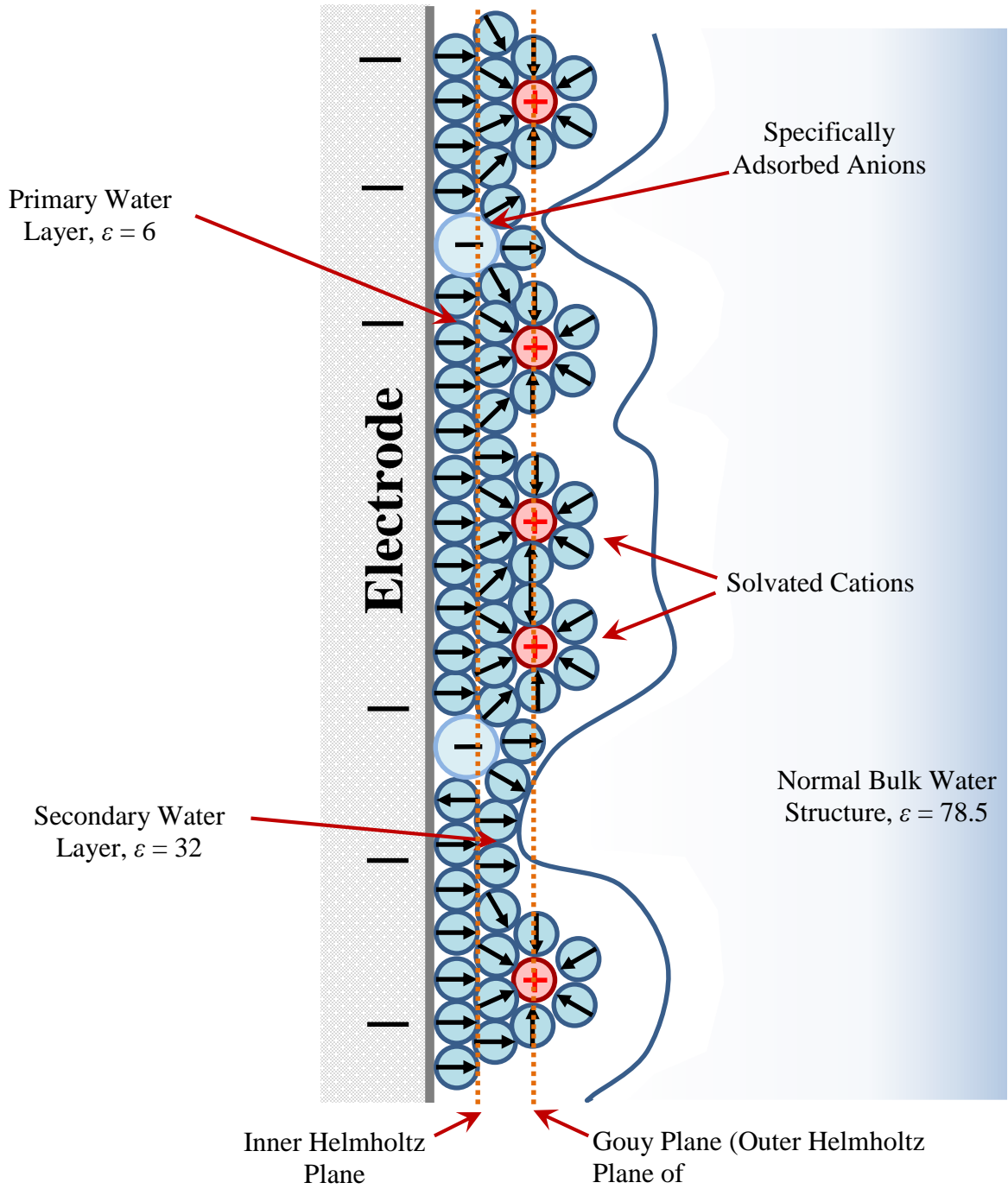
the usage of dopamine. Water by itself permits only a 10Å electron tunneling distance by when supporting a 10^3 /sec electron transfer rate between an electron donor and electron acceptor site [115]. For the same electron-transfer-rate, proteins allow an electron donor to acceptor center distance of about 20Å and on other biologically relevant time scales up to 25 Å [115][118][120]. Though dopamine is not a protein, it shares some characteristic with proteins. First, like most proteins, dopamine has a carbon backbone and is adorned with hydrogens. Dopamine has double bonded oxygens which are part of the peptide bond construction of all proteins. The catecholamine shares a trait with the amino acid lysine in that they both have a protonated terminus amine group.

But perhaps the most fortuitous factor with the usage of dopamine in this work could be correlated to its partial similar structure to ammonia. Ammonia has a small β , meaning it has a better electron conducting capacity [118]. This allows ammonia to have a much larger operative electron transfer length of upwards 100 Å between an electron donor and electron acceptor site [118]. This relates to dopamine, because it has an amine group, which is ammonia-like in structure. For both ammonia and the amine group, there is nitrogen and hydrogens present and likewise, both ammonia and amine can become protonated and have similar tetrahedral conformations [119]. These resemblances may help confer the electron tunneling characteristics seen in ammonia to a dopamine solution, if not in full, perhaps to some degree.

Another concept which maybe assisting the Debye-like signature in the comparative Cottrell current response, is structured water on the electrodes when a potential is applied. The Bockris-Devanathan-Muller (BDM) model was developed in 1963 as an extension of the Gouy-Chapman-Stern model (Figure 14). The BDM model takes into the account how a polar solvent, like water, will interact with the electrode, aligning itself on the basis of its dipole in relation to the electrode's surface charge as seen in Figure 46 [53][108]-[110]. The alignment restricts the movement of the water molecules and imparts a structure to the layers of water molecules [53][108]-[110]. This includes the presence of specifically and non-specifically absorbed ions. The resulting structure limits the degrees of freedom of the

molecules and as an outcome, the BDM model adjusts the dielectric, ϵ , values of the layers [53][108]-[110]. This modification helped to address some differences in experimental capacitance measurements [53]. The dipoles of subsequent layers are aligned to lesser extent, until they are completely random in the bulk water [126]. The reason BDM model is interesting is because structured water has also been studied in biological systems, where it has been shown in simulation and experiment to aid electron tunneling associated with ordered orientations of water [122][124][125]. By analogy, similar processes could be occurring in the electrode's vicinity, except instead of being points of redox activity as it is in biological systems, it is more like a zone or volume. Indeed, terminology by Compton et al refers to it as a "plane of electron transfer", or PET for short.

Figure 46: The Bockris-Devanathan-Muller (BDM) model. The BDM model adds further detail to the Gouy-Chapman-Stern model by taking into account the polar nature of water, describing how the dipoles align on the electrode surface and elsewhere, giving a structure to the water molecules [53][108]-[110]. This limits the degrees of freedom of the molecules and adjusts the dielectric, ϵ , values of the electric double layer as shown above. The surface potential decreases in the Inner Helmholtz and Gouy planes as before, and beyond that declines as in the Gouy-Chapman model [108].



To quickly discuss the aspects learned from biological systems, in proteins this “structured water” pertains to protein residues momentarily holding water molecules sterically constrained with an alignment dictated by the attraction/repulsion between the charge on the residue and water’s dipoles [124][125]. This can create a pathway for electron transfer referred to as “water-mediated electron tunneling” or “water bridge” between redox donor and acceptor sites [122][123][124][125]. The structured water provides strong electron tunneling routes between cofactors that would be unlikely to interact otherwise due to van der Waals gaps [122]. Simulations and experimental data indicate electron transfer can occur between two sites along a pathway composed of hydrogen bonds and covalent bonds [123]. Lin, Balabin and Beratan have described the structured regime as occurring between 9 and 12 Å and also conclude that a small amount of structured water molecules can enhance electron transfer between donor and acceptor cofactors [123]-[125]. More specifically they hypothesize that “water may be a particularly strong tunneling mediator when it occupies a sterically confined space between redox cofactors with strong organizing forces that favor constructively interfering coupling pathways” [123][125]. Though the 9 to 12 Å from structured water is a small value, along with the other influences of a large V/m field near the electrode, tunneling seen in protein and dopamine’s similarities to protein, tunneling seen in ammonia and dopamine’s similarities to ammonia, there could be a cumulative effect which may allow the electrode interact with a volume of solution around of it to cause the Debye-like signature in the Cottrell comparison.

With the background about the possible mechanisms at work, it is possible to fully explain how it was reasonable to fit the Cottrell equation multiplier to different equation types for the remaining platinum testing scenarios of 3b (Figure 47) and 4a (Figure 48).

The first fitting was to equation of the form (8) because the compared response of measured current divided by expected current yielded a curve resembling an inverse concentration correlation. For convenience, it is listed here again, with a and b as constants and C , the concentration.

$$S = \frac{a}{\sqrt{C}} + b \quad (8)$$

An exponential function can be used to describe the profile of the potential drop off from the electrode surface into the double layer [53]. Also as seen in (12), an exponential can be used to describe electron tunneling. For these reasons, the curve fitting introduced an exponential function element with a constant, m , to the form seen in (8) to generate a function of the type seen in (13) below.

$$S = \frac{ae^{mC}}{\sqrt{C}} + b \quad (13)$$

The last equation fitting was done to an expression with just an exponential and an offset, b , removing the inverse square root of the concentration relation to create an equation of the form given in (14).

$$S = ae^{mC} + b \quad (14)$$

These selections of equation fitting show that the Cottrell equation multiplier, S , behaves in a way that is consistent with ways used to describe the electric double layer width. This suggests the current is being modulated by an aspect of the double layer size based upon the concentration of the dopamine solution.

Figure 47 shows for Scenario 3b how the function, (9), is fitted with a and b to approximate the times larger the electrical current measurement is compared to that predicted by the Cottrell equation. Also given are exponential forms from equations (13) and (14).

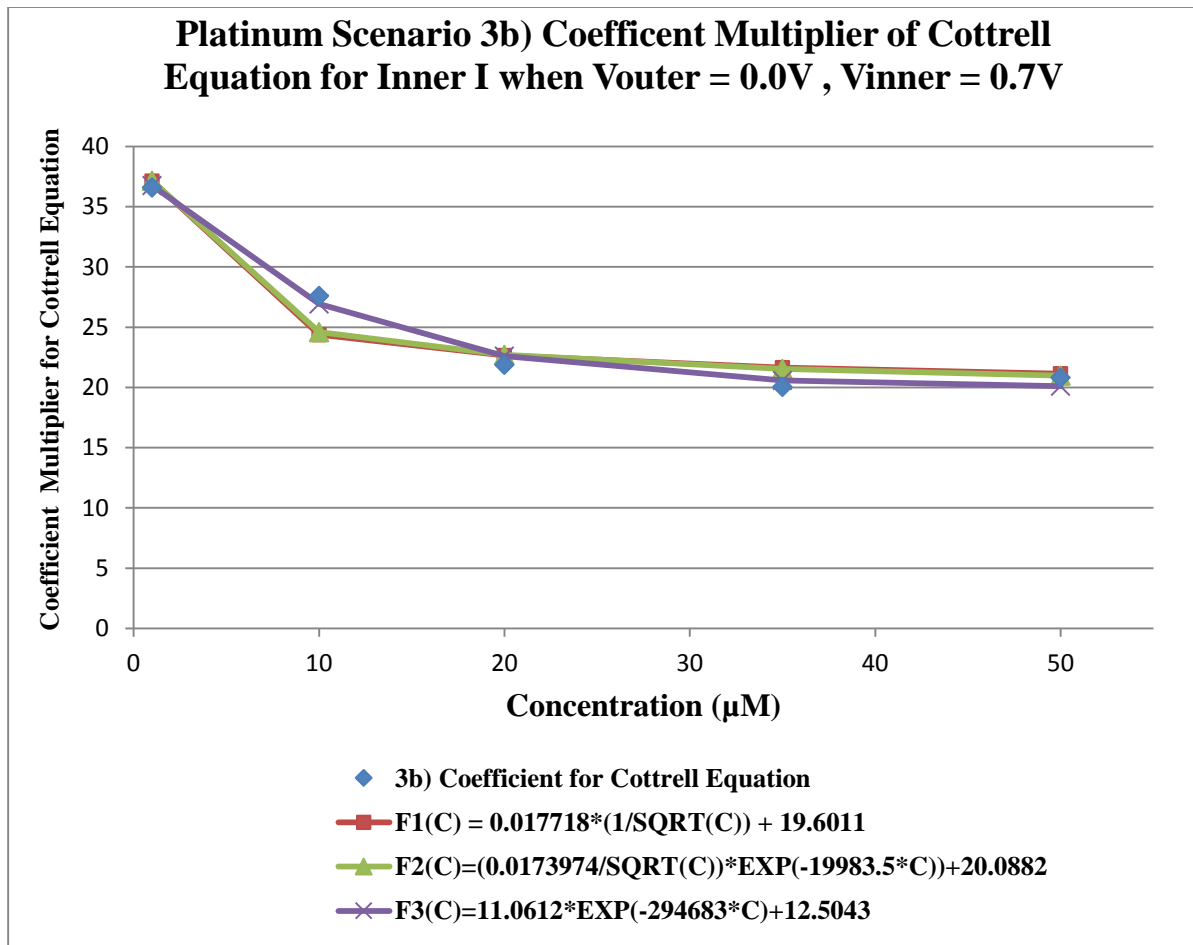


Figure 47: Platinum Scenario 3b) Coefficient Multiplier of Cottrell Equation for Inner I when $V_{outer} = 0.0V$, $V_{inner} = 0.7V$. The blue diamond markers are the measured multiplier coefficient for the Cottrell equation derived from dividing the measured current by the expected Cottrell equation prediction. The red box line for $F1(C)$ is an equation matching the blue line of the form given by (8). $F2(C)$ is an equation of form (13), while $F3(C)$ is an exponential based expression of the type seen in equation (14). The R-squared value for $F1(C)$ is 0.9109, $F2(C)$ is 0.9365 and $F3(C)$ is 0.991.

Below, in Figure 48, the same multiplier function from (108) and the exponential forms, (13) and (14) are applied and as shown, approximate the Scenario 4a test results.

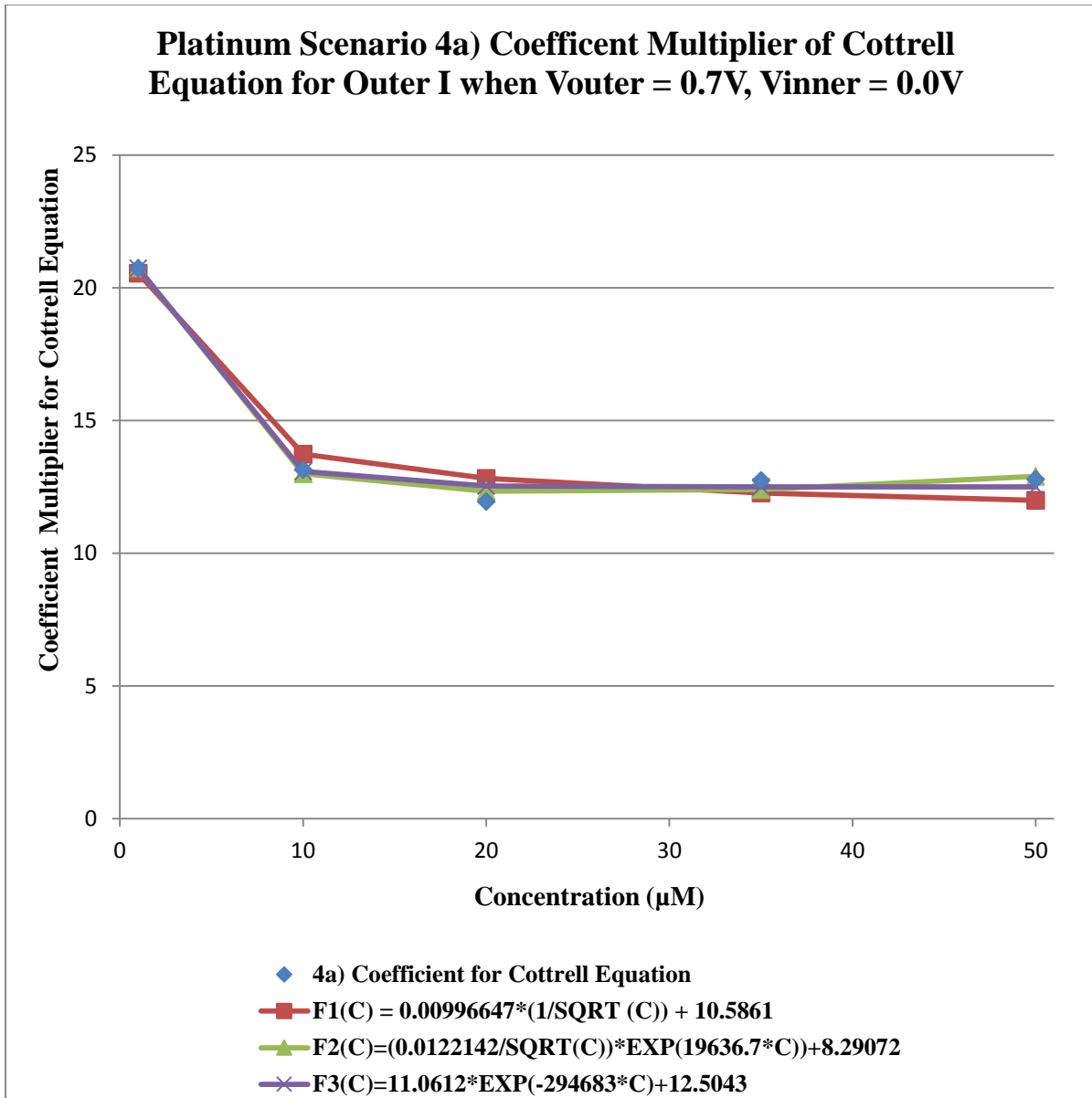


Figure 48: Platinum Scenario 4a) Coefficient Multiplier of Cottrell Equation for Outer I when $V_{outer} = 0.7V$, $V_{inner} = 0.0V$. The blue diamond markers are the measured multiplier coefficient for the Cottrell equation derived from dividing the measured current by the expected Cottrell equation prediction. The red box line, $F1(C)$, is an equation matching the blue line of the form given by (8). $F2(C)$ is an equation of form (13), while $F3(C)$ is an exponential based expression of the type seen in equation (14). The R-squared value for $F1(C)$ is 0.9626, $F2(C)$ is 0.9942 and $F3(C)$ is 0.991.

A difference between the Scenarios that are only a constant multiplier of the Cottrell equation, Table 7, and those that require a function, 3b and 4a, are the potentials of the electrodes. In Table 7 test, both electrodes have either a positive or negative potential on them, neither is every at a 0V potential.

However for Scenarios 3b and 4a, there is only one electrode at a time that has a potential on it. That potential is a positive oxidizing potential on it and the opposite electrode was held at 0 volts. These voltages conditions were necessary to generate a multiplying coefficient to the Cottrell equation that followed the function shown in (8).

For comparison, the testing Scenarios 3b and 4a measured multipliers are plotted together in Figure 49. As the graph shows, the inner and outer electrode curves are close to parallel and separate from one another.

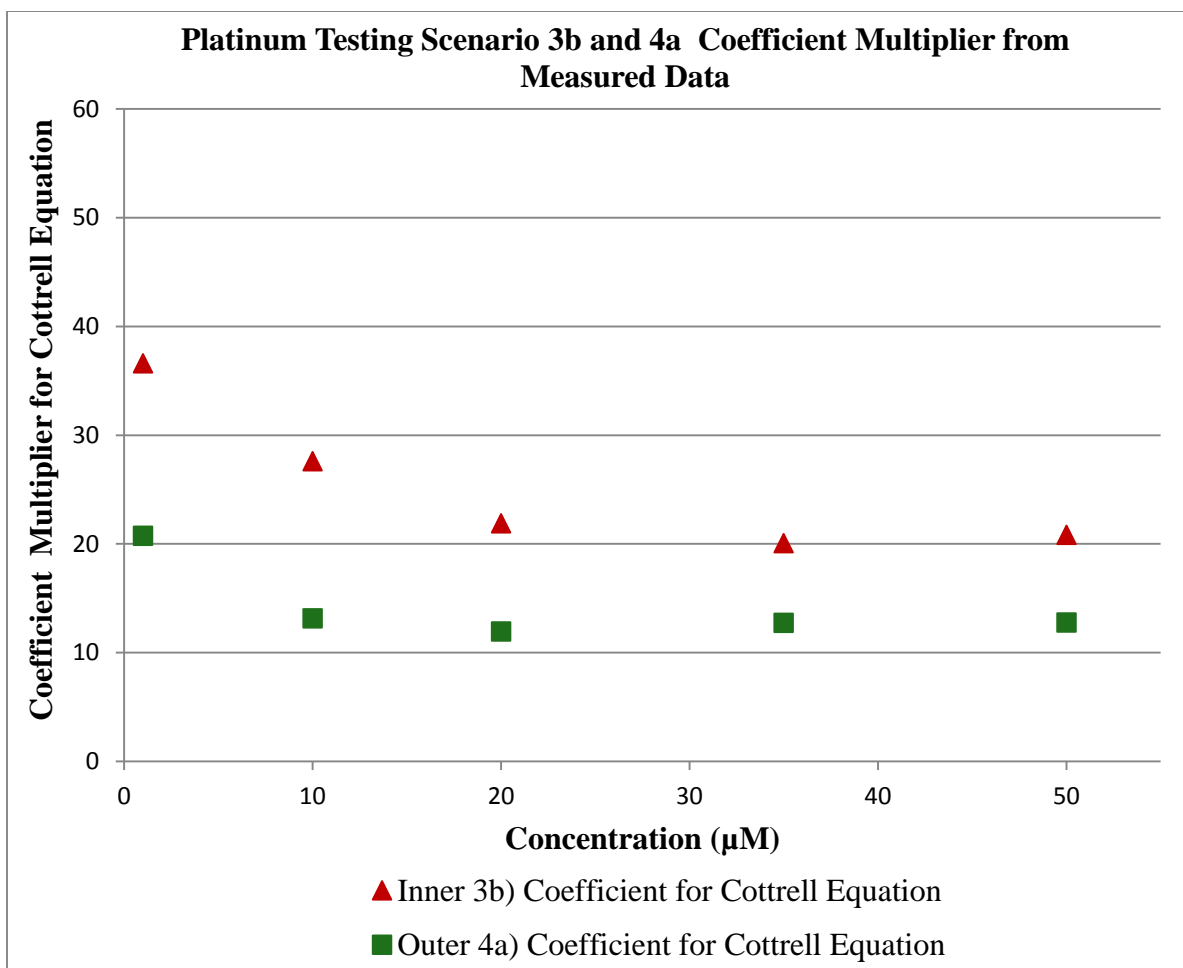


Figure 49: Plot of the measured platinum coefficient multipliers. These are the blue diamond lines from the previous 2 graphs, (Figure 47 and Figure 48) derived from taking the measured current value and dividing by the Cottrell equation prediction. The inner and outer electrode results are nearly parallel but are separate.

3.5 Carbon PPF Sensor Electrode Oxidative and Reduction Results

The carbon PPF sensors were tested in a manner identical to the testing done on the platinum sensors (Table 1 and Table 2). The dopamine concentrations for the carbon PPF sensors were the same as the ones used for the platinum sensors. In fact the dopamine solutions used for both platinum and carbon PPF came from the same source solution in

order to aid the comparison of the two kinds of devices. The only difference between platinum and carbon PPF sensors came with the data processing. The offset could not be adjusted utilizing the method done for the platinum sensors where the PBS-only background currents were subtracted. Other offset removal techniques were attempted, but did not produce suitable results. Consequently the data was analyzed without an offset subtraction.

Table 8, below, shows the findings and interpretation of results for Scenario 1 for the outer and inner carbon PPF electrodes.

Table 8: Carbon Scenario 1, Outer Electrode: Square Wave -0.4V to+0.7V, 10 sec cycle, Inner Electrode: Constant -0.4V				
Description	Measuring	Outer Electrode Potential	Inner Electrode Potential	Response Results
Scenario 1a	Outer Electrode Current	+0.7V	-0.4V	Linear, oxidative, concentration dependent curve (See Figure 50)
Scenario 1b	Inner Electrode Current	+0.7V	-0.4V	Linear, reduction, concentration dependent curve (See Figure 51)
Scenario 1c	Outer Electrode Current	-0.4V	-0.4V	Non-informative (not shown)
Scenario 1d	Inner Electrode Current	-0.4V	-0.4V	Non-informative (not shown)

Both scenarios 1a and 1b produced linear responses. Scenario 1a was an oxidative response current where the outer electrode was converting the dopamine to dopamine-o-

quinone with its positive 0.7V potential show in Figure 50. The earlier test of the platinum sensor also showed a linear, oxidative curve for Scenario 1a. The carbon PPF 1b response curve was a linear, reduction response curve as shown in Figure 51. In contrast, the platinum Scenario 1a curve was non-informative.

As expected, the carbon PPF scenarios 1c and 1d had response results that were not informative.

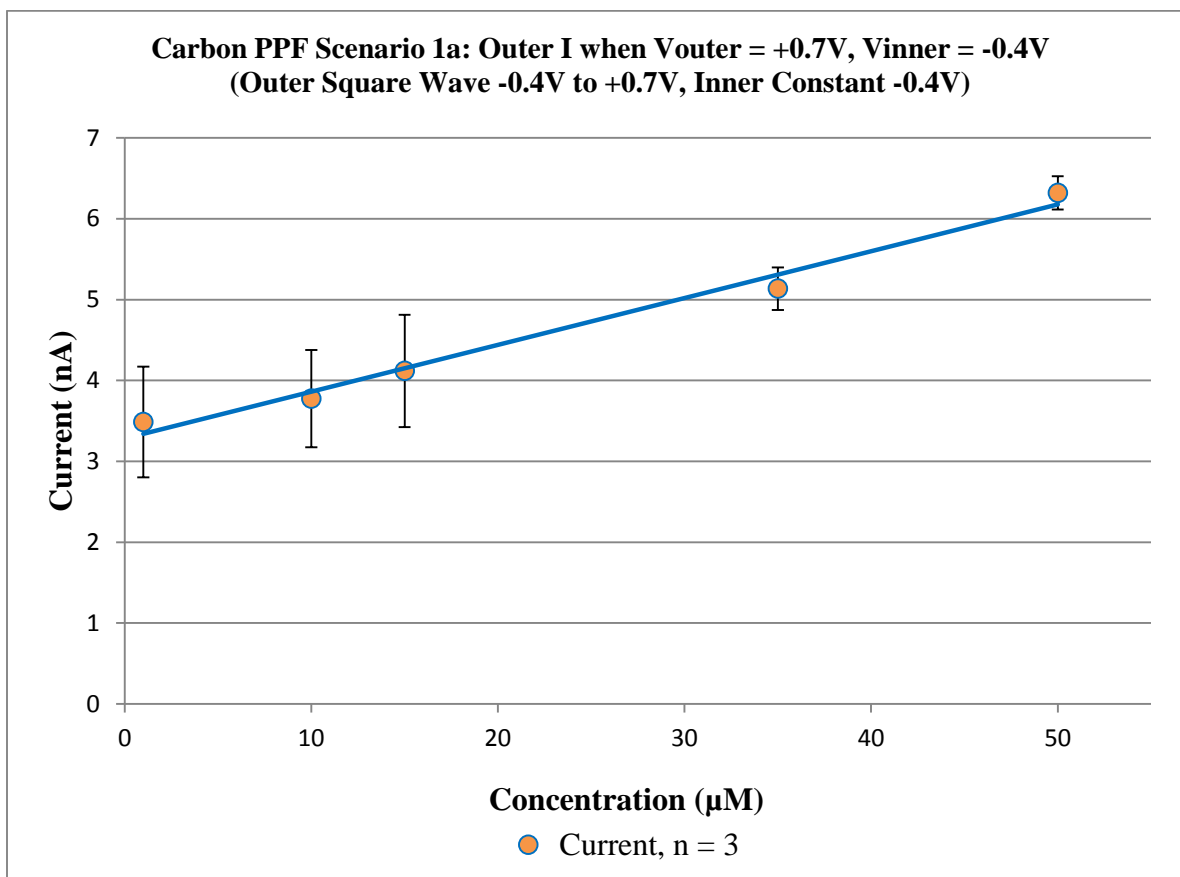


Figure 50: The carbon PPF sensors have a linear, oxidative concentration dependent curve for the outer electrode current in Scenario 1a where the outer electrode was at +0.7V and the inner electrode was at -0.4V. Error bars are one standard deviation.

Scenario 1b was a reduction response current that occurred because the inner electrode was at -0.4V, reducing the outer electrode produced dopamine-o-quinone to dopamine. The results can be seen below in Figure 51. Unlike the platinum sensor, the 1b carbon PPF test showed an inner electrode that was sensitive to the dopamine-o-quinone being produced by the outer electrode. It is expected that this difference is due to the platinum sensors not having a vertical component to the sensor above the substrate as the carbon PPF sensors possess. The electrodes protruding from the surface creates a channel where electrode surfaces are parallel to one another as can be seen in Figure 22. The two electrode surfaces facing each other directly could give the dopamine-o-quinone a higher probability of interacting with the inner electrode for two reasons. First, the diffusive random walk path the molecule starts on is a perpendicular path to the surface of the outer electrode. Second, the substrate lining the bottom of the channel acts like a reflector, redirecting dopamine-o-quinone molecules, giving them an additional chance to interact with the inner electrode. In contrast, for the platinum electrode there isn't a channel since the electrodes are flush with the surface. Also for the platinum sensors, the substrate does not reflect any molecules in a way that helps them interact with the opposing electrode because the substrate is planar with the electrodes.

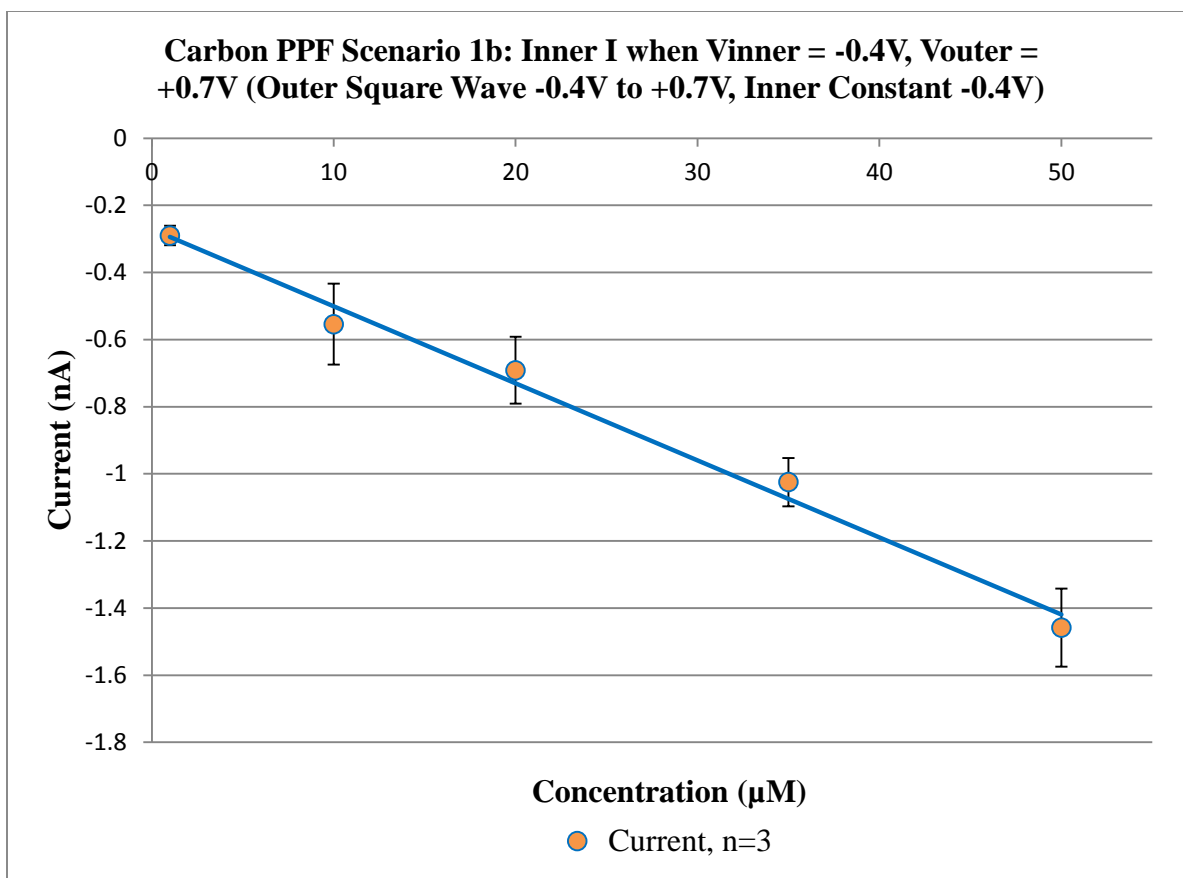


Figure 51: The carbon PPF sensors have a linear, reduction concentration dependent curve for the inner electrode current in scenario 1b where the inner electrode is at $-0.4V$ and the outer electrode is at $+0.7V$. Such a reduction curve for Scenario 1b was not seen in the platinum sensors. This could be due to the platinum sensors not having a vertical component to the sensor above the substrate as the carbon PPF sensors have. The vertical component of the carbon PPF sensor resulting channel may give the dopamine-o-quinone a higher probability of interacting with the inner electrode. Error bars are one standard deviation.

In the next test, Scenario 2, the inner electrode was held at dopamine's oxidation potential, $0.7V$, and the outer electrode had a square wave cycling between an oxidation potential ($0.7V$) for dopamine and a reducing potential ($-0.4V$) for dopamine-o-quinone. As with the platinum sensors, this scenario explored the shielding effect between electrodes and characterized the influence of the outer electrode on the inner electrode for dopamine oxidation.

Table 9 summarizes the results of testing Scenario 2 for the carbon PPF electrodes.

Table 9: Carbon Scenario 2, Outer Electrode: Square Wave -0.4V to +0.7V, 10 sec cycle, Inner Electrode: Constant +0.7V				
Description	Measuring	Outer Electrode Potential	Inner Electrode Potential	Response Results
Scenario 2a	Outer Electrode Current	+0.7V	+0.7V	Linear, oxidative, concentration dependent curve (See Figure 52)
Scenario 2b	Inner Electrode Current	+0.7V	+0.7V	Linear, oxidative, concentration dependent curve, screening of inner electrode (See Figure 53)
Scenario 2c	Outer Electrode Current	-0.4V	+0.7V	Linear, reduction, concentration dependent curve (See Figure 54)
Scenario 2d	Inner Electrode Current	-0.4V	+0.7V	Linear, oxidative, concentration dependent curve, no effect from outer electrode (See Figure 55)

In Scenario 2, three out of four response results, 2a, 2b and 2d, produced linear, oxidative, concentration dependent curve responses. Scenario 2c produced a linear, reduction concentration dependent curve response.

Figure 52 shows the response of the carbon PPF sensors for Scenario 2a.

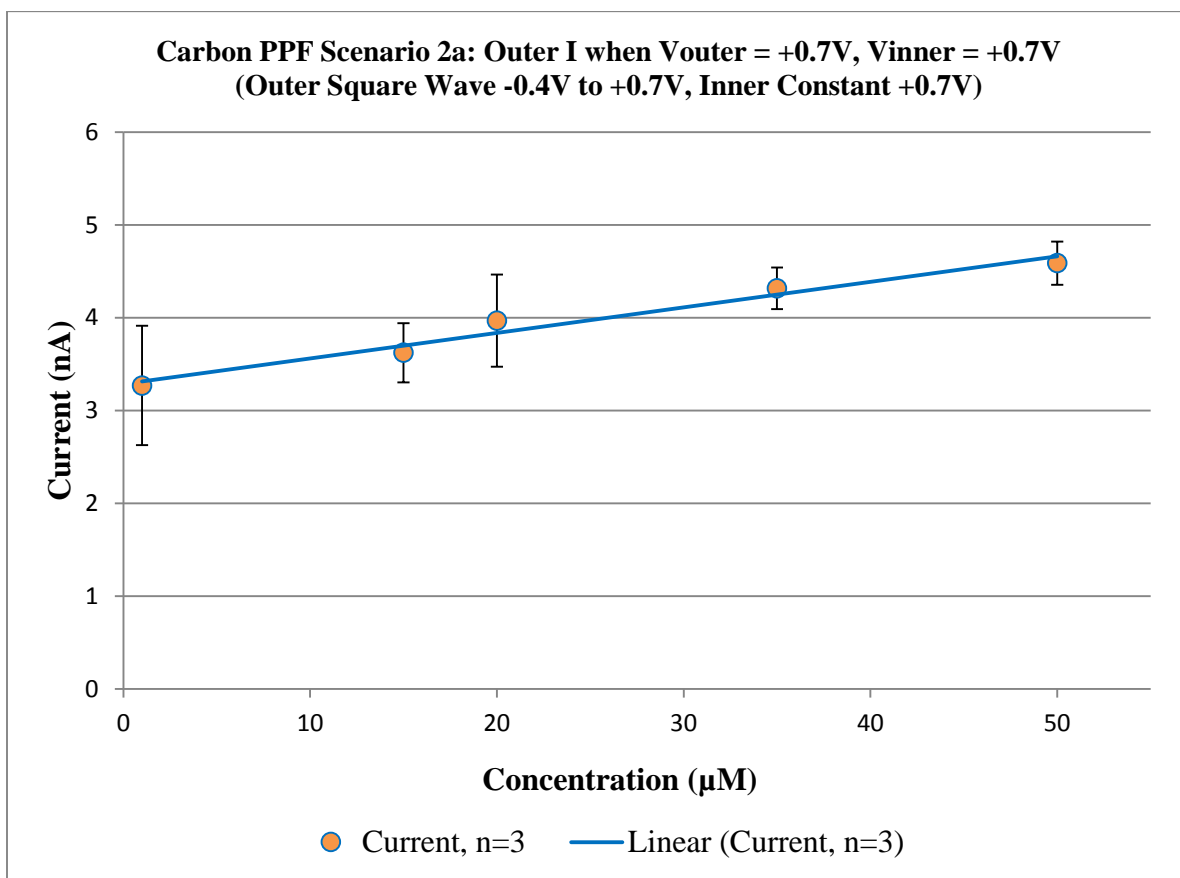


Figure 52: Carbon PPF sensors have a linear, oxidative concentration dependent curve for the outer electrode current in Scenario 2a. Error bars are one standard deviation.

Scenario 2b examined a screening effect of the inner electrode and the results for the test can be seen below in Figure 53. Later, in Figure 58, a comparison can be seen between the tests and how the shielding reduces the electrode oxidation rate.

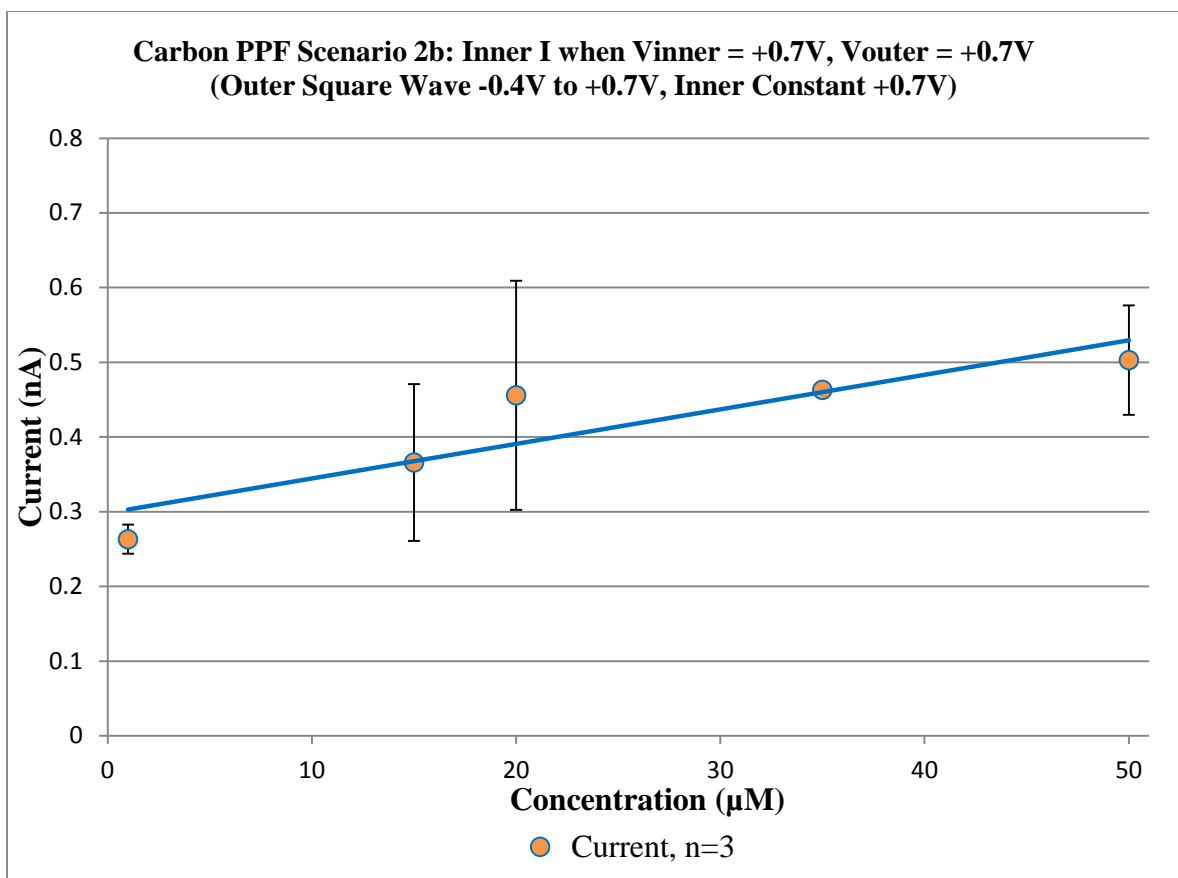


Figure 53: Carbon PPF sensors have a linear, oxidative concentration dependent curve for the inner electrode current in Scenario 2b. The error bars are one standard deviation.

Scenario 2c investigated if a reduction current could be measured on the outer electrode from the dopamine-o-quinone produced at the inner electrode. A linear and concentration dependent reduction current response was seen as shown in Figure 54. Unlike the platinum sensor, which had a response that plateaued, the carbon PPF had a reduction current which grew with increasing concentration. As with the carbon PPF scenario 1b, the 2c results may have been attainable because the carbon PPF sensors have electrodes with sides facing one another and the substrate acting as a reflecting surface that restricts dopamine-o-quinone molecules from completely diffusing away. Again these are two benefits the platinum sensors do not have.

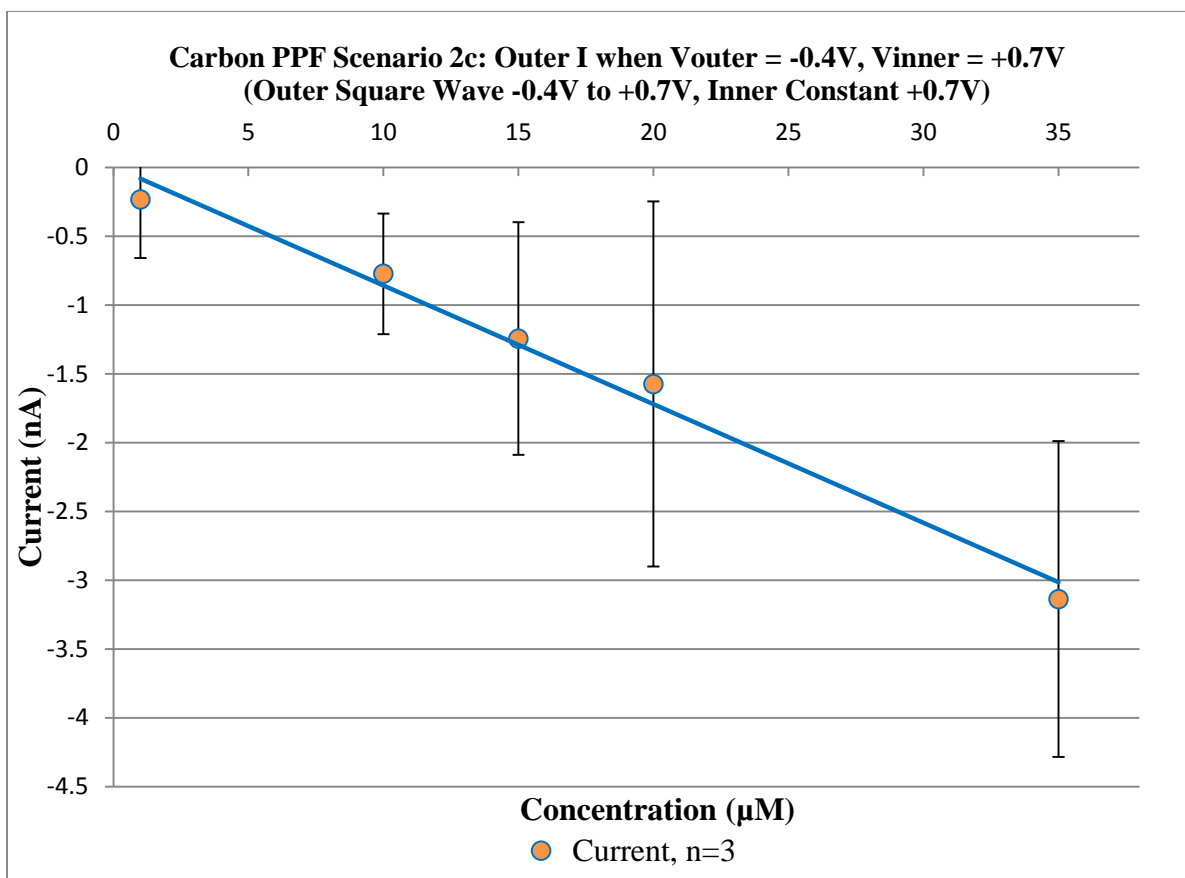


Figure 54: A reduction current was measured on the outer electrode in Scenario 2c for the carbon PPF sensors unlike the platinum sensors. The error bars are one standard deviation.

Scenario 2d examined how the inner electrode oxidation current when the outer electrode potential was $-0.4V$. A linear response was seen as seen in Figure 55. A comparison to other oxidation rates of the carbon PPF electrodes can be seen in Figure 58.

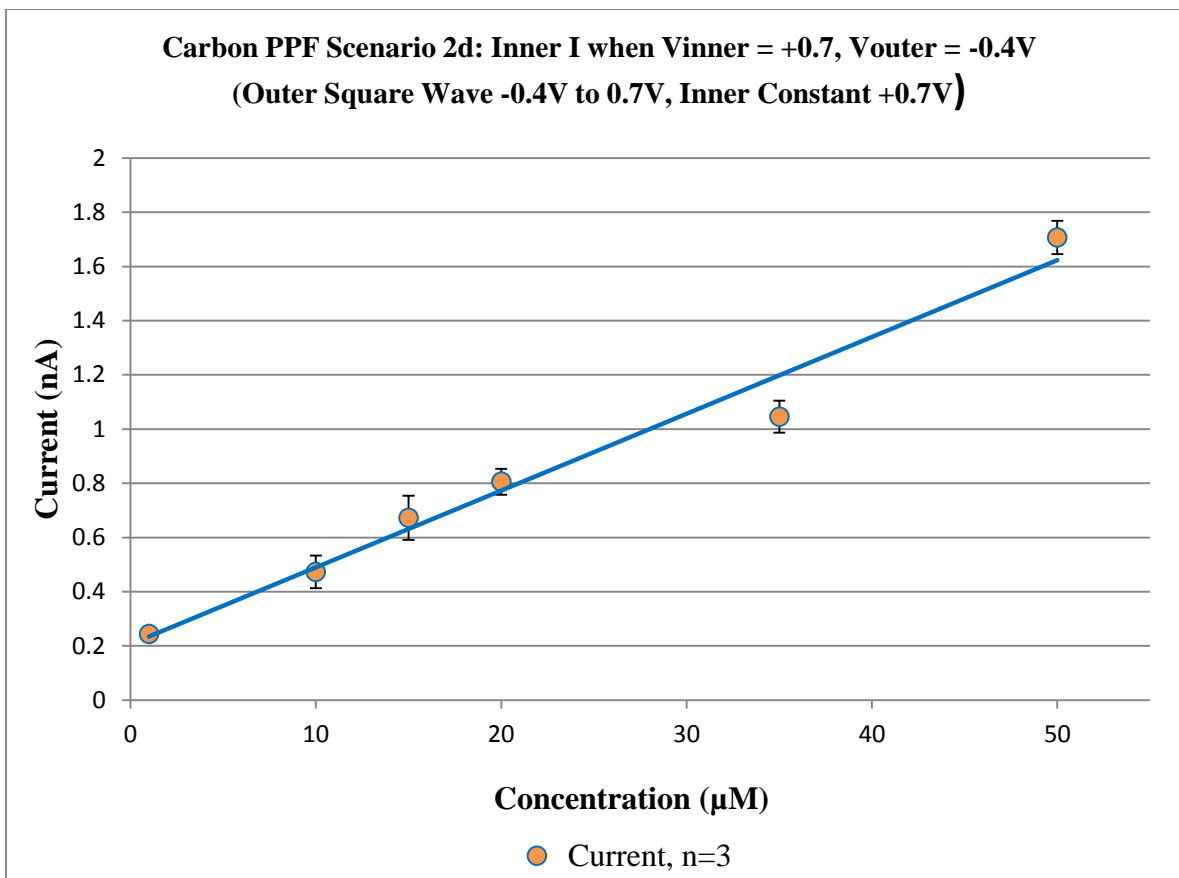


Figure 55: Scenario 2d for the carbon PPF sensors produce a linear, oxidative concentration dependent curve for the inner electrode current. Error bars are one standard deviation.

Scenario 3 put the square wave on the inner electrode and held the outer electrode at a constant 0V potential. The results for scenario 3 are summarized in Table 10.

**Table 10: Carbon PPF Scenario 3, Outer Electrode: Constant 0V
Inner Electrode: Square Wave -0.4V to +0.7V, 10 sec cycle**

Description	Measuring	Outer Electrode Potential	Inner Electrode Potential	Response Results
Scenario 3a	Outer Electrode Current	0V	+0.7V	Non-informative (not shown)
Scenario 3b	Inner Electrode Current	0V	+0.7V	Linear, oxidative, concentration dependent curve (See Figure 56)
Scenario 3c	Outer Electrode Current	0V	-0.4V	Non-informative (not shown)
Scenario 3d	Inner Electrode Current	0V	-0.4V	Non-informative (not shown)

Scenarios 3a, 3c and 3d did not give informative results.

For the carbon PPF sensors, scenario 3b produced a linear, oxidative concentration dependent curve for the inner electrode as seen in Figure 56.

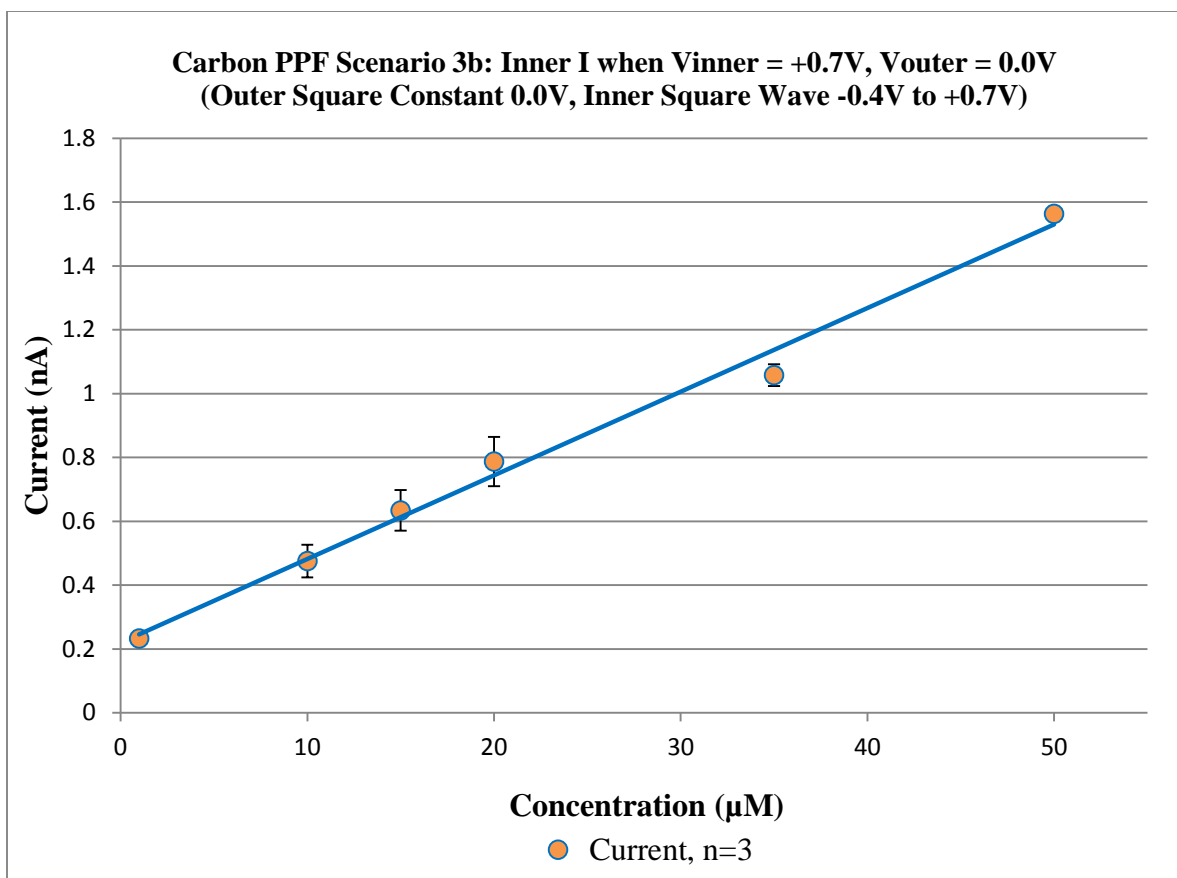


Figure 56: Scenario 3b for the carbon PPF sensors produced a linear, oxidative concentration dependent curve for the inner electrode current. The error bars are one standard deviation.

Scenario 4's results are shown in Table 11. For this test, the square wave of oxidation and reduction potentials was placed on the outer electrode, while the inner electrode was held at 0V.

Table 11: Carbon Scenario 4, Outer Electrode: Square Wave -0.4V to +0.7V, 10 sec cycle, Inner Electrode: Constant 0V				
Description	Measuring	Outer Electrode Potential	Inner Electrode Potential	Response Results
Scenario 4a	Outer Electrode Current	+0.7V	0V	Linear, oxidative, concentration dependent curve (See Figure 57)
Scenario 4b	Inner Electrode Current	+0.7V	0V	Non-informative (not shown)
Scenario 4c	Outer Electrode Current	-0.4V	0V	Non-informative (not shown)
Scenario 4d	Inner Electrode Current	-0.4V	0V	Non-informative (not shown)

Scenarios 4b, 4c and 4d did not produce responses that were useful for background current subtraction.

However, testing Scenario 4a produced a linear, oxidative, concentration dependent response for the outer electrode as seen in Figure 39.

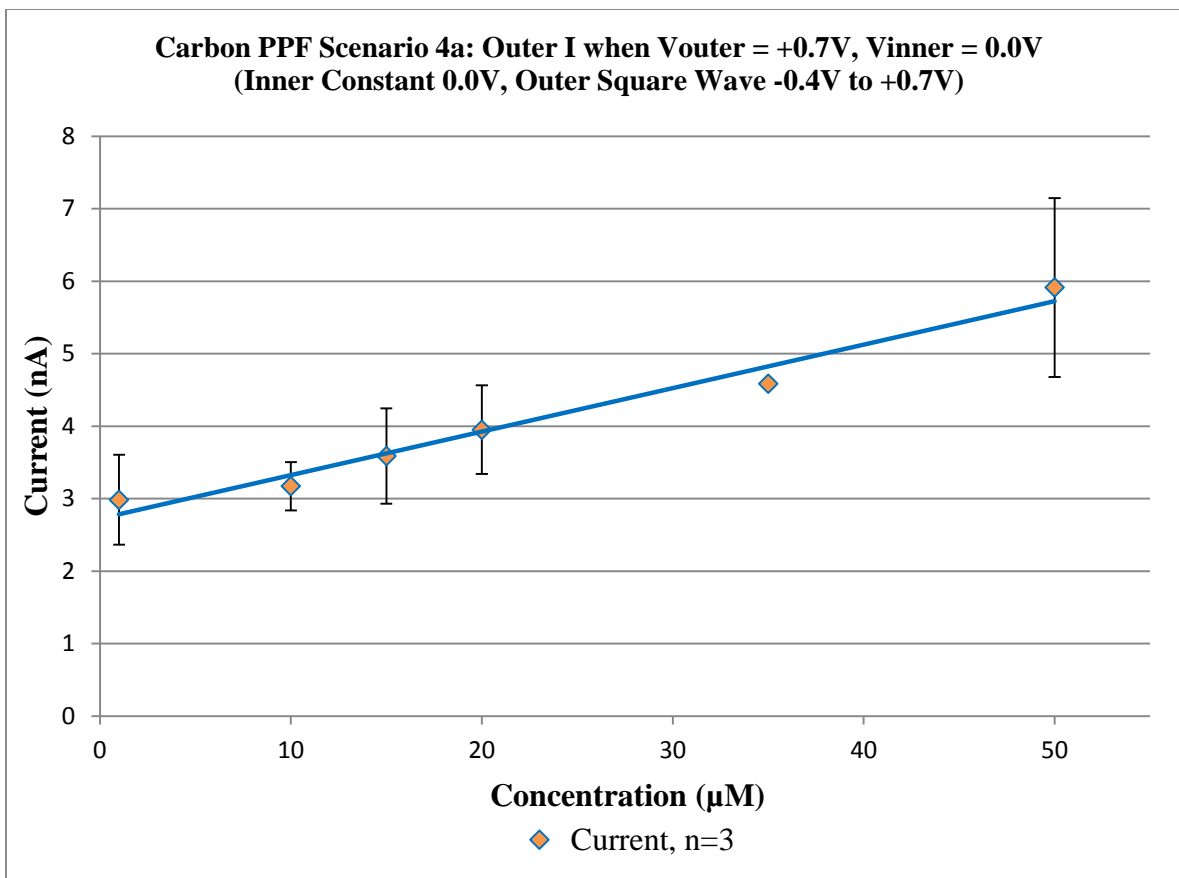


Figure 57: Carbon PPF sensors have a linear, oxidative concentration dependent curve for the inner electrode current in Scenario 4a. The error bars are one standard deviation.

As with the platinum sensors, to make the carbon PPF electrode response comparisons more apparent, all the oxidative graph slopes ($nA/\mu M$) were calculated and plotted together on the same graph as seen in Figure 58.

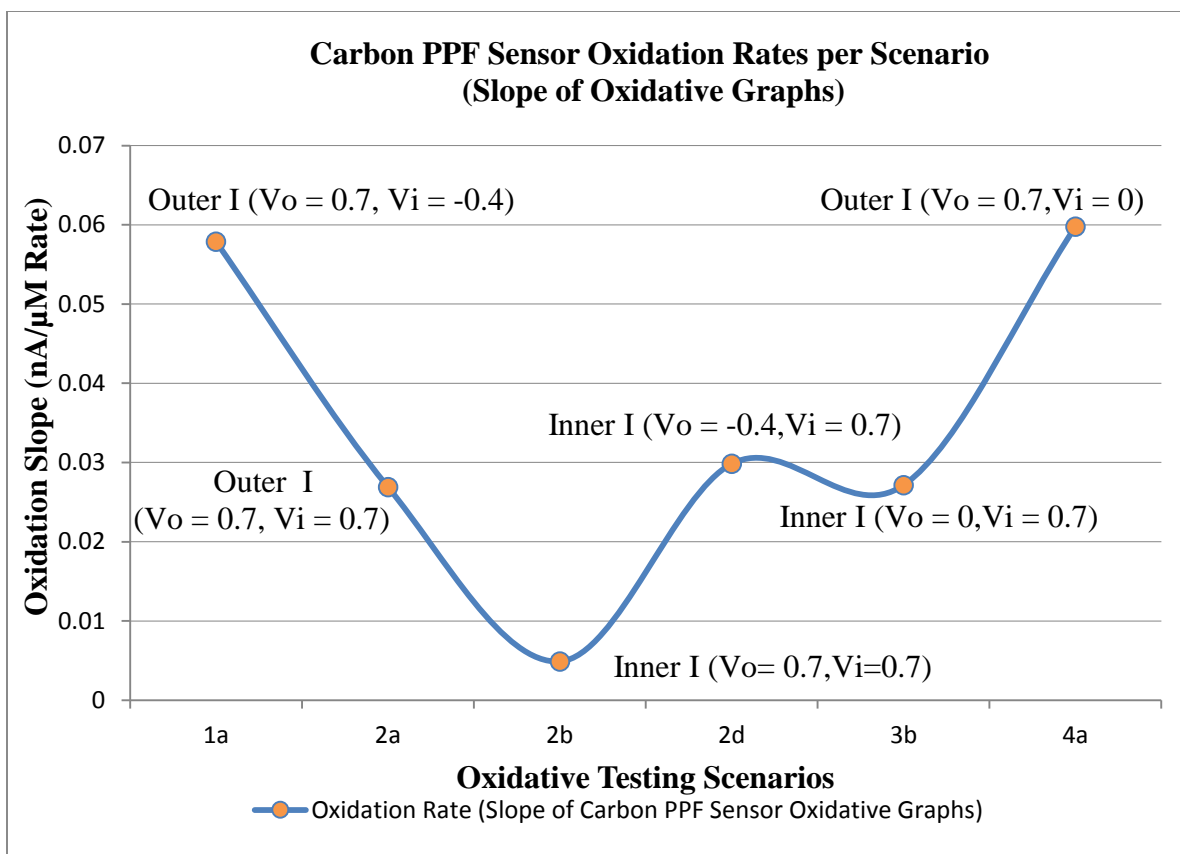


Figure 58: Carbon PPF sensor oxidation rates per scenario in nA/ μ M.

The chart in Figure 58 shows how the oxidative rate on the outer electrode is very similar whether the inner electrode is at -0.4V (Scenario 1a) or at 0V (Scenario 4a). However, if the outer electrode is oxidizing dopamine, it can be affected by the inner electrode if the inner potential is also at an oxidizing potential (Scenario 2a). The shielding, or competition, between outer and inner electrode to oxidize dopamine reduces the rate of oxidation on the outer electrode from an average of 5.9×10^{-2} nA/ μ M to 2.7×10^{-2} nA/ μ M, approximately a 54% decline.

A similar trend can be seen on the inner electrode oxidative graph slopes. When the inner electrode is oxidizing dopamine with a +0.7V potential, there is little difference for the inner electrode oxidation rate if the outer electrode is -0.4V or 0V (Scenarios 2d and 3b). However, when the inner electrode is at the oxidizing potential as well as the outer electrode,

as in Scenario 2b, then there is electrode shielding and competition for dopamine, reducing the inner electrode oxidation rate from an average 2.8×10^{-2} nA/ μ M to 4.9×10^{-3} nA/ μ M, approximately an 83% diminishment. The large decline is due to the competing outer electrode being larger in area than the inner electrode.

3.6 Carbon PPF Sensor Electrode Mass Transport

By using Faraday's Law of Electrolysis, (1), the mass transport flux of the carbon PPF sensors were also examined in the same fashion as were the platinum sensors.

Figure 59 shows how the outer electrode for a carbon PPF sensor had the highest mass transport flux for both electrodes. The outer electrode has maximum flux when there wasn't competition with the outer electrode for dopamine oxidation as seen in Scenarios 1a and 4a. When the outer electrode oxidation competes with the inner electrode for dopamine oxidation, there was some electrode shielding and the outer electrode mass transport flux drops as seen with the plot of Scenario 2a.

The next highest mass transport flux is in Scenarios 3b and 2d where the inner electrode was oxidizing dopamine and the outer electrode was at potentials that did not compete with the inner electrode, either 0V or -0.4V. When the outer electrode did compete with the inner electrode, the mass transport flux of the inner electrode dropped to the lowest level rate as seen in the plot of Scenario 2d.

However, the offsets for these carbon PPF mass transport cases were not removed as could be done with the platinum sensors. This means there would likely be some adjustment to the relative location of these flux curves if the proper offset removal could have been done. Since the platinum sensors were of comparable geometry, proportions, and had the same operating parameters as the carbon PPF sensors, that there should be similarities in the flux rates as well. This is also reasonable because related groupings of curves can be seen within the platinum and carbon PPF sensors. For instance, in both sensor types the curves for "Outer 1a" and "Outer 4a" are in close proximity to one other due to their similar operating condition and response. In addition, there is a similar increases in both curves from their starting point to their ending point. As these are outer electrodes, and larger in area, their

relative position on the graph should indicate a lower flux per unit area than the inner electrode. This indicates the carbon PPF background subtracted “Outer 1a” and “Outer 4a” mass transport response curves would most likely be in the mid-portion of the graph as seen in the platinum electrode mass transport graph in Figure 41.

A similar pairing can be seen with “Inner 3b” and “Inner 2d” current response curves for both platinum and carbon PPF response curves because of their similar operating parameters. As these are responses for the inner electrode, their flux rate should be higher per unit area than the outer electrodes. This is clearly seen in the platinum sensors of Figure 41. This would point toward the predicted carbon PPF sensors background subtracted “Inner 3b” and “Inner 2d” mass transport response curves to be at higher values above the carbon PPF “Outer 1a” and “Outer 4a” curves, in a similar relative location as seen with the platinum sensors, again from Figure 41.

Likewise, there are parallels with the electrode competing Scenarios of “Outer 2a” and “Inner 2b” between the platinum and carbon PPF sensors that can help place where the carbon PPF mass transport flux curves should be. As seen earlier, the larger outer electrode significantly impacts the performance of the inner electrode through shielding via dopamine competition. This would make it sensible that the carbon PPF “Inner 2b” mass transport flux response curve would have the smallest values, and be the lowest curve on the graph, as seen on the corresponding platinum sensor graph, Figure 41.

The “Outer 2a” carbon PPF mass transport flux was also one of electrode competition, but in this case the inner electrode would have less of an influence on the outer electrode than vice versa. As before, this mirrors the conditions of the platinum sensors, and it would be reasonable to suggest the relative position of the carbon PPF “Outer 2a” mass transport flux be higher than carbon PPF “Inner 2b” mass transport flux response curve.

Fortunately, the slopes of the carbon PPF sensors will not change no matter what the offset was and this allows for a direct comparison with platinum sensors in terms of responsivity, which is done in Table 13.

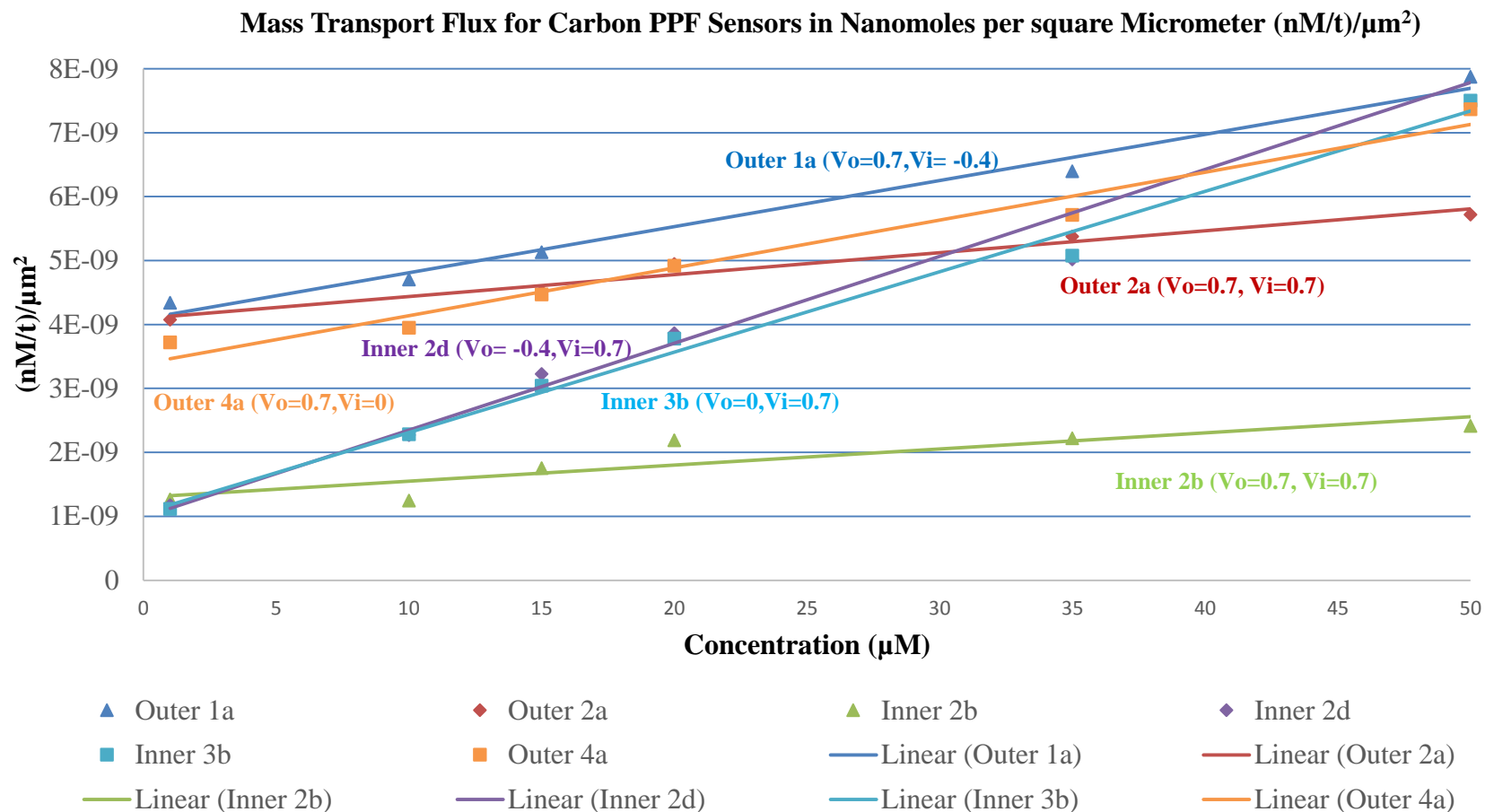


Figure 59: Mass Transport Flux for carbon PPF Sensors in Nanomoles per Second per Square Micrometer ($(\text{nM/t})/\mu\text{m}^2$) with linear regression lines. “Outer” and “inner” refer to the outer and inner electrodes respectively and are followed by the testing scenario.

A way to examine the responsiveness of the carbon PPF sensors without needing the background current offset is to look at the rates of the mass transport flux from Figure 59. This is also beneficial because it makes it possible later to compare the carbon PPF sensors to the platinum sensors with their own responsive slope rates. The carbon PPF flux rates of Figure 59 were plotted in Figure 60. The comparison between platinum and carbon PPF sensor mass transport flux rate is made in Table 13.

In comparing the mass transport flux results for the carbon PPF sensor, Scenarios 2d and 3b for the inner electrode were close in flux rate. This was when the inner electrode was not competing for dopamine with the outer electrode since the outer electrode was either at 0V or at -0.4V. As soon as there was competition, as in Scenario 2b, the mass transport rate fell from the approximate Scenario 2d and 3b average of $1.3 \times 10^{-10} \text{ ((nM/t)/}\mu\text{m}^2\text{)/}\mu\text{M}$ to Scenario 2b's rate of $2.5 \times 10^{-11} \text{ ((nM/t)/}\mu\text{m}^2\text{)/}\mu\text{M}$, a 81% decline. It is interesting to note that Scenario 2d has a slighter faster responsiveness than the other non-competing situation of Scenario 3b. Further study could clarify if this remains in a larger sample pool or is consistently present under these operating parameters.

For the outer electrodes, the mass transport rates were similar when only the outer electrode were actively oxidizing dopamine as in Scenario 1a and 4a. When the inner electrode also was oxidizing dopamine, the mass transport fell from the approximate Scenario 1a and 4a average of $7.3 \times 10^{-11} \text{ ((nM/t)/}\mu\text{m}^2\text{)/}\mu\text{M}$ to Scenario 2a's rate of $3.4 \times 10^{-11} \text{ ((nM/t)/}\mu\text{m}^2\text{)/}\mu\text{M}$, a 53% decrease.

Shielding, or competition, between electrodes is apparently greater when the inner electrode is being affected by the outer electrode, because the outer electrode has a larger surface area and flanks the smaller electrode on 2 sides.

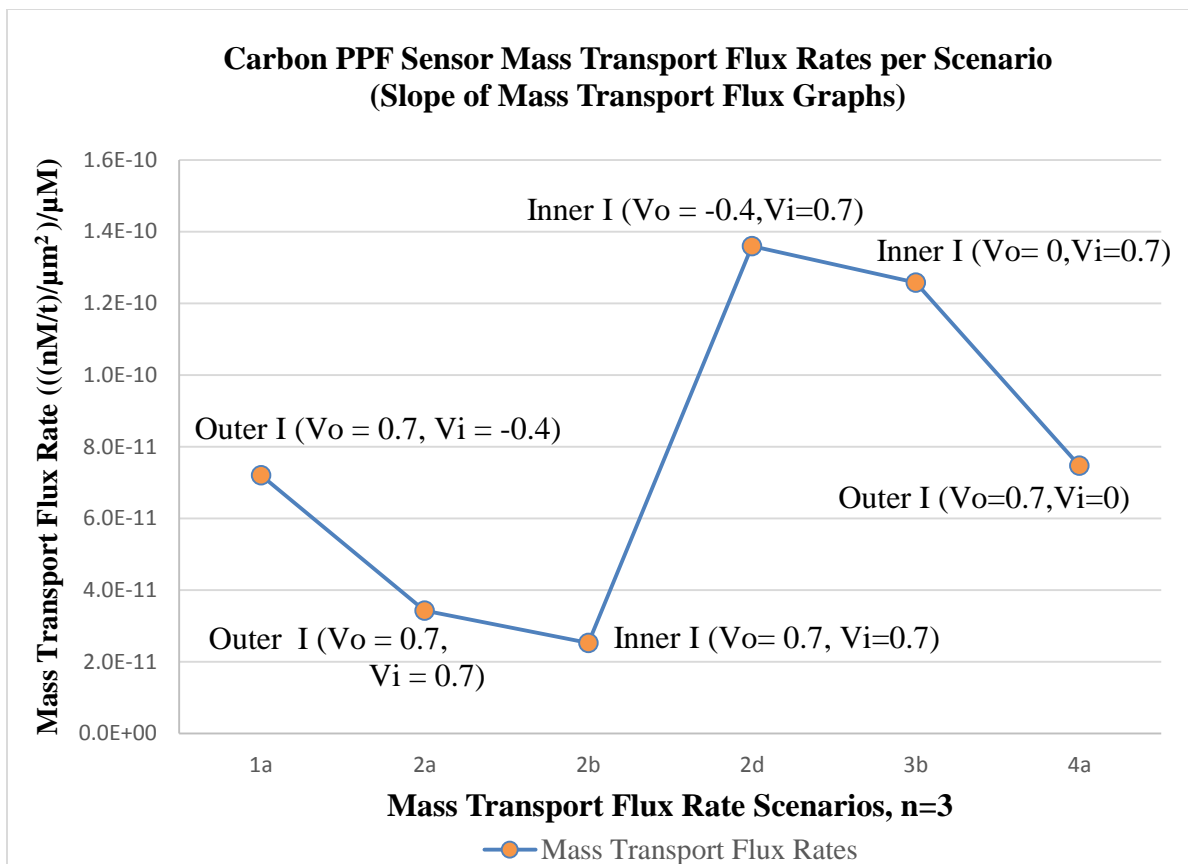


Figure 60: Carbon PPF sensor mass transport flux rates per scenario. The mass transport flux rate was greatest for the inner electrode in Scenarios 2d and 3b where there was not competition between inner and outer electrodes for dopamine oxidation. The next highest mass transport flux came from the outer electrode in Scenarios 1a and 4a where the outer electrodes did not have competition with the inner electrode for dopamine oxidation. Scenarios 2d and 3b were about twice the rate of 1a and 4a because the surface area of the larger electrode is larger than the inner electrode. The lowest mass transport flux was when the outer and inner electrode competed with one another as represented in Scenarios 2a and 2b. In these competitive shielding scenarios, the flux rate was nearly the same per unit area for both inner and outer electrode.

3.7 Carbon PPF Sensor Electrode Current Flux

The current flux per unit area of the carbon PPF sensors were also examined by taking the measured value of current and dividing per electrode area. The results for the analysis can be seen in Figure 61.

In comparing the electrical current flux rate, testing Scenarios 3b and 2d had similar values for the inner electrode. As seen with other trends, these were both where the inner electrode was not competing for the outer electrode for dopamine.

The two testing situations where there wasn't electrode competition or shielding for the outer were Scenarios 1a and 4a. They have a small difference between them, but run parallel to each other.

The Outer 2a and Inner 2b electrical current flux curves also run parallel to each another. However since the inner electrode in Scenario 2b is being competed against the larger electrode, the effect against it is more profound, giving it a lowered response rate than for the outer electrode in Outer 2a.

These 3 groupings of Figure 61 responses are similar as to what was seen in Figure 59 and Figure 41 for the platinum sensor current flux. The alignments of Figure 61 also mirror what was seen Figure 43 with the platinum type sensors for their electrical current flux in the various testing scenarios. Together this indicates the electrical current flux for the carbon PPF sensors relative positions would also have been adjusted if the offset could have been accurately defined. The order of carbon PPF electrical flux curves from top to bottom on the graph would most likely match the order the platinum sensors electrical flux curves of Figure 43 for reasons discussed in the previous section due to comparable geometry, proportions, and the same operating parameters shared between platinum and carbon PPF sensor types.

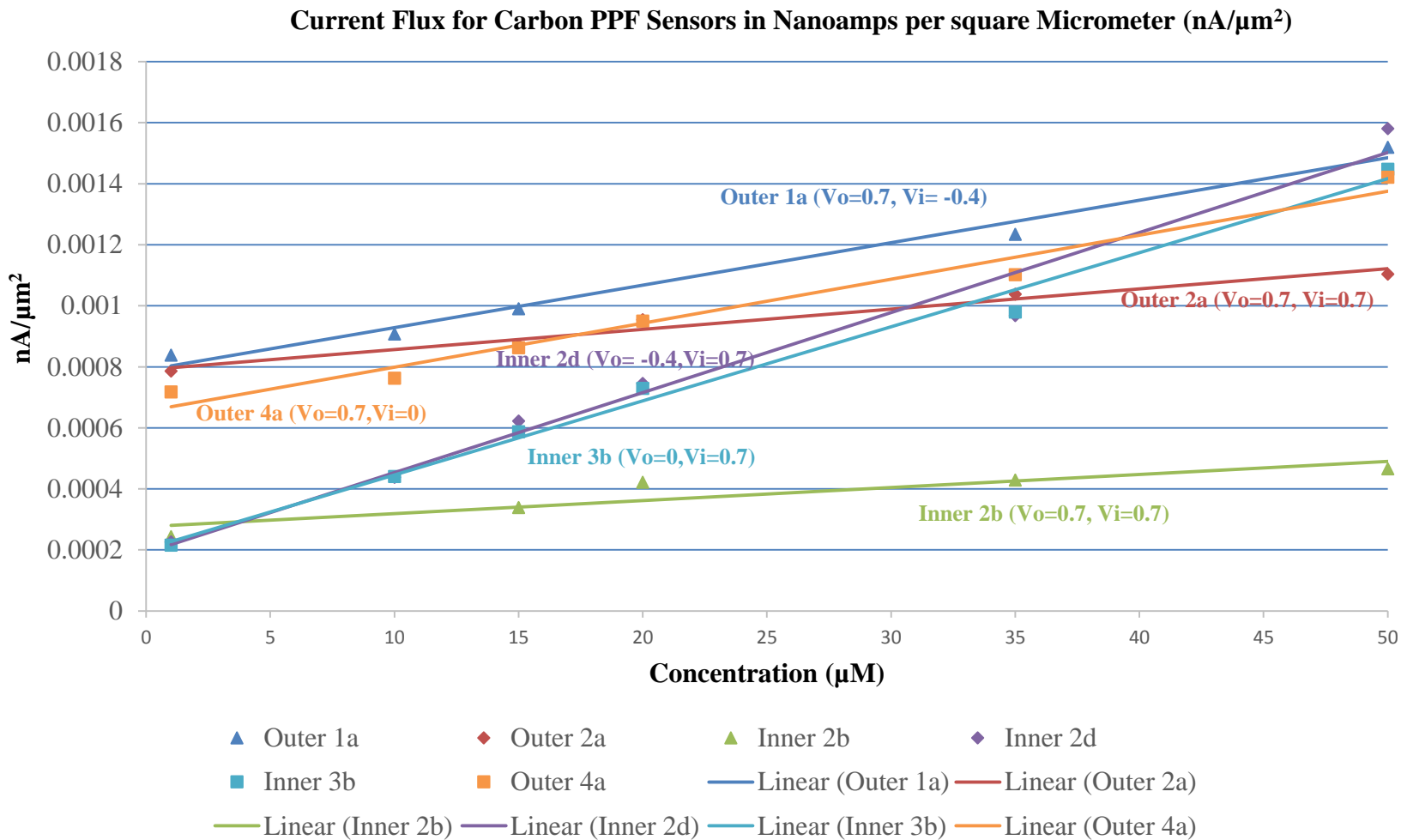


Figure 61: Carbon PPF electrical current per unit area ($\text{nA}/\mu\text{m}^2$) with linear regression lines. “Outer” and “inner” refer to the outer and inner electrodes respectively and followed by the testing scenario.

The current flux rates of Figure 61 were plotted in Figure 62. Inner electrode Scenarios 2d and 3b had similar electric current flux rates, and were overall the highest rate of current flux. This is most likely due to the outer electrode not competing with the inner electrode for dopamine.

The outer electrode Scenarios 4a and 1a were also similar to each other and were the next highest rates of current flux. Here the outer electrode was not competing with the inner electrode for local dopamine.

When the inner electrode had competition from the outer electrode was, as in Scenario 2b, the current flux rate of the inner electrode fell from Scenario 2d and 3b's approximate rate of 2.5×10^{-5} nA/ μm^2 to Scenario 2b's rate of 4.3×10^{-6} (nA/ μm^2)/ μM , an 83% decrease.

For the outer electrode, non-competition was for Scenarios 1a and 4a, while competition occurred in Scenario 2a. For these cases, the electric current flux rate of the outer electrode went from approximately 1.4×10^{-5} nA/ μm^2 to the lower value of 6.6×10^{-6} (nA/ μm^2)/ μM , respectively. This signified a 53% reduction in the electrical current flux rate.

A comparison of electrical flux rate between platinum and carbon PPF sensors can be seen in Table 14.

The large size of the outer electrode again reduced the inner electrode's current flux more when it competed with the inner electrode than when the inner electrode interfered with the outer electrode's dopamine oxidation. The shielding effect remains consistent.

Shielding, or competition, between electrodes is apparently greater when the inner electrode is being affected by the outer electrode, because the outer is bigger, has double the surface area and flanks the smaller inner electrode on 2 sides.

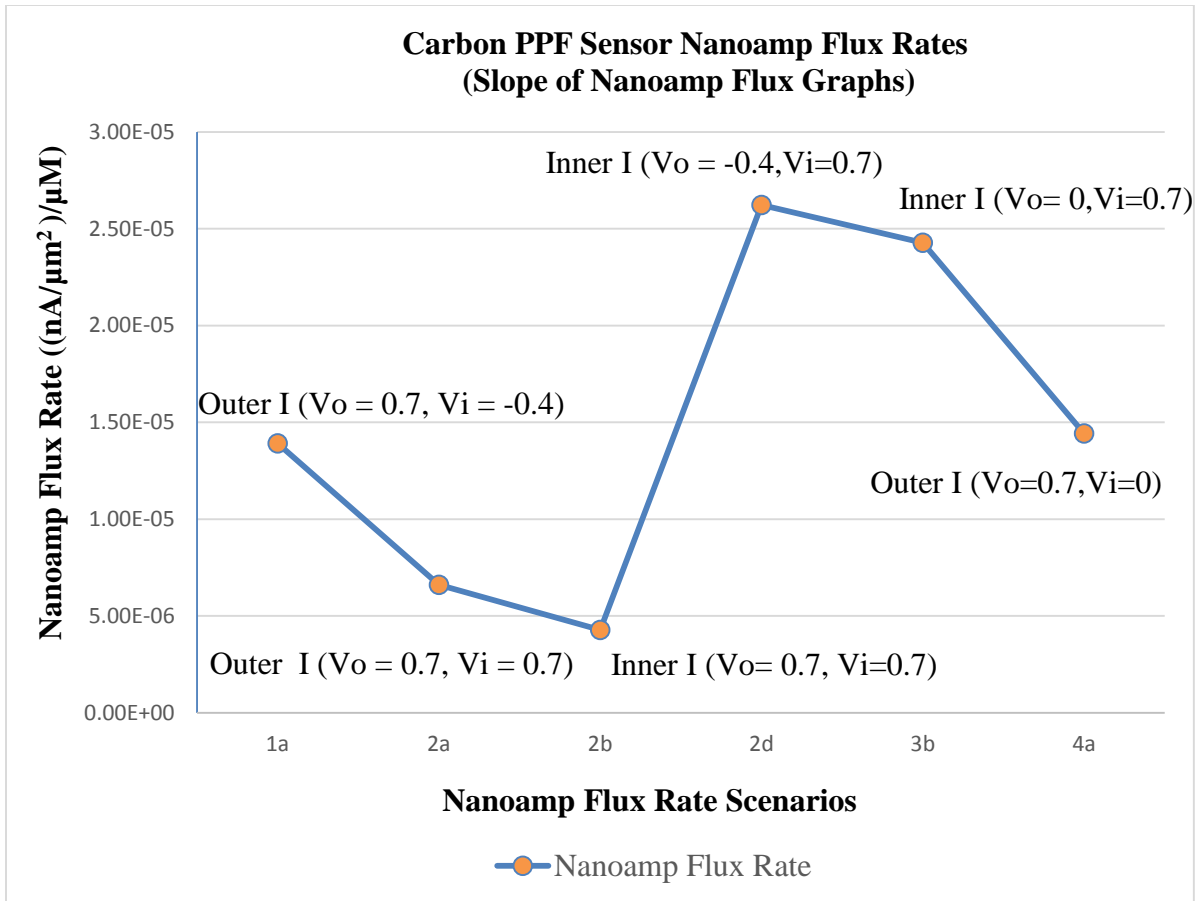


Figure 62: Carbon PPF Sensor Nanoamp Flux Rates per testing Scenario.

3.8 Carbon PPF Sensor Electrode Cottrell Equation Relation

As with the platinum sensors in section 3.4, it was found the carbon PPF sensors do not produce a current that can be strictly predicted from the Cottrell equation as given in (11). Instead, the carbon PPF sensor current can be approximated by applying a multiplying coefficient to the Cottrell equation. This coefficient, S , is proportional to the inverse square root of the concentration, C , multiplied by a constant, a , and added to a constant displacement value, b , as show in (12).

Figure 63 shows how the carbon PPF sensor Scenario 1a results are fitted to the function seen in (13), as well as exponential equations of form (13) and (14), to

approximate the times larger the current measurement is compared to that predicted by the Cottrell equation.

Scenario 1a was examining the outer electrode current when the outer electrode was oxidizing dopamine and the inner electrode was held at a reduction potential.

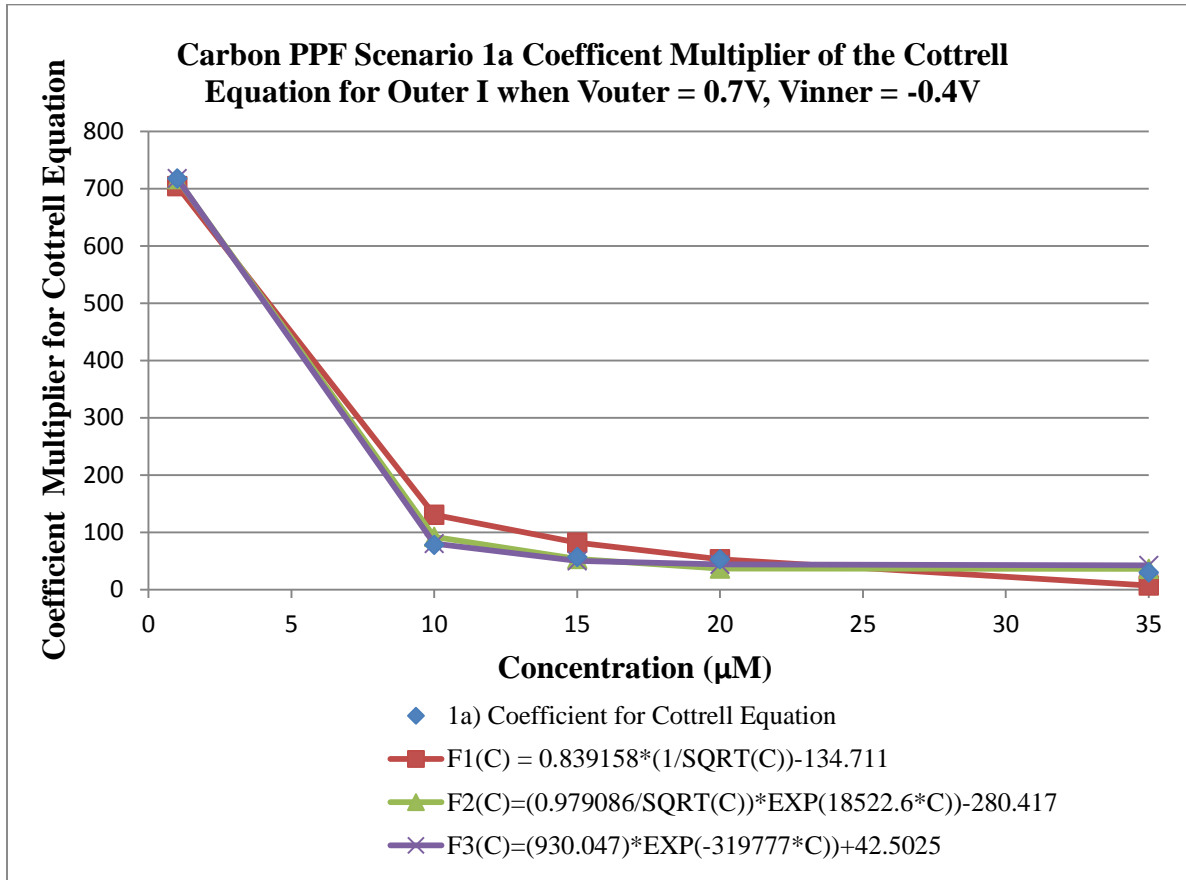


Figure 63: The carbon PPF sensor Scenario 1a coefficient multiplier of the Cottrell Equation for the outer electrode current when $V_{outer} = 0.7V$ and $V_{inner} = -0.4V$. Scenario 1a was examining the outer electrode current when the outer electrode was oxidizing dopamine and the inner electrode was held at a reduction potential. The blue diamond markers are the measured multiplier coefficients for the Cottrell equation derived from dividing the measured current by the expected Cottrell equation prediction. The red box line, $F1(C)$, is an equation matching the blue line of the form given by (8). $F2(C)$ is an equation of form (13), while $F3(C)$ is an exponential based expression of the type seen in equation (14). The R-squared value for $F1(C)$ is 0.987, $F2(C)$ is 0.9986 and $F3(C)$ is 0.9992.

Figure 64, shows how the Scenario 2a results were also more than what the Cottrell equation predicts, and that the measured currents are larger by a multiplier given by equation (8) and exponential type equations of form (13) and (14). Scenario 2a was examining the outer electrode current when both the inner and outer electrode were oxidizing dopamine.

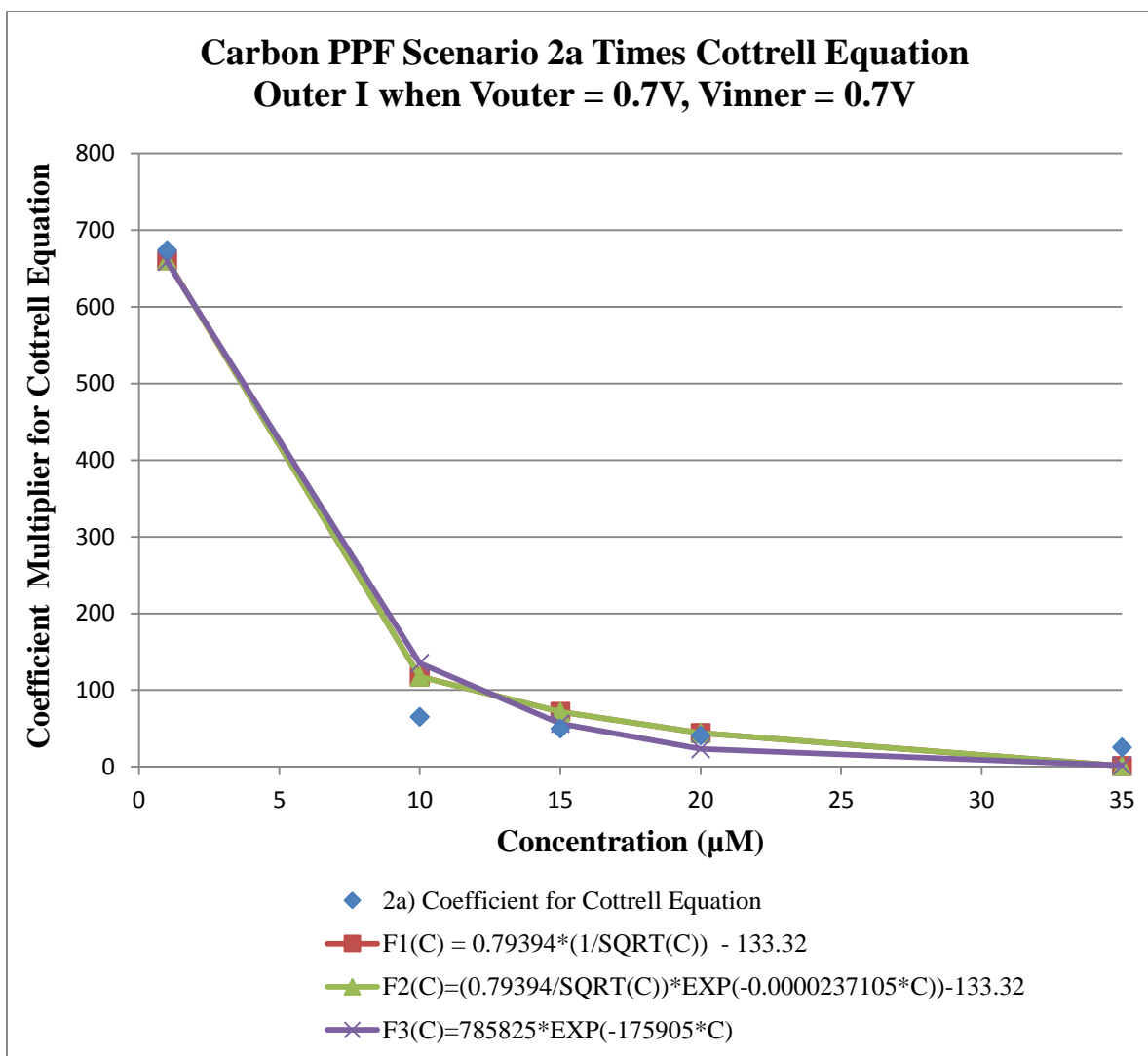


Figure 64: The carbon PPF sensor Scenario 2a coefficient multiplier of the Cottrell Equation for the outer electrode current when $V_{outer} = 0.7V$ and $V_{inner} = 0.7V$. Scenario 2a was examining the outer electrode current when both the inner and outer electrode were oxidizing dopamine. The blue diamond markers are the measured multiplier coefficients for the Cottrell equation derived from dividing the measured current by the expected Cottrell equation prediction. The red box line, $F1(C)$, is an equation matching the blue line of the form given by (8). $F2(C)$ is an equation of form (13), while $F3(C)$ is an exponential based expression of the type seen in equation (14). The R-squared value for $F1(C)$ is 0.9873, $F2(C)$ is 1 and $F3(C)$ is 0.9967.

Figure 65, below, shows how the Scenario 2b results followed the trend and were also more than what the Cottrell equation predicts by itself. The multiplier adjustments of

the Cottrell equation based upon exponential type equations, as well as the function of type (14), are shown in Figure 65 as well as exponential type equations of form (13) and (14). Scenario 2b was examining the inner electrode current when both the inner and outer electrode were oxidizing dopamine.

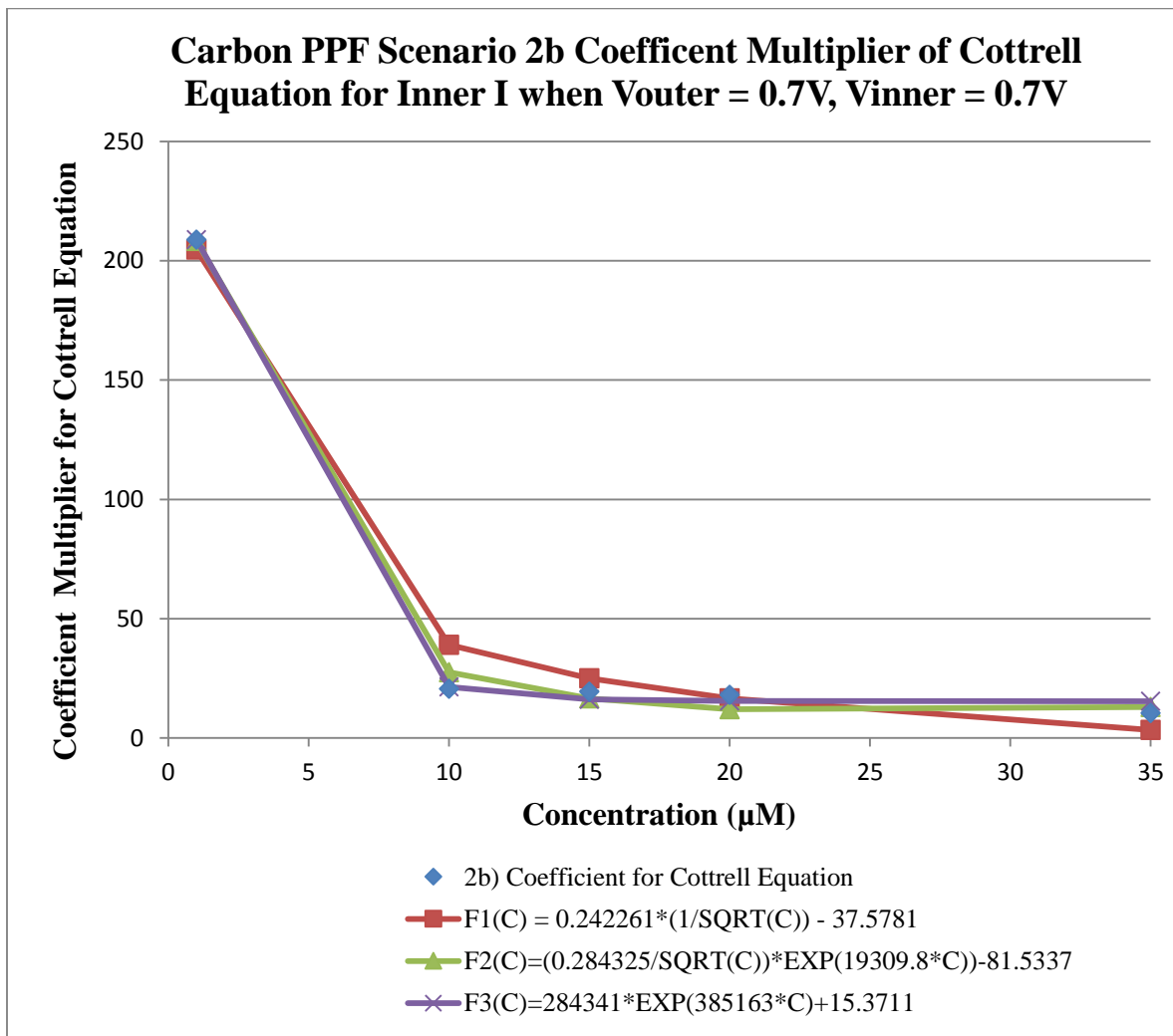


Figure 65: The carbon PPF sensor Scenario 2b coefficient multiplier of the Cottrell Equation for the inner electrode current when $V_{outer} = 0.7V$ and $V_{inner} = 0.7V$. The blue diamond markers are the measured multiplier coefficients for the Cottrell equation derived from dividing the measured current by the expected Cottrell equation prediction. The red box line, $F1(C)$, is an equation matching the blue line of the form given by (8). $F2(C)$ is an equation of form (13), while $F3(C)$ is an exponential based expression of the type seen in equation (14). The R-squared value for $F1(C)$ is 0.9851, $F2(C)$ is 0.9966 and $F3(C)$ is 0.9986.

The Scenario 2d results are shown in Figure 66, and in line with previous results being larger than the Cottrell equation predictions. As before, the measured current is divided by the expected Cottrell value to yield the dimensionless multiplier fitted to an equation of the form found in (8) as well as two exponential variants of form (13) and (14). Scenario 2d was examining the inner electrode current when both the inner and outer electrode were oxidizing dopamine.

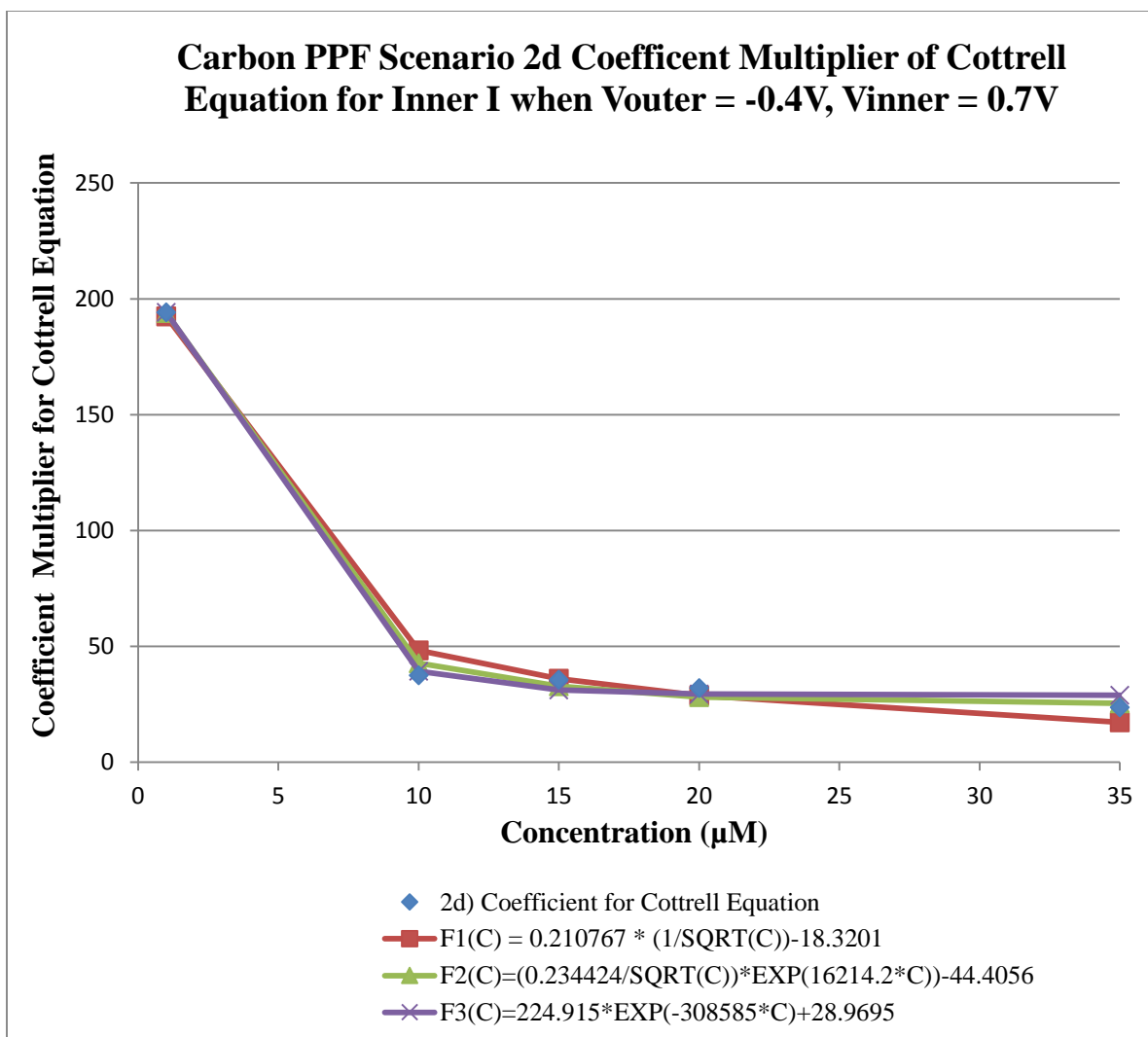


Figure 66: The carbon PPF sensor Scenario 2d coefficient multiplier of the Cottrell Equation for the inner electrode current when $V_{outer} = -0.4V$ and $V_{inner} = 0.7V$. The blue diamond markers are the measured multiplier coefficients for the Cottrell equation derived from dividing the measured current by the expected Cottrell equation prediction. The red box line, $F1(C)$, is an equation matching the blue line of the form given by (8). $F2(C)$ is an equation of form (13), while $F3(C)$ is an exponential based expression of the type seen in equation (14). The R-squared value for $F1(C)$ is 0.9919, $F2(C)$ is 0.9975 and $F3(C)$ is 0.9973.

Figure 67 shows how the Scenario 3b results were also more than what the Cottrell equation predicts, and that the measured currents are larger by a multiplier given by equation (8) and the exponential equations of form (13) and (14). Scenario 3b was examining the

inner electrode current when the inner electrode was oxidizing dopamine and outer electrode was set at a 0V potential.

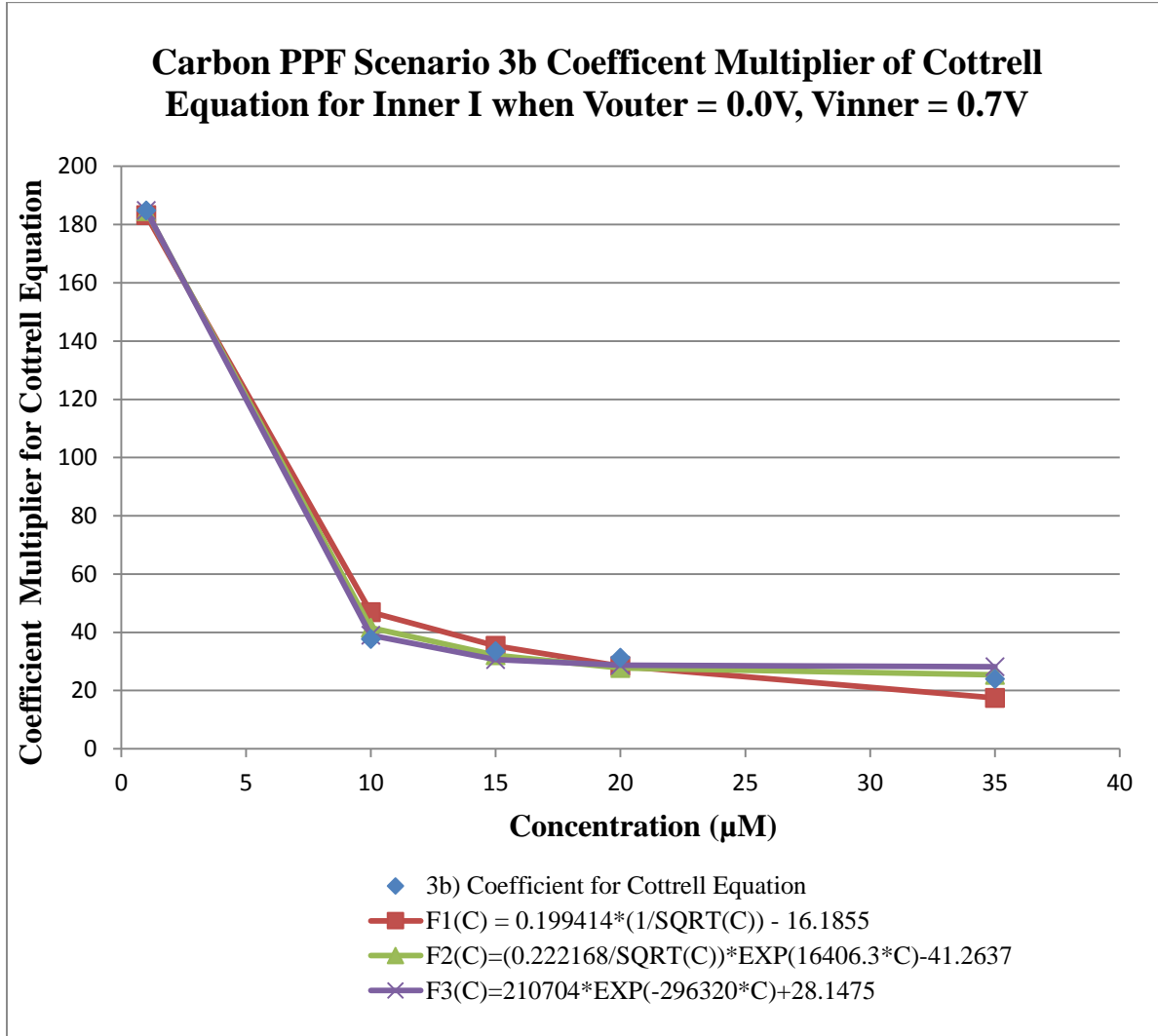


Figure 67: The carbon PPF sensor Scenario 3b coefficient multiplier of the Cottrell Equation for the inner electrode current when $V_{outer} = 0.7V$ and $V_{inner} = 0.0V$. The blue diamond markers are the measured multiplier coefficients for the Cottrell equation derived from dividing the measured current by the expected Cottrell equation prediction. The red box line, $F1(C)$, is an equation matching the blue line of the form given by (8). $F2(C)$ is an equation of form (13), while $F3(C)$ is an exponential based expression of the type seen in equation (14). The R-squared value for $F1(C)$ is 0.991, $F2(C)$ is 0.9984 and $F3(C)$ is 0.9982.

With Figure 68 below, the pattern continues of the measured currents being larger than predicted Cottrell values. As done earlier, the measured currents were divided by the expected value and the multiplier curve result was matched to equation (8) and two exponential equation variants of form (13) and (14). Scenario 4a was examining the outer electrode current when the outer electrode was oxidizing dopamine and inner electrode was set at a 0V potential.

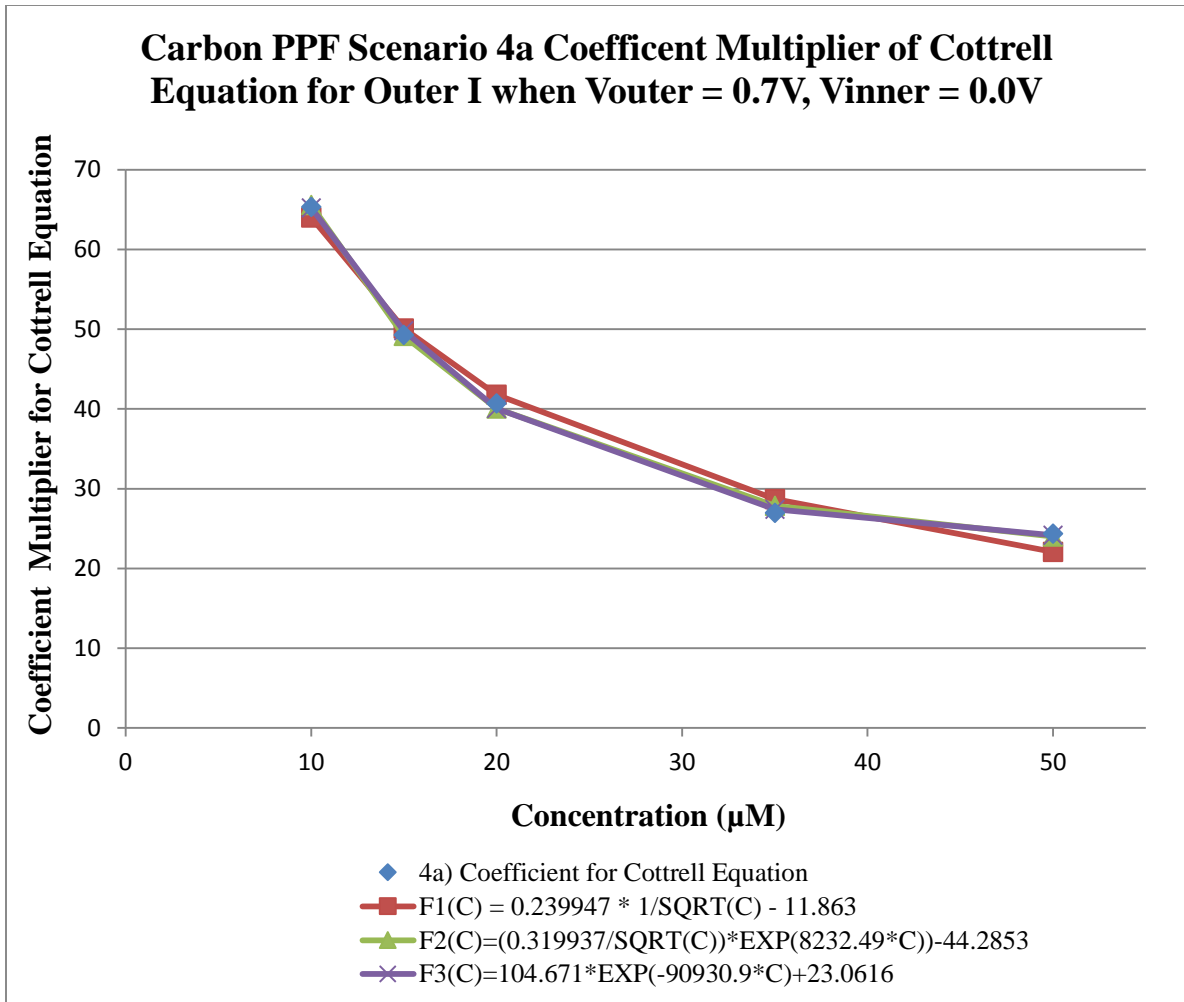


Figure 68: The carbon PPF sensor Scenario 4a coefficient multiplier of the Cottrell Equation for the outer electrode current when $V_{outer} = 0.7V$ and $V_{inner} = 0.0V$. The blue diamond markers are the measured multiplier coefficients for the Cottrell equation derived from dividing the measured current by the expected Cottrell equation prediction. The red box line is an equation matching the blue line of the form given by (8). $F2(C)$ is an equation of form (13), while $F3(C)$ is an exponential based expression of the type seen in equation (14). The R-squared value for $F1(C)$ is 0.9896, $F2(C)$ is 0.9988 and $F3(C)$ is 0.9992.

The next figure takes all the carbon PPF measured multiplier data and puts them together on a single graph. Two groupings are immediately apparent. These correspond to the outer and inner electrode of the sensor, showing there is a consistency to the effect.

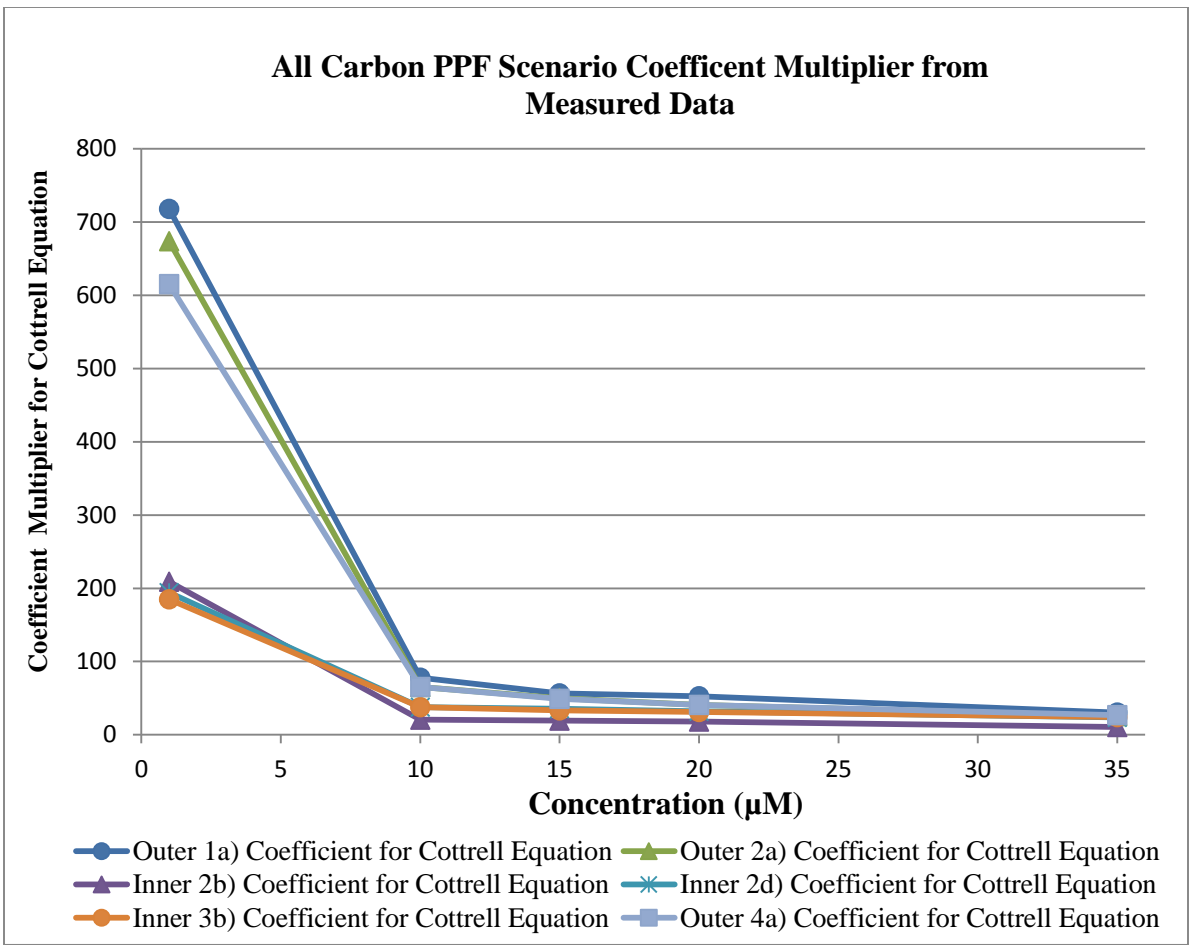


Figure 69: All measured carbon PPF sensor measured multiplier values together. These curves represent the blue lines in the previous 6 graphs where the measured current was divided by the expected Cottrell equation expectation. The two groupings correspond to the outer and inner electrode responses. A similar plot was done for the platinum sensors, in Figure 49.

3.9 Comparison of Platinum versus Carbon PPF Sensors

3.9a Electrode Oxidative Response Comparison

There was a challenge in finding a way to compare the platinum and carbon PPF sensors because the offset for the carbon PPF could not easily be removed. A way in which the two different kinds of sensors could be related was to look at the slopes or rates of the

oxidation for the sensors as these did not depend on the offset. This method compared the oxidative response sensitivity of the sensors to the dopamine concentrations in units of nA/ μ M. Table 12 shows the nanoamps per micromolar (nA/ μ M) rates for each sensor type with the right most column indicating the percentage change of carbon PPF versus the platinum sensor.

Table 12: Comparing Platinum and Carbon PPF Sensor Oxidative Rates					
Scenario	Description	Current being measured & electrode potentials	Platinum (nA/μM)	Carbon PPF (nA/μM)	Percentage Change: Carbon PPF vs Platinum
1a	Outer oxidizing potential, inner reducing potential	Outer I ($V_o = 0.7V$, $V_i = -0.4V$)	5.2×10^{-2}	5.8×10^{-2}	+12%
2a	Outer electrode competing with inner electrode	Outer I ($V_o = 0.7V$, $V_i = 0.7V$)	3.4×10^{-2}	2.7×10^{-2}	-21%
2b	Inner electrode competing with outer electrode	Inner I ($V_o = 0.7V$, $V_i = 0.7V$)	7.5×10^{-3}	4.9×10^{-3}	-35%
2d	Inner oxidizing potential, outer reducing potential, no competing	Inner I ($V_o = -0.4V$, $V_i = 0.7V$)	2.3×10^{-2}	3×10^{-2}	+30%
3b	Inner oxidizing potential, outer zero potential, no reducing, no competing	Inner I ($V_o = 0V$, $V_i = 0.7V$)	2.4×10^{-2}	2.7×10^{-2}	+13%
4a	Outer oxidizing potential, inner zero potential, no reducing, no competing	Outer I ($V_o = 0.7V$, $V_i = 0V$)	5.2×10^{-2}	6×10^{-2}	+15%

In Table 12 it can be seen how the carbon PPF sensors behaved with a greater responsiveness than the platinum sensor of similar design for oxidizing dopamine (Scenarios 1a, 2d, 3b and 4a) when the opposite electrode was at a reduction potential or when the opposite electrode was not competing for dopamine. When the two electrodes competed with one another, there was shielding effect that made the carbon PPF have less response sensitivity than the platinum sensor. Another interpretation is that the characteristics that make the carbon PPF sensors respond more vigorously than the platinum sensors, as in Scenarios 1a, 2d, 3b and 4a, are also responsible for the stronger competition interference between electrodes than seen in the platinum sensors (Scenarios 2a and 2b).

Evidence for some redox cycling signal strengthening can also be seen in Table 12 when comparing the inner electrode in the carbon PPF 3b test scenario to the 2d test scenario.

The Table 12 comparisons have examined the oxidative current response of the sensor on an entire electrode basis. Table 13 and Table 14 in the following sections examine the sensors on a per unit area comparisons.

3.9b Electrode Mass Transport

The mass transport flux characteristics for the platinum and carbon PPF sensor were compared in a similar way as the oxidative reactivity by examining the rates of mass transport flux. The slopes of the graphs (Figure 41 and Figure 59) in this case gave the mass transport flux responsivity in units of nanomoles per square micrometer per micromolar ($(\text{nM}/\mu\text{m}^2)/\mu\text{M}$). Table 13 shows the $(\text{nM}/\mu\text{m}^2)/\mu\text{M}$ for each sensor type with the right most column indicating the percentage change of carbon PPF versus the platinum sensor.

Scenario	Description	Current being Measured & Electrode Potentials	Platinum ((nM/μm²)/μM)	Carbon PPF ((nM/μm²)/μM)	Percent Change: Carbon PPF vs Platinum
1a	Outer oxidizing potential, inner reducing potential	Outer I (V _o = 0.7V, V _i = -0.4V)	8.8x10 ⁻¹¹	7.2 x10 ⁻¹¹	-18%
2a	Outer electrode competing with inner electrode	Outer I (V _o = 0.7V, V _i = 0.7V)	6.7 x10 ⁻¹¹	3.4 x10 ⁻¹¹	-49%
2b	Inner electrode competing with outer electrode	Inner I (V _o = 0.7V, V _i =0.7V)	3.7x10 ⁻¹¹	2.5x10 ⁻¹¹	-32%
2d	Inner oxidizing potential, outer reducing potential	Inner I (V _o = -0.4V, V _i =0.7V)	1.2 x10 ⁻¹⁰	1.4 x10 ⁻¹⁰	+17%
3b	Inner oxidizing potential, outer zero potential, no reducing, no competing	Inner I (V _o = 0V, V _i = 0.7V)	1.2 x10 ⁻¹⁰	1.3 x10 ⁻¹⁰	+8%
4a	Outer oxidizing potential, inner zero potential, no reducing, no competing	Outer I (V _o = 0.7V, V _i = 0V)	9.1 x10 ⁻¹¹	7.5 x10 ⁻¹¹	-18%

As Table 13 shows, the per unit area flux examination indicates the carbon PPF sensor has a lower mass transport flux responsivity than the platinum sensor of similar design (Scenarios 1a, 2a, 2b and 4a). This result is most likely due to the carbon PPF sensor having

a slightly larger outer electrode surface area of $4,160 \mu\text{m}^2$ versus the average outer electrode surface size of the platinum outer electrode of $3,000 \mu\text{m}^2$. The larger surface area distributes the mass transport flux over more surface meaning there is less mass transport per unit area.

The inner electrode of the carbon PPF sensor had a higher mass transport flux than the platinum inner electrode for Scenario 2d and 3b. For both these cases the inner electrodes were not competing with the outer electrode. The carbon PPF and platinum inner electrodes have very similar inner electrode areas of $1,080 \mu\text{m}^2$ and $1,000 \mu\text{m}^2$, respectively. The higher mass transport flux with the carbon PPF inner electrode may be due to the sensor having a vertical component off the substrate. As mentioned before, this vertical component helps to form a channel, bolstering the possibility for redox cycling. This can explain why the carbon PPF Scenario 2d has a higher response than the platinum sensor for the same testing scenario.

3.9c Electrode Current Flux

The electrode current flux characteristics for the platinum and carbon PPF sensor were also compared in a similar way as the oxidative response and mass transport flux by examining the rates of electrode current flux per unit area. The slopes of the graphs in this case gave the electrode current flux response sensitivity in units of nanoamps per square micrometer per micromolar ($(\text{nA}/\mu\text{m}^2)/\mu\text{M}$). Table 13 shows the $(\text{nA}/\mu\text{m}^2)/\mu\text{M}$ for each sensor type with the right most column indicating the percentage change of carbon PPF versus the platinum sensor.

Table 14: Comparing Platinum and Carbon PPF Sensor Nanoamp Flux Rates					
Scenario	Description	Current being Measured & Electrode Potentials	Platinum ((nA/μm²)/μM)	Carbon PPF ((nA/μm²)/μM)	Percent Change: Carbon PPF vs Platinum
1a	Outer oxidizing potential, inner reducing potential	Outer I (V _o = 0.7V, V _i = -0.4V)	1.7x10 ⁻⁵	1.4x10 ⁻⁵	-18%
2a	Outer electrode competing with inner electrode	Outer I (V _o = 0.7V, V _i = 0.7V)	1.3x10 ⁻⁵	6.6 x10 ⁻⁶	-49%
2b	Inner electrode competing with outer electrode	Inner I (V _o = 0.7V, V _i =0.7V)	7.1 x10 ⁻⁶	4.3 x10 ⁻⁶	-39%
2d	Inner oxidizing potential, outer reducing potential	Inner I (V _o = -0.4V, V _i = 0.7V)	2.3 x10 ⁻⁵	2.6 x10 ⁻⁵	+13%
3b	Inner oxidizing potential, outer zero potential, no reducing, no competing	Inner I (V _o = 0V, V _i =0.7V)	2.3 x10 ⁻⁵	2.4 x10 ⁻⁵	+4%
4a	Outer oxidizing potential, inner zero potential, no reducing, no competing	Outer I (V _o = 0.7V, V _i = 0V)	1.8 x10 ⁻⁵	1.4 x10 ⁻⁵	-22%

The results of Table 14 show the current flux rate indicates the carbon PPF sensor has lower electrode current flux responsivity than the platinum sensor of similar design for most of the test cases (Scenarios 1a, 2a, 2b and 4a). A similar trend was seen in the previous

section with mass transport flux. This decrease is likely due to the electrode surface area as seen in the mass transport section. To be clear, the slightly larger carbon PPF outer electrode surface area of $4,160 \mu\text{m}^2$ versus the average $3,000 \mu\text{m}^2$ outer electrode surface size of the platinum translates to less current per unit area.

In the noncompeting testing Scenarios 2d and 3b, the inner electrode of the carbon PPF sensor had a higher flux than the platinum inner electrode. As before with the mass transport flux, the carbon PPF inner electrode has $1,080 \mu\text{m}^2$ surface area, while the platinum inner electrode has $1,000 \mu\text{m}^2$ surface area. With such similar surface area values, the explanation of why the carbon PPF inner electrode current flux is higher than the platinum sensor, could stem from the physical differences between the sensors. The carbon PPF has a vertical component off the substrate, which helps make a channel where redox cycling can enhance the signal as possibly occurring in Scenario 2d.

The vertical dimension also means the sensors interact with the dopamine solution on 3 surfaces instead of 1 surface as with the platinum sensor. The additional two-dimensional diffusion may provide a greater mass transport of dopamine to the surface, yielding a higher electrode current flux.

3.9d Carbon PPF and platinum sensor electrode Cottrell Equation relation

In previous sections where the Cottrell equation was applied to the platinum sensor and carbon PPF, it was observed that the Cottrell equation did not accurately predict the measured current. Instead the equation needed a modification in terms of a coefficient. The type of coefficient the formula needed is detailed in the Table 15 below.

**Table 15: Characteristic Platinum and Carbon PPF Cottrell Equation
Multiplier Coefficient, S, Summary**

Scenario	Description	Current being Measured & Electrode Potentials	Platinum Sensor Coefficient	Carbon PPF Sensor Coefficient
1a	Outer oxidizing potential, inner reducing potential	Outer I ($V_o = 0.7V$, $V_i = -0.4V$)	Constant Coefficient (see Table 7)	Debye-like Function Coefficient (see Figure 63)
2a	Outer electrode competing with inner electrode	Outer I ($V_o = 0.7V$, $V_i = 0.7V$)	Constant Coefficient (see Table 7)	Debye-like Function Coefficient (see Figure 64)
2b	Inner electrode competing with outer electrode	Inner I ($V_o = 0.7V$, $V_i = 0.7V$)	Constant Coefficient (see Table 7)	Debye-like Function Coefficient (see Figure 65)
2d	Inner oxidizing potential, outer reducing potential	Inner I ($V_o = -0.4V$, $V_i = 0.7V$)	Constant Coefficient (see Table 7)	Debye-like Function Coefficient (see Figure 66)
3b	Inner oxidizing potential, outer zero potential, no reducing, no competing	Inner I ($V_o = 0V$, $V_i = 0.7V$)	Debye-like Function Coefficient (see Figure 47)	Debye-like Function Coefficient (see Figure 67)
4a	Outer oxidizing potential, inner zero potential, no reducing, no competing	Outer I ($V_o = 0.7V$, $V_i = 0V$)	Debye-like Function Coefficient (see Figure 48)	Debye-like Function Coefficient (see Figure 68)

Chapter 4 Conclusions

The focus of this work was the chronoamperometric study of microscale platinum and carbon pyrolyzed photoresist film sensors of similar design to electrochemically detect dopamine in solution. Using potentiometric step methods, the inner and outer electrodes of each sensor types were probed for dopamine detection ability as well as interaction with each other under different operating parameters.

To start the work, the supporting physical electronics hardware was constructed. This was needed to set voltage potentials on the sensors, amplify and measure the nanoamp sized currents. Software for controlling the hardware, data acquisition, equilibrating the sensors, automating the testing protocols and data processing was then locally programmed. Together, the electronics hardware and software stepped the sensors through a routine of testing scenarios.

Fouling issues prevented the initials stages of this work. Solvents and acid cleaning removed the deposited material, however the sensors would quickly foul again upon usage. A way to clean the electrodes, in a repeatable and consistent way, was developed by cycling a series of potentials which restored sensor sensitivity. The method was utilized to clean the sensors prior to every set of testing.

For oxidative dopamine testing, the platinum and carbon PPF sensors had a current response that was linearly dependent on the concentration of dopamine. Based on the rate of dopamine oxidation, the carbon PPF sensors had a higher responsivity than the platinum sensors for both inner and outer electrodes. Both sensor types had electrode competition and shielding when the opposing electrode was actively oxidizing dopamine. When the opposite electrode was either at a zero or reduction potential, competition was not observed. There was a large interference between the inner and outer electrodes for carbon PPF versus the platinum sensors. This was most likely due to the higher responsivity of the carbon PPF sensors also causing larger responses in shielding or competition. The physical difference of the carbon PPF having a channel between the electrodes probably also contributed because the channel creates a small volume of solution from which dopamine can get depleted by two

actively oxidizing potential electrodes. In contrast, the platinum electrodes were planar to the surface of the silicon substrate and did not have a channel.

In the reduction testing, the platinum sensor did not register any chemical reduction activity on the smaller inner electrode. On the larger outer electrode, the platinum sensor showed reduction detection ability to a certain limit. The response was linear until about 20 μM whereupon it plateaued and remained steady for the remaining higher concentrations. This suggests that the maximum generation of dopamine-o-quinone from the inner electrode, to be detected on the outer electrode, had been attained. A combination of the diffusion limited aspect of the reaction and the physical size of the inner electrode is most likely responsible for this behavior.

As for the carbon PPF sensor, it had chemical reduction detection abilities on both the inner and outer electrode. This may have been possible for the carbon PPF sensor instead of the platinum sensor because the carbon PPF sensor had a geometry that created a channel between the electrodes. Any created dopamine-o-quinone would have a high likelihood of diffusing from the surface of the channel orthogonally in the direction of the electrode. In comparing the individual electrodes, the outer electrode exhibited about twice the reduction response of the inner electrode. This was probably due to its physical characteristics of being twice as large as the inner electrode. The greater surface area could react with more of the produced dopamine-o-quinone.

The carbon PPF sensor also exhibited some enhancement with redox cycling when the inner electrode was set to the oxidizing potential and the outer electrodes were at a reduction potential.

The mass transport analysis showed that the mass transport flux for the platinum sensor was higher for the inner electrode at oxidizing potentials than the outer electrode. With the carbon PPF sensor, there was the issue of the remaining background current presence which offset the flux values for this kind of sensor. However, the similarity of construction between the carbon PPF and platinum sensors, as well as the similarity of responsivity, gave an indication that the carbon PPF electrode followed the same trend as the platinum sensors. The tendency for both was that the inner electrode experienced a higher

per unit area mass transport than the large electrode because of the area differences between the two electrodes.

The electrode current flux analysis for the platinum and carbon PPF sensors were comparable to the mass transport flux analysis. The inner electrodes experienced a higher rate of flux than the outer electrode due to the smaller area of the electrode.

The Cottrell analysis of the electrodes showed a response that was not directly predictable by the Cottrell equation. However, when the measured electrical current response was compared to the predicted response, a pattern emerged. The recurring result was a multiplying factor that could be applied to the Cottrell equation to yield the measured current. The multiplier equation could be characterized by an inverse square root of the concentration function or an exponential function. Both of these kinds of equations have a form that has also been used to describe the electric double layer width around an electrode as a function of concentration. Consequently, the proposed mechanism in action is thought to be the electrode interacting with a volume or zone of dopamine solution of a Debye or Debye-like length scale from the electrode by means of an electron tunneling current. Or in other words, the electron tunneling is moderated by the electric double layer. A number of elements support this conclusion. The first is that in a 7.4 pH solution, dopamine carries a positive charge. Adding a charged molecule to a solution is known to change the Debye length. With each higher concentration of dopamine experiment, more charge was introduced to the solution. Second, there has been work where tunneling was observed in proteins and ammonia. Dopamine has the same atom constituents as proteins and has an amine group at its terminus that resembles ammonia. Third, the electrode surface is known to have structured water due to the dipole interaction of water with the charge on the electrode surface and the charge of the specifically and non-specifically adsorbed ions. In work where water is sterically constrained, electron tunneling has been described. Together, these factors may contribute to the Debye-like multiplier modulation of the Cottrell predicted current. A possible explanation for noticing this effect is due to the small areas, small currents and sparse dopamine concentration used. At larger values for these variables, the

measured currents probably converge with the Cottrell equation predictions, as the curves seem to already indicate by beginning to become more horizontal with increasing dopamine concentrations.

The Debye-like multiplying effect of the Cottrell equation was noticed in 2 of the testing scenarios for the platinum sensors and all of the testing cases for carbon PPF sensors. For the remaining four platinum testing scenarios, a constant multiplier could be used to describe the resulting electrical current. The platinum sensors did function with a Debye-like modulated current when one electrode was oxidizing dopamine while the other was at a zero potential. The carbon PPF sensors did not have this limitation based upon voltages.

Chapter 5 Future Work

There are several different ways this work can be expanded and furthered. The following are descriptions of some possibilities.

- Increase the number of interdigitated electrode to enhance signal strength.
- Increase the height to width ratio between electrodes to enhance steady-state redox currents as observed in other work [41][129][130].
- Bubble nitrogen through the water to reduce any pH change effects.
- Give the existing sensor a partial covering over a portion of the sensor window to improve redox cycling by preventing the dopamine-o-quinone from diffusing quickly into the bulk solution. The concept is shown in Figure 70.

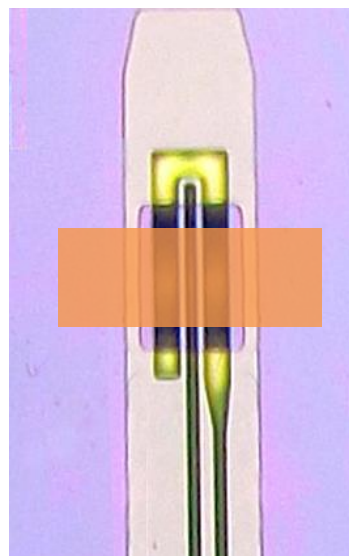


Figure 70: A possible future modification to the sensor could include a partial covering over the sensing region. This would still allow sensor contact with the dopamine solution through the uncovered areas, but would prevent dopamine-o-quinone from diffusing quickly away into the bulk solution. It should enhance the signal by strengthening the redox cycling effect.

Continuing with avenues of future development, the following could also be investigated:

- Create a way to directly measure and verify the Debye length changes which come from increasing concentrations of dopamine. For this the PBS concentration can be varied, as can the pH or the PBS could be switched for another buffer solution.
- Make a circuit, chemical and physics computer model for the sensors.
- Use the measured current to Cottrell equation relation to probe modified surfaces and compare surfaces where there are attached molecules, ligands, proteins, antibodies, DNA, aptamers and other substances. The method might be useful in probing surfaces used for creating capacitors as well.

- Use a scanning electrochemical potential microscope (SECPM) to measure the profile of the electric double layer and compare it to the differences seen with the measured and predicted currents.
- Develop the system to have wireless capabilities, similar to the WINCS (Wireless Instantaneous Neurotransmitter Concentration Sensing System) created at the Mayo Clinic [99][131]. This would free any in vivo study subjects being studied from being tethered to a cable.
- Place the transimpedance amplifier closer to the sensing region, perhaps even on the same piece of silicon in a miniaturized surface mount component to minimize external electrical noise.

REFERENCES

1. Ronkainen, Niina, H B. Halsall, and William R. Heineman. "Electrochemical Biosensors." *Chemical Society Reviews* 39, 1747-1763. 1 Feb. 2010.
2. Grieshaber, Dorothee, Robert MacKenzie, Janos Vörös, and Erik Reimhult. "Electrochemical Biosensors - Sensor Principles and Architectures." *Sensors* 8, 1400-1458. 23 Jan. 2008.
3. Eiggins, Brian. *Chemical Sensors and Biosensors*. England: John Wiley & Sons, 2004.
4. Yang, Xiaoyun, Jeffrey Kirsch, and Aleksandr Simonian. "Campylobacter Spp. Detection in the 21st Century: a Review of the Recent Achievements in Biosensor Development." *Journal of Microbiological Methods* 95 (2013): 48-56.
5. Wightman, R. Mark "Probing Cellular Chemistry in Biological Systems with Microelectrodes." *Science* 311 (2006): 1570-1574.
6. McCarty, Gregory, Matthew Zachek "Enhancing Electrochemical Detection by Scaling Solid State Nanogaps." *Journal of Electroanalytical Chemistry* 643 (2010): 9-14.
7. Wang, Hongwei, Qiaolin Lang, Liang Li, Bo Liang, Xiangjiang Tang, Lingrang Kong, Marco Mascini, and Aihua Liu. "Yeast Surface Displaying Glucose Oxidase as Whole-cell Biocatalyst: Construction, Characterization, and Its Electrochemical Glucose Sensing Application." *Analytical Chemistry* 85(2013): 6107-6112.
8. Patolsky, Fernando, Gengfeng Zheng, and Charles Lieber. "Nanowire Sensor for Medicine and the Life Sciences." *Nanomedicine* 1.1 (2006): 51-65.
9. Lieber, Charles, and Zhong Wang. "Functional Nanowires." *MRS Bulletin* 32.2 (2007): 99-108.
10. Lieber, Charles, and Zhong Wang. "Electrochemical Biosensors at the Nanoscale." *Lab on a Chip* 9 (2009): 2123-2131.
11. Patolsky, Fernando, Gengfeng Zheng, Oliver Hayden, Melike Lakadamyali, Xiaowei Zhuang, and Charles Lieber. "Electrical Detection of Single Viruses." *PNAS* 101.39 (2004): 14017-14022.

12. Engel, Yoni, Roey Elnathan, Alexander Pevzner, Guy Davidi, Eli Flaxer, and Fernando Patolsky. "Supersensitive Detection of Explosives by Silicon Nanowire Arrays." *Angewandte Chemie International Edition* 49.38 (2010): 6830-6835. 16 Sept. 2010.
13. Jain, Ankit, Pradeep Nair, and M A. Alam. "Flexure-FET Biosensor to Break Fundamental Sensitivity Limits of Nanobiosensors Using Nonlinear Electromechanical Coupling." *PNAS* 109.24 (2012): 9304-9308.
14. Rajan, Nitin, Xuexin Duan, and Mark A. Reed. "Performance Limitations for Nanowire/Nanoribbon Biosensors." *WIREs Nanomedicine and Nanobiotechnology* 5(2013): 629-645.
15. Wang, Joseph. "Chapter 6, Electrochemical Sensors." *Analytical Chemistry*. Hoboken, NJ: John Wiley & Sons, Inc, 2006. 201-234. Web.
16. Arugula, Mary, and Aleksandr Simonian. "Novel Trends in Affinity Biosensors: Current Challenges and Perspectives." *Institute of Physics (IOP) Publishing - Measurement Science and Technology* 25(2014)
17. Liu, Yang, Erlan Ramanculov, and Alexander Revzin. "Aptamer-Based Electrochemical Biosensor for Interferon Gamma Detection." *Analytical Chemistry* 82.19 (2010): 8131-8136.
18. Li, Bor-Ran, Chiao-Chen Chen, U. R. Kumar, and Yit-Tsong Chen. "Advances in Nanowire Transistors for Biological Analysis and Cellular Investigation." *The Royal Society of Chemistry* 139 (2014): 1589-1608.
19. Pumera, Martin, Adriano Ambrosi, Alessandra Bonanni, Elaine Lay Khim Chng, and Hwee Ling Poh. "Graphene for Electrochemical Sensing and Biosensing." *Trends in Analytical Chemistry* 29.9 (2010): 954-965.
20. Bard, Allen J., and Larry R. Faulkner. *Electrochemical Methods. Fundamentals and Applications*. New York: John Wiley & Sons, Inc, 2000.
21. Ellen Bowden, Mary. *Chemistry Is Electric!* Philadelphia: Chemical Heritage Foundation, Publication 15, 1997.
22. Bard, Allen J., and Royce W. Murray. "Electrochemistry." *PNAS* 109.29 (2012): 11484-11486.

23. Burns, William E. *Science in the Enlightenment: An Encyclopedia*. ABC-CLIO, 2003.
24. Zoski, Cynthia. *Handbook of Electrochemistry*. Amsterdam: Elsevier, 2007.
25. Bevilacqua, Fabio. "The Investigations and Inventions of Volta." *American Scientist* 91(2003): 560-563.
26. Madou, Marc. *Fundamentals of Microfabrication and Nanotechnology, Third Edition, Volume Two: Manufacturing Techniques for Microfabrication and Nanotechnology*. CRC Press, 2012.
27. Madou, Marc. *Fundamentals of Microfabrication and Nanotechnology, Third Edition, Volume Three: From MEMS to Bio-MEMS and Bio-NEMS: Manufacturing Techniques and Applications*. TYML. CRC Press, 2012.
28. Wanjun, Wang, and Steven A. Soper. *Bio-MEMS: Technologies and Applications*. CRC Press, 2006.
29. Deng, Xiao L., Tomohide Takami, Jong W. Son, Eun J. Kang, Tomoji Kawai, and Bae H. Park. "Effect of Concentration Gradient on Ionic Current Rectification in Polyethyleneimine Modified Glass Nano-pipettes." *Scientific Reports* 4.4005 (2014): 2875-2880.
30. Xiao, Yi, Rebecca Y. Lai, and Kevin W. Plaxco. "Preparation of Electrode-immobilized, Redox-modified Oligonucleotides for Electrochemical DNA and Aptamer-based Sensing." *Nature Protocols* 2.11 (2007): 2875-2880.
31. Ronkainen-Matsuno, Niina J., Jennifer H. Thomas, H B. Halsall, and William Heineman. "Electrochemical Immunoassay Moving into the Fast Lane." *Trends in Analytical Chemistry* 21.4 (2002): 213-225.
32. "Volta Before the First Consul". Courtesy of Library and Artifacts of the Bakken Museum. Permission for use obtained April 1, 2014. Volta demonstrating his battery, to be later called the voltaic pile, before First Consul Napoleon Bonaparte in November 1801 at the Institut de France in Paris. A colored engraving by Ducollet, after a painting by François Constant Mès , n.d. Count Alessandro Volta (1745-1827), Physicist. Self-taught citizen of northern Italian province of the Austrian empire [25]. 137

33. Richard, Kelly S. "Analytical Electrochemistry." *Analytical Electrochemistry*. Department Of Chemistry, East Stroudsburg University and Analytical Sciences Digital Library (ASDL), n.d. Web. http://www.asdlib.org/onlineArticles/ecourseware/Kelly_Potentiometry/PDF-6-Chronoamp.pdf, http://www.asdlib.org/onlineArticles/ecourseware/Kelly_Potentiometry/EC_CONCEPTS1.HTM, Creative Commons Access.
34. Clark, J J., and S G. Sandberg. "Chronic Microsensors for Longitudinal, Subsecond Dopamine Detection in Behaving Animals." *Nature Methods* (2010):126-129.
35. Jackowska, Krystyna, and Pawel Krysinski. "New Trends in Electrochemical Sensing of Dopamine." *Analytical and Bioanalytical Chemistry* 405.11 (2013): 3753-3771.
36. Vial, Laurent, and Pascal Dumy. "Artificial Enzyme-based Biosensors." *New Journal of Chemistry* 33(2009): 939-946.
37. ul Hasan, K, M H. Asif, O Nur, and M Willander. "Needle-Type Glucose Sensor Based on Functionalized Graphene." *Journal of Biosensors and Bioelectronics* 3:114 (2012). Open Access.
38. Permission granted April 4, 2014 by Research Corporation for Science Advancement.
39. "About Frederick Gardner Cottrell." *About Frederick Gardner Cottrell*. Research Corporation For Science Advancement, n.d. Web. 04 Apr. 2014. <<http://www.rescorp.org/about-rdsa/history/about-frederick-cottrell>>.
40. "Frederick Gardner Cottrell." *Frederick Gardner Cottrell*. Chemical Heritage Foundation, n.d. Web. 04 Apr. 2014. <<http://www.chemheritage.org/discover/online-resources/chemistry-in-history/themes/public-and-environmental-health/environmental-chemistry/cottrell.aspx>>.
41. Shim, Joon S., Michael J. Rust, and Chong H. Ahn. "A Large Area Nano-gap Interdigitated Electrode Array on a Polymer Substrate as a Disposable Nanobiosensor." *Journal of Micromechanical Microengineering* 23(2013): 1-6.
42. Chan, Feng-Lin, Wen-Ying Chang, Li-Min Kuo, Chih-Heng Lin, Shi-Wei Wang, Yuh-Shyong Yang, and Michael S-C Lu. "An Electrochemical Dopamine Sensor with a CMOS Detection Circuit." *Journal of Micromechanics and Microengineering* 18 (2008): 1-7.

43. Stern, Eric, Robin Wagner, Fred J. Sigworth, Ronald Breaker, Tarek M. Fahmy, and Mark A. Reed. "Importance of the Debye Screening Length on Nanowire Field Effect Transistor Sensors." *Nano Letters* 7.11 (2007): 3405-3409.
44. Dodo, Tara, Masao Sugawa, Eiji Nonaka, and Shun-chi Ikawa. "Submillimeter Spectroscopic Study of Concentrated Electrolyte Solutions as High Density Plasma." *AIP, The Journal of Chemical Physics* 116.113 (2002): 5701-5707.
45. Thorne, Kip, and Roger D. Blanford. "Chapter 19, Part V, Plasma Physics." *Modern Classical Physics: Optics, Fluids, Plasmas, Elasticity, Relativity, and Statistical Physics*. Princeton University Press, 2004. 6-8. Web. <www.pma.caltech.edu/Courses/ph136/yr2004/0419.1.K.pdf>.
46. Makowski, Matthew S., and Albena Ivanisevic. "Molecular Analysis of Blood with Micro-/Nanoscale Field-Effect-Transistor Biosensors." *Small* 7.14 (2011): 1863-1875.
47. Zhu, Xiaoshan, and Chong H. Ahn. "Electrochemical Determination of Reversible Redox Species at Interdigitated Array Micro/Nanoelectrodes Using Charge Injection Method." *IEEE Transactions on Nanobioscience* 4.2 (2005): 164-169.
48. Maehashi, Kenzo, and Kazuhiko Matsumoto. "Label-Free Electrical Detection Using Carbon Nanotube-Based Biosensors." *Sensors* 9 (2009): 5368-5378.
49. Wang, Hainan, and Laurent Pilon. "Accurate Simulations of Electric Double Layer Capacitance of Ultramicroelectrodes." *The Journal of Physical Chemistry C* 115 (2011): 16711-16719.
50. Leite, Fabio L., Carolina C. Bueno, Alessandra L. Da Roz, Ervino C. Ziemath, and Osvaldo N. Oliveita Jr.. "Theoretical Models for Surface Forces and Adhesion and Their Measurement Using Atomic Force Microscopy." *International Journal of Molecular Sciences* 13 (2012): 12773-12856.
51. Zhang, Li Li, and X S. Zhao. "Carbon-based Materials as Supercapacitor Electrodes." *Chemical Society Reviews*. 38 (2009): 2520-2531.
52. Kirby, Brian. *Micro- and Nanoscale Fluid Mechanics: Transport in Microfluidic Devices*. NY: Cambridge University Press, 2010.

53. Madou, Marc. *Fundamentals of Microfabrication and Nanotechnology, Third Edition, Volume One: Solid-State Physics, Fluidics and Analytical Techniques in Micro- and Nanotechnology*. CRC Press, 2012.
54. Salieb-Beugelaar, G., Dorfman, K., Van Den Berg, A., Grismer, L. & Eijkel, J. (2009). Electrophoretic separation of DNA in gels and nanostructures. *Lab on a Chip*, 9, 2508-2523.
55. Zahn, Jeffrey D. *Biomicrofabrication and Biomicrofluidics*. Boston: Artech House, 2010.
56. Lee, Ki B. *Principles of Microelectromechanical Systems*. Boston: Wiley-IEEE, 2011.
57. "Plasma Enhanced Chemical Vapor Deposition." SNTEK LTD, n.d. Web. 15 Apr. 2014. <<https://www.crystec.com/tridepe.htm>>.
58. Ranganathan, Srikanth, Richard McCreery, Sree M. Majji, and Marc Madou. "Photoresist-Derived Carbon for Microelectromechanical Systems and Electrochemical Applications." *Journal of the Electrochemical Society* 147.1 (2000): 277-282.
59. Karunakaran, B, J P. Jeong, S J. Chung, and E K. Suh. "Low-Temperature Deposition of Silicon-Nitride Layers by Using PECVD for High Efficiency Si Solar Cells." *Journal of the Korean Physical Society* 48.6 (2005): 1250-1254.
60. "What Is PECVD?" Plasma Equipment Technical Services Incorporated, 15 Apr. 2014. Web. <<http://www.plasmaequip.com/WHAT IS PECVD.pdf>>.
61. Fedosenko, G, A Schwabedissen, J Engemann, E Braca, L Valentini, and J M. Kenny. "Pulsed PECVD Deposition of Diamond-like Carbon Films." *Diamond and Related Materials. 12th European Conference on Diamond, Diamond-like Materials, Carbon Nanotubes, Nitrides and Silicon Carbide* 11.3-6 (2002): 1047-1052.
62. Xu, Xiangdong, Qiong He, Taijun Fan, Yadong Jiang, Long Huang, Tianhong Ao, and Cunqian Ma. "Hard and Relaxed A-SiN_xHy Films Prepared by PECVD: Structure Analysis and Formation Mechanism." *Applied Surface Science* 264 (2013): 823-831.
63. Da Silva Zambom, Luis, Ronaldo D. Mansano, and Ana P. Mousinho. "Low-temperature Deposition of Silicon Oxide and Silicon Nitride by Reactive Magnetron Sputtering." *Microelectronics Journal* 40.1 (2009): 66-69.
64. Adrianus De Groot, Wilhelmus, James R. Webster, Daniel Felnhofer, and Evgeni P. Gusev. "Review of Device Reliability Physics of Dielectrics in Electrostatically Driven

- MEMS Devices." *IEEE Transactions on Device and Materials Reliability* 9.2 (2009): 190-202.
65. Ansari, Kambiz, Jeroen Anton Van Kan, Andrew A. Bettioli, and Frank Watt. "Stamps for Nanoimprint Lithography Fabricated by Proton Beam Writing and Nickel Electroplating." *Journal of Micromechanics and Microengineering* 16 (2006): 1967-1974.
 66. Schumuki, Patrik, and Sannakaisa Virtanen. *Electrochemistry at the Nanoscale*. NY: Springer, 2009.
 67. Zabetakis, Daniel, and Walter J. Dressick. "Selective Electroless Metallization of Patterned Polymeric Films for Lithography Applications." *ACS Applied Materials and Interfaces* 1.1 (2009): 4-25.
 68. Schlesinger, Mordechai, and Milan Paunovic. *Modern Electroplating*, Fifth Edition. Hoboken, NJ: John Wiley & Sons, 2010.
 69. Adams, Thomas M., and Richard Layton. *Introductory MEMS Fabrication and Applications*. NY: Springer, 2010.
 70. Gad-el-Hak, M. *MEMS Design and Fabrication*. Boca Raton, FL: CRC Taylor & Francis Group, 2006.
 71. Guangchi Xuan; Adam, T.N.; Suehle, J.; Fitzgerald, E.; Pengcheng Lv; Sustersic, N.; Copping, M.J.; Kolodzey, J., "Xenon Difluoride Dry Etching of Si, SiGe Alloy and Ge," *SiGe Technology and Device Meeting, 2006. ISTDM 2006. Third International* , vol., no., pp.1,2, 15-17 May 2006
 72. Owen, K J., B VanDerElzen, R L. Peterson, and K Najafi. "High Aspect Ratio Deep Silicon Etching." *IEEE MEMS 2012* (2012): 251-254.
 73. Tang, Y, R L. Peterson, and K Najafi. "Technology for Fabricating Dense 3-D Microstructure Arrays for Biomimetic Hair-Like Sensors." *IEEE MEMS 2013* (2013): 355-358.
 74. Martin, Peter. "Chapter 9 - Plasma-Enhanced Chemical Vapor Deposition of Functional Coatings." *Handbook of Deposition Technologies for Films and Coatings (Third Edition)*. United States: Elsevier, 2010. 392-465.

75. Levinson, Harry J. *Principles of Lithography, Third Edition*. Bellingham, WA: SPIE, Press, 2010.
76. "Lithography Overviews." MicroChem Corporation, n.d. Web. 4 Apr. 2014.
<<http://www.microchem.com/Prod-LithographyOverviewPosNeg.htm>>.
77. Zachek, Matthew, Jinwoo Park, Pavel Takmakov, R M. Wightman, and Gregory S. McCarty. "Microfabricated FSCV-compatible Microelectrode Array for Real-time Monitoring of Heterogeneous Dopamine Release." *The Royal Society of Chemistry, Analyst* 135 (2010): 1556-1563.
78. Dengler, Adam K., and Gregory S. McCarty. "Microfabricated Microelectrode Sensor for Measuring Background and Slowly Changing Dopamine Concentrations." *Journal of Electroanalytical Chemistry* 693 (2013): 28-33.
79. Wang, Wanjun, and Steven Soper. *Bio-MEMS: Technologies and Applications*. CRC Press, 2007.
80. Bernhard, Wolfrum, Marcel Zevenbergen, and Serge Lemay. "Nanofluidic Redox Cycling Amplification for the Selective Detection of Catechol." *Analytical Chemistry* 80, 972-977.
81. Wang, Huai Y., Yue Sun, and Bo Tang. "Study on Fluorescence Property of Dopamine and Determination of Dopamine by Fluorimetry." *Talanta* 57 (2002): 899-907.
82. Palanisamy, S, Shuhao Ku, and Shen-Ming Chen. "Dopamine Sensor Based on Glassy Carbon Electrode Modified with Reduced Graphene Oxide and Palladium Nanoparticles Composite." *Microchim Acta* 180 (2013): 1037-1042.
83. Kim, Yang-Rae, Sungyool Bong, Yeon-Joo Kang, Yongtak Yang, Rakesh Mahajan, Jong S. Kim, and Hasuck Kim. "Electrochemical Detection of Dopamine in the Presence of Ascorbic Acid Using Graphene Modified Electrodes." *Biosensors and Bioelectronics* 25 (2010): 2366-2369.
84. Shankar, S, B E. Swamy, M Panduranganchar, Umesh Chandra, B Chandrashekar, J G. Manjunatha, and B S. Sherigara. "Electrocatalytic Oxidation of Dopamine on Acrylamide Modified Carbon Paste Electrode: a Voltammetric Study." *International Journal of Electrochemical Science* 5 (2010): 944-954.

85. Barnes, Edward, Aoife O'Mahony, Leigh Aldous, Christopher Hardacre, and Richard Compton. "The Electrochemical Oxidation of Catechol and Dopamine on Platinum in 1-Ethyl-3-methylimidazolium Bis(trifluoromethylsulfonyl)imide ([C₂mim][Ntf₂] and 1-Butyl-3-methylimidazolium Tetrafluoroborate ([C₄mim][BF₄]) Adsorption Effects in Ionic Liquid Voltammetry." *Journal of Electroanalytical Chemistry* 646 (2010): 11-17.
86. "Dopamine Hydrochloride Injection, Solution [General Injectables & Vaccines, Inc]." U.S. National Library Of Medicine, National Institutes Of Health, Health And Human Services, n.d. Web.<<http://dailymed.nlm.nih.gov/dailymed/lookup.cfm?setid=d76ebb82-bc6b-47fc-9a32-58357a43e783>>.
87. Yao, Hong, Yuanyuan Sun, Xinhua Lin, and Liying Huang. "Electrochemical Characterization of Poly(eriochrome Black T) Modified Glassy Carbon Electrode and Its Application to Simultaneous Determination of Dopamine, Ascorbic Acid and Uric Acid." *Electrochimica Acta* 52 (2007): 6165-6171.
88. Tóth, Béla, Miklós Vecsernyés, Tivadar Zelles, Kristóf Kádár, and György Nagy. "Role of Peripheral and Brain-Derived Dopamine (DA) in Immune Regulation." *Advances in Neuroimmune Biology* 52(2012): 111-155.
89. Buttarelli, Francesca, Alessandra Faniulli, Clelia Pellicano, and Francesco Pontieri. "The Dopaminergic System in Peripheral Blood Lymphocytes: from Physiology to Pharmacology and Potential Applications to Neuropsychiatric Disorders." *Current Neuropharmacology* 9(2011): 278-288.
90. Pacheco, Rodrigo, Carolina E. Prado, Magaly J. Barrientos, and Sebastian Bernales. "Role of Dopamine in the Physiology of T-cell and Dendritic Cells." *Journal of Neuroimmunology* 216(2009): 8-19.
91. Guyton, Arthur C., and John E. Hall. *Textbook of Medical Physiology*. Philadelphia: Elsevier, 2006.
92. Venton, B, Hui Zhang, Paul Garris, Paul Phillips, David Sulzer, and R M. Wightman. "Real-time Decoding of Dopamine Concentration Changes in the Caudate-putamenduring Tonic and Phasic Firing." *Journal of Neurochemistry* 87(2003): 1284-1295.
93. Pacheco, Rodrigo, Francisco Contreras, and Moncef Zouali. "The Dopaminergic System in Autoimmune Diseases." *Frontiers in Immunology* 5(2014): 1-17.

94. Herculano-Houzel, Suzana. "The Human Brain in Numbers: a Linearly Scaled-up Primate Brain." *Frontiers in Human Neuroscience* 3.31 (2009): 1-11.
95. Azevedo, F A., L R. Car, L T. Grinberg, J M. Farfel, R E. Ferretti, R E. Leite, Filho W. Jacob, R Lent, and S Herculano-Houzel. "Equal Numbers of Neuronal and Nonneuronal Cells Make the Human Brain an Isometrically Scaled-up Primate Brain." *Journal of Computational Neurology* 513.5 (2009): 532-541.
96. Gross, Liza. "From Structure to Function: Mapping the Connection Matrix of the Human Brain." *PLoS: Biology* 6.7 (2008): 1357. Web. <<http://www.plosbiology.org/article/info%3Adoi%2F10.1371%2Fjournal.pbio.0060164>>.
97. Chu-Shore, Catherine, Matt Kramer, Matt Bianchi, Verne Caviness, and Sydney Cash. "Network Analysis: Applications for the Developing Brain." *Journal of Child Neurology* 26.4 (2011): 488-500.
98. Kim, Do Hyoung, Yoonbae Oh, Hojin Shin, Charles D. Blaha, Kevin E. Bennet, Kendall H. Lee, In Young Kim, and Dong Pyo Jang. "Investigation of the Reduction Process of Dopamine Using Paired Pulse Voltammetry." *Journal of Electroanalytical Chemistry* 717-718 (2014): 157-164.
99. Jang, Dong Pyo, Inyong Kim, Su-Youme Chang, Hoon-Ki Min, Kanika Arora, Michale P. Marsh, Sun-Chul Hwang, Christopher J. Kimble, Kevin E. Bennet, and Kendall H. Lee. "Paired Pulse Voltammetry for Differentiating Complex Analytes." *Analyst (The Royal Society of Chemistry)* 137(2012): 1428-1435.
100. Bradley, Bath D., Darren J. Michael, B J. Trafton, Joshua D. Josphe, Petrise L. Runnels, and R. Mark Wightman. "Subsecond Adsorption and Desorption of Dopamine at Carbon-Fiber Microelectrodes." *Analytical Chemistry* 72.24 (2000): 5994-6002.
101. Colin-Orozco, E, S Corona-Avendano, M T. Ramirez-Silva, M Romero-Romo, and M Palomar-Pardave. "On the Electrochemical Oxidation of Dopamine, Ascorbic Acid, and Uric Acid onto a Bare Carbon Paste Electrode from a 0.1M NaCl Aqueous Solution at PH 7." *International Journal of Electrochemical Science* 7(2012): 6097-6105.
102. Enno, Katelkohn, and Bernhard Wolfrum. "On-chip Redox Cycling Techniques for Electrochemical Detection." *Reviews in Analytical Chemistry* 31.1 (2012): 7-14.
103. Aoki, Koichi. "Theory of Ultramicroelectrodes." *Electroanalysis* 5(1993): 627-639.

104. Shoup, David, and Attila Szabo. "Chronoamperometric Current at Finite Disk Electrodes." *Journal of Electroanalytical Chemistry* 140(1982): 237-245.
105. Bell, Christopher. "The Long-Time Chronoamperometric Current at an Inlaid Microband (or Laminar) Electrode." *Sensors* 13(2013): 626-647.
106. Prasad, Bhim, Shrinkhala Srivastava, Khushaboo Tiwari, and Sindhu Sharma. "Trace-level Sensing of Dopamine in Real Samples Using Molecularly Imprinted Polymer-sensor." *Biochemical Engineering Journal* 44.2-3 (2009): 232-239.
107. Fausto, Rui, Maria João S. Ribeiro, and João J. Pedroso De Lima. "A Molecular Orbital Study on the Conformational Properties of Dopamine [1,2-benzenedio-4(2-aminoethyl)]and Dopamine Cation." *Journal of Molecular Structure* 484(1999): 181-196.
108. Ohshima, Hiroyuki, and Kunio Furusawa. *Electrical Phenomena at Interfaces, Second Edition: Fundamentals: Measurements, and Application (Surfactant Science)*. M.Dekker, New York, 1998.
109. Srinivasan, S, and Kunio Furusawa. *Fuel Cells, from Fundamentals to Applications*. Springer, 2006.
110. Bockris, J. O'M., M.A.V. Devanathan, and K Muller. "On the Structure of Charged Interfaces." *Proceedings of the Royal Society A* 274(1963): 55-79.
111. Albrecht, T. "Electrochemical Tunnelling Sensors and Their Potential Applications." *Nature Communications* 3.829 (2012): 1-10.
112. Arima, Akhide, Makusa Tsutsui, Takanori Morikawa, Kazumichi Yokota, and Masateru Taniguchi. "Fabrications of Insulator-protected Nanometer-sized Electrode Gaps." *Journal of Applied Physics* 115(2014): pg 114310-1 to 114310-5.
113. Compton, Richard. *Understanding Voltammetry (2nd Edition)*. Ch 7, Imperial College Press, London, 2010.
114. Uman, Martin. *The Lightning Discharge*. Toronto, Canada: General Publishing Company, pg 64, 2001.
115. Edwards, Peter, Harry B. Gray, Matthew Lodge, and Robert Williams. "Electron Transfer and Electronic Conduction Through an Intervening Medium." *Angewandte Chemie International Edition* 47(2008): 6758-6765.

116. Dickinson, Edmund, and Richard G. Compton. "Influence of the Diffuse Double Layer on Steady-state Voltammetry." *Journal of Electroanalytical Chemistry* 661(2011): 198-212.
117. Compton, Richard, Christopher Batchelor-McAuley, and Edmund Dickinson. *Understanding Voltammetry: Problems and Solutions*. London: Imperial College Press, 2012.
118. Winkler, Jay R., and Harry B. Gray. "Long-Range Electron Tunneling." *Journal of the American Chemical Society* 136 (2014): 2930-2939.
119. Lagutschenkov, Anita, Judith Langer, Giel Berden, Jos Oomes, and Otto Dopfer. "Infrared Spectra of Protonated Neurotransmitters: Dopamine." *Physical Chemistry Chemical Physics* 13(2011): 2815-2823.
120. Gray, Harry B., and Jay R. Winkler. "Electron Tunneling Through Proteins." *Quarterly Review of Biophysics* 36 (2003): 341-372.
121. Nagy, Peter, Giuliano Alagona, and Caterina Ghio. "Theoretical Studies on the Conformation of Protonated Dopamine in the Gas Phase and in the Aqueous Phase." *Journal of the American Chemical Society* 121.20 (1999): 4804-4815.
122. Beratan, David N., Spiros S. Skourtis, Ilya A. Balabin, Alexander Balaeff, Shahar Keinan, Ravindra Venkatramani, and Dequan Xiao. "Steering Electrons on Moving Pathways." *Accounts of Chemical Research* 42.10 (2009): 1669-1678.
123. de la Lande, Aurelian, Sergio Marti, Oliver Parisel, and Vicent Moliner. "Long Distance Electron-transfer Mechanism in Peptidylglycine Alpha-hydroxylating Monooxygenase: a Perfect Fitting for a Water Bridge." *Journal of American Chemical Society* 129(2007): 11700-11707.
124. de la Lande, Aurelian, Nathan S. Babcock, Jan Rezac, Barry C. Sander, Dennis R. Salahub, and David N. Beratan. "Surface Residues Dynamically Organize Water Bridge to Enhance Electron Transfers Between Proteins." *Proceedings of the National Academy of Science of the United States of America* 107.26 (2010): 11799-11804.
125. Lin, Jianping, Ilya A. Balabin, and David Beratan. "The Nature of Aqueous Tunneling Pathways Between Electron-Transfer Proteins." *Science* 310.5752 (2005): 1311-1313.

126. Bandosz, Teresa. *Activated Carbon Surfaces in Environmental Remediation*. USA, Elsevier, 2006, pg 296.
127. Gorman, James. "All Circuits Are Busy." *New York Times*, 26 May 2014. Web. 26 May 2014. <http://www.nytimes.com/2014/05/27/science/all-circuits-are-busy.html?_r=0>.
128. Heinzl, S, TG Riemer, S Schulte, J Onken, A Heinz, and MA Rapp. "Catechol-O-methyltransferase (COMT) Genotype Affects Age-related Changes in Plasticity in Working Memory: a Pilot Study." *BioMed Research International* (2014): Article ID 414351, pg 1-7.
129. Morita, Masao, Katsuyoshi Hayashi, Tsutomu Horiuchi, Sayaka Shibano, Katsunobu Yamamoto, and Koichi J. Aoki. "Enhancement of Redox Cycling Currents at Interdigitated Electrodes with Elevated Fingers." *Journal of the Electrochemical Society* 161.4 (2014): H178-H182.
130. Kamath, Rahul R., and Marc J. Madou. "Three-Dimensional Carbon Interdigitated Electrode Arrays for Redox-Amplification." *Analytical Chemistry* 86(2014): 2963-2971.
131. Kimble, Christopher J., David M. Johnson, Bruce A. Winter, Sidney V. Whitlock, Kenneth R. Kressin, April E. Horne, Justin C. Robinson, Jonathan M. Bledsoe, Susannah J. Tye, Su-Youne Chang, Filippo Agnesi, Christoph J. Griessenauer, David Covey, Young-Min Shon, Kevin E. Bennet, Paul A. Garris, and Kendall H. Lee. "Wireless Instantaneous Neurotransmitter Concentration Sensing System (WINCS) for Intraoperative Neurochemical Monitoring." *31st Annual International Conference of the IEEE EMBS, Minneapolis, Minnesota, USA, September 2-6, (2009)*: 4856-4859.